

**AFRL-IF-RS-TR-2005-390**  
**Final Technical Report**  
**November 2005**



# **BIOFLUIDIC INTELLIGENT PROCESSORS FOR PREPARATIVE MANIPULATIONS OF BIOLOGICAL WARFARE AGENTS AT THE ATTOMOLE LEVEL**

**University of Illinois at Urbana-Champaign**

**Sponsored by**  
**Defense Advanced Research Projects Agency**  
**DARPA Order No. J302**

*APPROVED FOR PUBLIC RELEASE; DISTRIBUTION UNLIMITED.*

The views and conclusions contained in this document are those of the authors and should not be interpreted as necessarily representing the official policies, either expressed or implied, of the Defense Advanced Research Projects Agency or the U.S. Government.

**AIR FORCE RESEARCH LABORATORY  
INFORMATION DIRECTORATE  
ROME RESEARCH SITE  
ROME, NEW YORK**

# STINFO FINAL REPORT

This report has been reviewed by the Air Force Research Laboratory, Information Directorate, Public Affairs Office (IFOIPA) and is releasable to the National Technical Information Service (NTIS). At NTIS it will be releasable to the general public, including foreign nations.

AFRL-IF-RS-TR-2005-390 has been reviewed and is approved for publication

APPROVED: /s/  
GEORGE O. RAMSEYER  
Project Engineer

FOR THE DIRECTOR: /s/  
JAMES A. COLLINS, Deputy Chief  
Advanced Computing Division  
Information Directorate

# REPORT DOCUMENTATION PAGE

Form Approved  
OMB No. 074-0188

Public reporting burden for this collection of information is estimated to average 1 hour per response, including the time for reviewing instructions, searching existing data sources, gathering and maintaining the data needed, and completing and reviewing this collection of information. Send comments regarding this burden estimate or any other aspect of this collection of information, including suggestions for reducing this burden to Washington Headquarters Services, Directorate for Information Operations and Reports, 1215 Jefferson Davis Highway, Suite 1204, Arlington, VA 22202-4302, and to the Office of Management and Budget, Paperwork Reduction Project (0704-0188), Washington, DC 20503

<b>1. AGENCY USE ONLY (Leave blank)</b>			<b>2. REPORT DATE</b> November 2005	<b>3. REPORT TYPE AND DATES COVERED</b> Final Jun 00 – Sep 04
<b>4. TITLE AND SUBTITLE</b> BIOFLUIDIC INTELLIGENT PROCESSORS FOR PREPARATIVE MANIPULATIONS OF BIOLOGICAL WARFARE AGENTS AT THE ATTOMOLE LEVEL			<b>5. FUNDING NUMBERS</b> G - F30602-00-2-0567 PE - 63739E PR - E117 TA - 00 WU - 54	
<b>6. AUTHOR(S)</b> Paul W. Bohn Johnathan V. Sweedler Mark A. Shannon			<b>8. PERFORMING ORGANIZATION REPORT NUMBER</b> N/A	
<b>7. PERFORMING ORGANIZATION NAME(S) AND ADDRESS(ES)</b> University of Illinois at Urbana-Champaign 3351 Beckman Institute 405 North Matthews Avenue Urbana IL 61801			<b>9. SPONSORING / MONITORING AGENCY NAME(S) AND ADDRESS(ES)</b> Defense Advanced Research Projects Agency AFRL/IFTC 3701 North Fairfax Drive 525 Brooks Road Arlington VA 22203-1714 Rome NY 13441-4505	
<b>11. SUPPLEMENTARY NOTES</b> AFRL Project Engineer: George Ramseyer/IFTC/(315) 330-3492			<b>10. SPONSORING / MONITORING AGENCY REPORT NUMBER</b> AFRL-IF-RS-TR-2005-390 George.Ramseyer@rl.af.mil	
<b>12a. DISTRIBUTION / AVAILABILITY STATEMENT</b>  APPROVED FOR PUBLIC RELEASE; DISTRIBUTION UNLIMITED.			<b>12b. DISTRIBUTION CODE</b>	
<b>13. ABSTRACT (Maximum 200 Words)</b> A new type of biofluidic transport system, the Biofluidic Intelligent Processor (BIP), was developed which specifically used biological compounds to adaptively control the transport of microfluids. The multicompartiment, multimembrane BIP system was designed, fabricated and tested. The BIP had characteristic linear dimensions of nanometers and volumes as small as tens of attoliters, and was specifically designed to manipulate nano-amounts of species. Electrokinetic and other standard microfluidic flows were exploited to move species among the separate compartments of the system, where molecules were selectively separated and transported from the influent to the detector, independent of the other constituents within the biofluid. Within the new biofluidic BIP system were integrated compartments, including molecular gates, which were based on novel membranes that performed important biomolecular manipulations that included affinity binding and molecular sieving. The molecular gate concept is analogous to transistors, in that switching, gain, and digital manipulation of specific molecules, such as proteins, are now possible.				
<b>14. SUBJECT TERMS</b> Microfluidics, microfluidics system, manofluidic system, Biofluidic Intelligent Processor, attoliter, molecular gate, affinity binding, molecular sieving, transport of microfluids, electrokinetic microfluidic flow			<b>15. NUMBER OF PAGES</b> 172	
			<b>16. PRICE CODE</b>	
<b>17. SECURITY CLASSIFICATION OF REPORT</b>  UNCLASSIFIED	<b>18. SECURITY CLASSIFICATION OF THIS PAGE</b>  UNCLASSIFIED	<b>19. SECURITY CLASSIFICATION OF ABSTRACT</b>  UNCLASSIFIED	<b>20. LIMITATION OF ABSTRACT</b>  UL	

## TABLE OF CONTENTS

<b>LIST OF FIGURES .....</b>	<b>v</b>
<b>LIST OF TABLES .....</b>	<b>viii</b>
<b>1. EXECUTIVE SUMMARY .....</b>	<b>1</b>
<b>2. INTRODUCTION.....</b>	<b>2</b>
<b>2.1 The Approach .....</b>	<b>2</b>
<b>2.2 The Results.....</b>	<b>2</b>
<b>3. TRANSPORT .....</b>	<b>5</b>
<b>3.1 Synthesis of the Affinity Tag .....</b>	<b>5</b>
<b>3.2 Botulinum Neurotoxins Type A(BoNT/A) Affinity Tag .....</b>	<b>6</b>
<b>3.3 Size-dependent Gate Performance.....</b>	<b>7</b>
<b>3.4 Affinity Tag Desorption. .....</b>	<b>10</b>
<b>3.5 Electrochemistry in the Microdevices.....</b>	<b>12</b>
<b>3.6 Improvements in the Affinity Tag Synthesis.....</b>	<b>13</b>
<b>3.7 Size-dependent Gate Performance.....</b>	<b>14</b>
<b>3.8 Memory Effects.....</b>	<b>15</b>
<b>3.9 Au-coated Nanoaffinity Gates .....</b>	<b>16</b>
<b>3.10 Nanoaffinity Complex .....</b>	<b>16</b>
<b>3.11 Au-coated Nanoaffinity Gates .....</b>	<b>17</b>
<b>3.12 Transport Rate and Efficiency .....</b>	<b>18</b>
<b>3.13 Molecular Transport Gating Functions .....</b>	<b>19</b>
<b>3.14 Nanoaffinity Channels .....</b>	<b>22</b>
<b>3.15 Affinity Tag .....</b>	<b>23</b>
<b>3.16 Pore-size Measurement Devices .....</b>	<b>24</b>

3.17	Size Selective Sampling .....	27
3.18	Affinity Gate .....	27
3.19	Reaction Profiling.....	29
3.20	Reactive Mixing .....	31
3.21	Membrane Chemistry .....	37
3.22	Fluorescence/Electrochemical Desorption of SAMSA. ....	38
3.23	Fluorescence/Electrochemical Desorption of BoNT/A Affinity Tag .....	39
3.24	Maintaining Salt Concentration Differentials.....	40
3.25	SAMSA Adsorption and Desorption Experiments .....	42
3.26	Affinity Tag Experiments .....	44
3.27	Post Processing of Collected Samples .....	46
3.28	Development of a catalytic DNA-based $Pb^{2+}$ sensor .....	50
3.29	Proton Gradient Homostasis .....	52
3.30	Dynamic Mixing Studies with Fast Scanning Confocal Microscopy.....	53
4.	FABRICATION .....	56
4.1	Designed and fabricated masks for test bed prototypes.....	56
4.2	Developed a method for patterning fluid channels.....	58
4.3	Determine compatible membrane for nanochannel .....	58
4.4	Develop membrane transfer process to substrate.....	58
4.5	Etching of silicon .....	58
4.6	Start-up Challenges.....	59
4.7	Second stage of fabrication of a first plus generation of BIP.....	61
4.8	Phenolic adhesive bonding.....	61
4.9	Development of high-aspect ratio frit structures.....	63
4.10	BIP Multilevel Fabrication .....	64
4.11	A new method of transferring and bonding multiple layers.....	66
4.12	BIP Fabrication .....	69

<b>4.13 Five Layer Second Generation BIP .....</b>	<b>72</b>
<b>4.14 A New Second Generation BIP .....</b>	<b>75</b>
<b>4.15 Atomization Spray.....</b>	<b>77</b>
<b>4.16 Fabrication of the next generation BIP .....</b>	<b>78</b>
<b>4.17 Active Nanogate Fabrication.....</b>	<b>78</b>
<b>4.18 Improving the fabrication of the BIP .....</b>	<b>79</b>
<b>4.19 Transfer Printing Process.....</b>	<b>80</b>
<b>4.20 Transfer of Polyimide Middle Channel Layer.....</b>	<b>82</b>
<b>4.21 Gold Deposition for Affinity Gates .....</b>	<b>84</b>
<b>4.22 Increased Clarity of the BIP Stack. .....</b>	<b>85</b>
<b>4.23 Eight Layer Stacked BIP .....</b>	<b>90</b>
<b>4.24 BIP Chip Fabrication.....</b>	<b>93</b>
<b>4.25 Nano-Affinity Gate Fabrication .....</b>	<b>95</b>
<b>4.26 Affinity Gate Fabrication/Operation.....</b>	<b>96</b>
<b>4.27 BIP Fabrication .....</b>	<b>100</b>
<b>5.0 INTERFACING AND OPERATION .....</b>	<b>103</b>
<b>5.1 Prototype Testing .....</b>	<b>103</b>
<b>5.2 Different Gate Membranes.....</b>	<b>106</b>
<b>5.3 Transport .....</b>	<b>109</b>
<b>5.4 Transport Behavior by Fluorescence Imaging.....</b>	<b>113</b>
<b>5.5 Stacking Effect of the Membrane .....</b>	<b>114</b>
<b>5.6 Interfacing and Characterization of the First Generation BIP .....</b>	<b>115</b>
<b>5.7 Optimization of the Operation in the Second Generation Prototype BIP's .....</b>	<b>117</b>
<b>5.8 Automated Sample Injections. .....</b>	<b>119</b>
<b>5.9 Molecular Gates as Injectors.....</b>	<b>121</b>
<b>5.10 Composite Device Structures.....</b>	<b>123</b>
<b>5.11 Molecular Gates as Injectors.....</b>	<b>124</b>

<b>5.12 Band Collection.....</b>	<b>129</b>
<b>5.13 Automated Collection of Chromatographic Bands .....</b>	<b>132</b>
<b>5.14 Fluorescence Characterization of Second Generation BIP.....</b>	<b>135</b>
<b>5.15 Membrane Gated Injections for Chip-based Separations .....</b>	<b>137</b>
<b>5.16 Impedance Analysis of the Membrane Gated Injections .....</b>	<b>139</b>
<b>5.17 Fluorescence Characterization of Second Generation BIP's.....</b>	<b>141</b>
<b>5.18 Membrane Gated Injections for Microfluidic Chip-based Separations .....</b>	<b>141</b>
<b>5.19 Impedance Analysis of the Membrane Gated Injections .....</b>	<b>143</b>
<b>5.20 Microfluidic Salt Gradients Across Nanofluidic Membrane Gates .....</b>	<b>144</b>
<b>5.21 Automated Manipulation of Attomole Samples.....</b>	<b>148</b>
<b>5.22 Post-Processing of Collected Samples.....</b>	<b>151</b>
<b>5.23 Dynamic Mixing Studies with Ultrafast Confocal Microscopy .....</b>	<b>152</b>
<b>6. CONCLUSIONS .....</b>	<b>155</b>
<b>7. SUMMARY AND FUTURE PROSPECTS.....</b>	<b>158</b>
<b>8. REFERENCES.....</b>	<b>159</b>
<b>APPENDIX I. LIST OF JOURNAL PUBLICATIONS.....</b>	<b>160</b>

## LIST OF FIGURES

Figure 1. BoNT/A affinity tag with protected thiol group.	7
Figure 2. 2 MDa FITC-labeled Dextran transport.	8
Figure 3. Transport across a 100-nm pore diameter membrane.	9
Figure 4. Mass-diameter dependent gating.	9
Figure 5. Schematic of <i>in situ</i> fluorescence and electrochemical measurements.	10
Figure 6. Fluorescence intensity as a function of time.	11
Figure 7. Electrochemistry from the microfabricated devices.	12
Figure 8. Labeled heptapeptide.	13
Figure 9. Uptake of probe as a function of gating potential for fluorescently-labeled dextrans.	14
Figure 10. Reductive scans (Current (a.u.) v. Potential) of adsorbed 1-hexadecanethiol.	17
Figure 11. Relative transport rate of fluorescein vs. absolute bias (Transport Efficiency (%)) vs. Voltage) in a 200-nm device.	18
Figure 12. Transport efficiency (%) of fluorescein vs. absolute bias in the PDMS devices.	19
Figure 13. Molecular transport of 2 MDa FITC-labeled dextran across a 200-nm pore size membrane in a 3-D PDMS/PCTE/PDMS structure.	20
Figure 14. Reproducibility of analyte injection into the receiving channel tested with 2 MDa FITC labeled dextran under varying transport conditions.	20
Figure 15. Scanning electron micrographs of electroless Au plated 50-nm pore diameter membranes.	22
Figure 16. Scanning electron micrographs of electroless Au plated 50-nm pore diameter membranes.	24
Figure 17. Downstream pressure as a function of time for a 10-nm pore diameter membrane.	25
Figure 18. Size selective transport with two-color detection.	26
Figure 19. A. Electrode patterning on PDMS directly. B. New design patterning on glass substrate.	28
Figure 20. Electron micrographs of 50-nm pore diameter membranes before (A) and after (B&C) 2 hr electroless Au plating at room temperature.	28
Figure 21. Cross-sectional SCM fluorescence images of fluorescein mixing.	30
Figure 22. Fluorescence profiles of reaction 1 along the receiving channel.	33
Figure 23. Fluorescence profiles of reaction 1 along the receiving channel under different applied voltages.	34
Figure 24. Ca <sup>2+</sup> Detection.	36
Figure 25. Cyclic voltammogram of a Au-coated nanopore molecular gate membrane decorated with the S-terminated fluorophore SAMSA.	37
Figure 26. Time dependence of the release of the fluorescent model SAMSA.	38
Figure 27. Concurrent fluorescence and microchannel current measurements to assess biased mobility transport.	41
Figure 28. The exact structure of SAMSA.	42
Figure 29. Time dependence of the release of the fluorescent model SAMSA.	43
Figure 30. Time dependent release of SAMSA from a planar gold surface measured by SPR.	44
Figure 31. SPR spectroscopy of the botulism affinity tag (SH-Lys-Fl-Cys-Arg-Ala-Thr-Lys-Met-Leu) in gold nanotubes.	45
Figure 32. Plot of the number density of surface adsorbed CKWAKWAK.	46
Figure 33. UV-Visible absorption spectra of 2 nM CKWAKWAK/colloid conjugates under different conditions.	47
Figure 34. Transmission electron micrographs and nearest neighbor distance histograms.	48
Figure 35. Expanded molecular ion region of the MALDI mass spectrum of the CKWAKWAK/colloid conjugate.	50
Figure 36. Comparison of concentration of Pb <sup>2+</sup> induced DNA released with controls.	51
Figure 37. Confocal optical xz microsections of the nanofluidic interconnect regions under conditions of varying pH.	53
Figure 38. Schematic of a multilayer device.	54
Figure 39. Fluorescence intensity as a function of adjusted time at 5-μm and 35-μm below the gate.	55
Figure 40. Schematic of the initial test bed electrophoretic channels in the substrate.	56

<b>Figure 41. Photograph of the masks designed to create the test bed.</b>	57
<b>Figure 42. Photographs of channels (left) and through-holes (right) etched into Si wafers.</b>	59
<b>Figure 43. SEM micrograph of glass etching which showed excessive pitting.</b>	60
<b>Figure 44. A nanogate membrane bonded to glass with phenolic.</b>	61
<b>Figure 45. Development of micro-”grass” structures for making low-pressure loss glass frits for ultra-high area filtering of influent.</b>	62
<b>Figure 46. Cluster tool evaporator and sputterer (left).</b>	63
<b>Figure 47. Evaporator system developed for fabricating the membranes.</b>	64
<b>Figure 48. Mask sets to etch 6 of the 7 layers in the BIP.</b>	65
<b>Figure 49. PDMS bonded membrane on etched glass slide.</b>	69
<b>Figure 50. PDMS channels integrated with a membrane.</b>	70
<b>Figure 51. Concept of phenolic conforming to a “rough” membrane topography and planarizing for m multiple stacked layers.</b>	70
<b>Figure 52. A hydrophobic PC membrane bonded to glass with an aqueous-based thermosetting phenolic adhesive.</b>	71
<b>Figure 53. An enlarged side view of a five-layer second generation BIP.</b>	72
<b>Figure 54. Second generation BIP made with etched glass sandwich of two polycarbonate membranes that were patterned to form gate and microfluidic channels.</b>	73
<b>Figure 55. Second generation BIP made with etched glass sandwich of two polycarbonate membranes.</b>	75
<b>Figure 56. A photograph of a nanopore polycarbonate membrane on a carrier that was sprayed with the phenolic adhesive.</b>	76
<b>Figure 57. The next generation BIP.</b>	77
<b>Figure 58. (Left) Phenolic adhesive transferred to glass using a PDMS platen. (Right) Polycarbonate nanopore membrane transferred to glass.</b>	80
<b>Figure 59. Polyimide patterned on a carrier glass.</b>	82
<b>Figure 60. Full stack bonded via transfer printing and bonding.</b>	82
<b>Figure 61. Bonded PC membrane to bond the polyimide middle layer.</b>	83
<b>Figure 62. Thermal bonding of the polyimide middle layer to the nanopore polycarbonate layer.</b>	83
<b>Figure 63. Deposition of Au in nanopores for the fabrication of the affinity gates.</b>	84
<b>Figure 64. Photograph of a glass substrate with etched channels which has a thin layer of the new thermoplastic adhesive covering the top surface.</b>	86
<b>Figure 65. Photograph of a polycarbonate membrane bonded to a glass channel piece.</b>	87
<b>Figure 66. Photograph of a PMMA channel layer on a coverglass carrier.</b>	87
<b>Figure 67. Photograph of a bonded stack of layers.</b>	88
<b>Figure 68. Another photograph of the bonded stack of layers.</b>	88
<b>Figure 69. Photograph of the stack of Fig. 67 with the PMMA carrier and the polycarbonate excess removed.</b>	89
<b>Figure 70. Magnified photograph of the crossing channels (Fig. 69).</b>	90
<b>Figure 71. Photographs of the 8 Layered BIP chip.</b>	90
<b>Figure 72. Gold nanotubes that were electrolessly plated into 220 nm polycarbonate nanopore membranes.</b>	91
<b>Figure 73. TEM micrographs of gold plated nanopores.</b>	92
<b>Figure 74. Photographs of the BIP chip design showing (left) the cap assembly before bonding and (right) the assembled BIP.</b>	94
<b>Figure 75. Glass bottom layer with patterned metal leads for molecular gate interconnection.</b>	95
<b>Figure 76. Top acrylic layer with pin connectors to serve electrical connections from the outside world to the molecular gate region.</b>	96
<b>Figure 77. Schematic of the proposed arrangement of Pt electrodes to be fabricated within the microfluidic channels.</b>	97
<b>Figure 78. Electrical connection to the interior of the nanopores.</b>	99
<b>Figure 79. Device design having three microfluidic channels.</b>	99
<b>Figure 80. Probe station.</b>	100
<b>Figure 81. Straight-channel device.</b>	101
<b>Figure 82. Illustration of the first prototype crossed channel device.</b>	104
<b>Figure 83. Plot of the fluorescence response.</b>	105

<b>Figure 84. Fluorescein concentration in the receiving channel.</b>	107
<b>Figure 85. Fluorescein concentration in the receiving channel in response to applied voltage.</b>	108
<b>Figure 86. Fluorescence intensity and applied bias.</b>	110
<b>Figure 87. Transport of BODIPY in 15 and 200-nm pore size membrane PCTE microchips.</b>	112
<b>Figure 88. Fluorescence images vs. time.</b>	114
<b>Figure 89. Sample stacking in the source channel vs. absolute bias.</b>	115
<b>Figure 90. Schematic diagram of an injection/collection system.</b>	115
<b>Figure 91. Injection and collection of an analyte band.</b>	117
<b>Figure 92. Diagnostic station with dual detection capabilities.</b>	119
<b>Figure 93. Modes of operation of the dual point detection.</b>	119
<b>Figure 94. Schematic showing voltage sequence used for automated injections of fluorescein.</b>	121
<b>Figure 95. Gates as Injectors.</b>	122
<b>Figure 96. Fluorescence intensity in the receiving channel.</b>	123
<b>Figure 97. Schematic of molecular gate injection device.</b>	125
<b>Figure 98. Potential bias application for both injection and separation schemes.</b>	126
<b>Figure 99. Fluorescence image of gated injected analyte (FITC-labeled arginine) band across 200-nm PCTE membrane.</b>	127
<b>Figure 100. Reproducibility of the separation of <math>\mu\text{M}</math> FITC-labeled arginine and tryptophan in phosphate buffer.</b>	128
<b>Figure 101. Separation of <math>\mu\text{M}</math> FITC-labeled arginine and tryptophan in phosphate buffer as a function of the gate injection time.</b>	128
<b>Figure 102. Schematic of the separation channel and the two LIF detection regions.</b>	130
<b>Figure 103. All five bands of the post-collection volume.</b>	131
<b>Figure 104. Scheme for differential detection of chromatographic peaks.</b>	133
<b>Figure 105. Electropherograms showing the automated collection of labeled glutamate, arginine and degradation products.</b>	134
<b>Figure 106. Optical photograph of the new design for the five-layered second generation BIP.</b>	135
<b>Figure 107. Fluorescence image at the border of a connection via.</b>	136
<b>Figure 108. Laser-induced fluorescence intensity profiles.</b>	137
<b>Figure 109. Optical photograph of PDMS devised used to demonstrate gated-injections for microfluidic chip-based separations.</b>	138
<b>Figure 110. Current versus applied bias for single layer channels.</b>	139
<b>Figure 111. Current versus applied bias for an injection bias scheme compared to a simpler separation bias scheme.</b>	140
<b>Figure 112. Simplified representation of the equivalent electrical circuit for the injection bias scheme.</b>	141
<b>Figure 113. Separation of FITC-labeled arginine and typtophan.</b>	142
<b>Figure 114. Current vs. applied voltage in individual channels of a single device.</b>	144
<b>Figure 115. Schematic representation of a microfluidic chip designed for 2-D separation of proteins.</b>	146
<b>Figure 116. SEM micrograph of a 3-D micro-fluidic channel.</b>	147
<b>Figure 117. Schematic depicting method for patterning in 3-D masters to create PDMS microfluidic devices via soft lithography.</b>	148
<b>Figure 118. Schematic showing the relationship of detection strategies and device layout.</b>	149
<b>Figure 119. Separation and collection of FITC-labeled amino acids arginine and glycine.</b>	150
<b>Figure 120. Representation of attaching target specie on nanometer gold colloids for identification by MALDI.</b>	151
<b>Figure 121. Schematic of a multilayer device showing positions for confocal XZT series used for studying dynamic mixing (i.e. gated injections).</b>	152
<b>Figure 122. Confocal XZT series (210 ms/frame) for 1-s injections across a 200-nm diameter nanocapillary array.</b>	153
<b>Figure 123. Confocal XZT series (210 ms/frame) for 1-s injections across a 200-nm diameter nanocapillary array.</b>	154
<b>Figure 124. SEM micrograph of patterned nanopores highlighting the excellent patterning control of the FIB spot-milling process.</b>	155
<b>Figure 125. Confocal fluorescence images sectioning parallel to the xz plane.</b>	156

## LIST OF TABLES

Table I. Reactive Ion Etching Parameter Optimization to Minimize Corner Rolloff and Slope.....	101
Table II. Injection and Separation Parameters for Automated Triplicate Injections of 5 $\mu$ M Fluorescein in 5mM Phosphate Buffer (pH=7.7).....	120
Table III. Impedances and Electric Field Strengths in 3-D Microfluidic Systems.....	124

## 1. EXECUTIVE SUMMARY

This project targeted the construction of a multicompartiment, multimembrane biofluidic device, the Biofluidic Intelligent Processor (BIP), with characteristic linear dimensions of nanometers and volumes as small as tens of attoliters, specifically designed to manipulate species which must be handled at extremely low masses, *e.g.*, the potent neurotoxins encountered in biological warfare agents. Electrokinetic and other standard microfluidic flows were exploited to move species among the separate compartments of the device. By integrating the compartments with a new biofluidic device, the *molecular gate*, based on novel membranes developed at the University of Illinois at Urbana-Champaign (UIUC) that perform important biomolecular manipulations including affinity binding and molecular sieving, molecules were selectively separated and transported from the influents to the detectors independently from the other constituents within the biofluid.

A new type of biofluidic device was developed, which specifically used biological compounds to adaptively control the transport of fluids. The molecular gate concept is analogous to transistors, in that switching, gain, and digital manipulation of specific molecules, such as proteins, are possible. As a vehicle to demonstrate the importance of this concept to the mission of the Department of Defense (DoD), it was anticipated that structures which specifically separate and detect the potent neurotoxin serotype A from *Clostridium botulinum* (BoNT/A) would be developed and demonstrated. However, dramatic changes in the regulatory environment post-9/11, especially as it pertained to Class A agents, dictated that the work proceed with simulants.

These major accomplishments have also been disseminated by various publications, and those publications are listed in Appendix I.

## 2. INTRODUCTION

### 2.1 The Approach.

In this project a revolutionary approach to biofluidics was explored by developing Biofluidic Intelligent Processor (BIP) devices in which:

- Flow occurred in a completely new size regime (10 – 100 nm);
- The biomolecule itself was integral to the biofluidic transport;
- Active control of fluid transport accomplished digital transfer of fluids;
- The interconnect itself was integral to the intelligent movement of biomolecules; and
- Digital transport renders molecular manipulations insensitive to environmental disturbances.

The device was intended to drill down to the size regime of interest from the macroscopic world by using a ‘conventional’ microchannel as a front-end pre-separation or molecular sorter. All of the nanoscale fluidic manipulations were accomplished in a series of parallel intelligent membranes, or ‘molecular gates,’ developed at UIUC. Each gate consisted of a nanocapillary array (NCA) membrane. By careful design of the molecular and supermolecular architectures of each of the individual gates, transport rates were determined by the applied conditions, the electrokinetic flows, and the presence and identities of the biomolecules of interest. Because transfer between adjacent compartments occurred either for all or none of the target species, the biofluidic control established was digital, and therefore insensitive to environmental perturbations.

### 2.2 The Results

The work plan for this project was divided into three main tasks: 1. Transport, 2. Fabrication, and 3. Interfacing and Operation. The detailed report which follows is organized by these three tasks. The major findings and outcomes are presented in an integrated fashion. The highlights of work carried out during the current project period include:

- The demonstration and characterization of digital flow switching mediated by nanocapillary array membranes in three dimensional microfluidic/nanofluidic hybrid architectures. The reversal of the polarity of forward- and reverse-bias upon going from large pore diameter ( $d > 100$  nm) membranes to smaller pore

diameter ( $d < 50$  nm) membranes demonstrated how the properties of both nanochannels and microchannels must be considered in understanding flow switching.

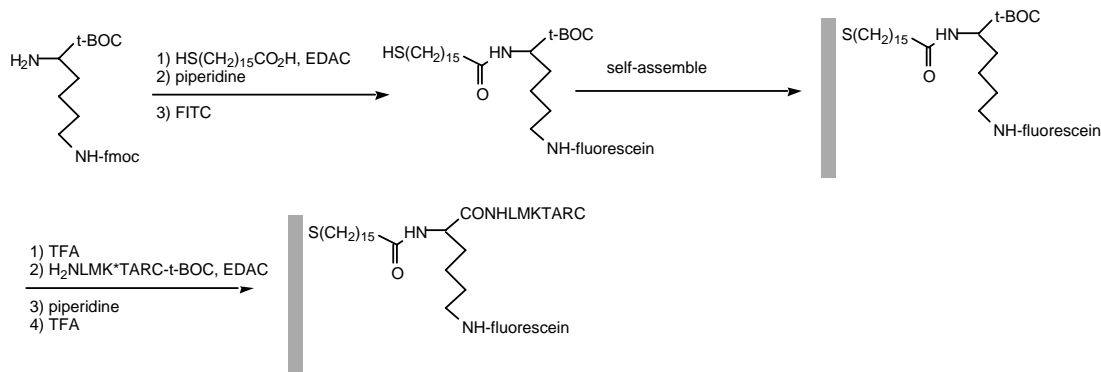
- The role of surface charge density in controlling the quantitative flow characteristics was studied in detail. Under conditions of comparable driving voltages, larger surface charge densities resulted in higher volume transport rates.
- Size-dependent molecular transport was demonstrated. Molecular size cutoffs were measured for 15 nm pore diameter membranes with fluorescently-labeled dextrans of varying molecular weight. Two-component mixtures were intelligently switched based on recognition of the molecular size. Hindered transport, similar to the phenomenon of hindered diffusion, was observed when the hydrodynamic radius approaches 0.1-0.2 of the channel diameter.
- Techniques were developed which allowed complex three-dimensional multiple molecular gates and arrays to be fabricated in precisely aligned multilayer architectures with efficient self-aligned fluidic vias. Communication among the vertically separate reservoirs and molecular gate nanocapillary array membranes, fabricated from polycarbonate, established digital fluidic switching among the vertically separated analytical channels.
- Unique multilayer architectures, comprised entirely of polymethylmethacrylate, were developed to circumvent the thermal and pressure induced cracking problems associated with melding together disparate materials such as glass, polycarbonate and silicon.
- All of the analytical unit operations needed to accomplish multidimensional chemical analysis relevant to the early detection of biologically derived neurotoxins were established and characterized, which included: injection, electrophoretic separation, band collection and analyte derivatization. The sequential binary operations of electrophoretic separations followed by band collections were also demonstrated.
- The volume transfer rate under forward bias conditions scaled linearly with applied potential and monotonically with pore diameters, whcih provided *qualitative control* over transfer rates.
- Quantitative transfer measurements indicated the conditions under which transfer could be accomplished with 100% mass efficiency ( $d = 200$  nm,  $V > 80$ V). Based on these measurements nanocapillary array membranes were used as injectors for flow injection analysis (FIA) and for capillary electrophoretic (CE) separations. Furthermore, the quantitative transfer was used to establish automated band collection for *attomole-level preparative chromatography*. Pre-selected bands were recognized and then collected under computer control.

- Reactive mixing experiments established that the injection of one component of a reactive pair into a microfluidic channel containing a reactive partner could be accomplished in the low millisecond time regime. Kinetics of the *o*-phthalodialdehyde-glycine reaction monitored *in situ* indicated the potential for using this configuration for stopped-flow kinetic measurements with femtomole sample amounts.
- Highly efficient approaches to fabricating single nanopores and small arrays of precisely placed nanocapillaries were developed. Focused ion beam milling was used to produce nanometer scale cylindrical pores and polymethylmethacrylate thin films. The films were then released from sacrificial silicon carriers and mounted in the microfluidic-nanofluidic hybrid structures.

### 3. TRANSPORT

#### 3.1 Synthesis of the Affinity Tag

Usable quantities of the labeled heptapeptide HSR'-LMKTARC, where R denoted the fluorescently-labeled linker portion of the molecule, were first synthesized and then used in the testing of the molecular gate construct of the to micron scale delivery channels.



Scheme 1

The original strategy for the synthesis is outlined in Scheme 1, but the reaction order in this scheme was altered. The heptapeptide portion of the molecule was fabricated by purely solid-state synthesis techniques in good yield (~ 100 mg). Coupling of the mercaptohexadecanoic acid (MHDA) (HS(CH<sub>2</sub>)<sub>15</sub>CO<sub>2</sub>H) to the derivatized lysine was performed next, prior to the assembly of the MHDA on the Au surface. From experience with similar surface-directed peptide coupling reactions, it was determined that much better coupling efficiency could be attained if the reaction was carried out prior to being coupled to the Au. The conditions for the coupling reaction, which had not yet been optimized, resulted in the acquisition of 1.5 mg of the product at 90% purity and 500 µg at 80% purity.

While 1.5 mg (1 x 10<sup>-6</sup> mole) of MHDA were sufficient to begin the initial experiments on model planar and cylindrical geometries, further refinements of the reaction were necessary to improve both the yield and the purity. Initial efforts to improve yield

examined the release pf the peptide reagent from its carrier at an earlier point in the reaction sequence, thereby mimicking conditions used to produce thiol-labeled latex particles. Purification experiments pursued binding the partially purified reaction product to copper (Cu) beads as a mechanism to separate the thiol-containing species from the unreacted peptide. Once separated, the affinity interaction was broken by chemical oxidation, which was then followed by the physical separation of the beads from the reaction product, and lastly the purified reagent was re-reduced.

It must be emphasized that even 1  $\mu$ mole of reagent was sufficient to accomplish a number of experiments. The crossed channel geometry demonstrated below accesses on the order  $10^5$  cylindrical channels. Using 15 nm diameter channels and a saturation surface density of  $10^{-10}$  mole  $\text{cm}^{-2}$  required 25 pmole ( $25 \times 10^{-12}$  mole), even if the efficiency of reagent delivery and reaction was only 0.001. Thus, 1  $\mu$ mole would yield enough of the Biofluidic Intelligent Processor agent to completely derivatize 40,000 samples under these conditions. Although the efficiency of these sample handling steps was not known without coating the interior of a channel, the calculations conveyed that even though the absolute amount of reagent in-hand was small, the areas to be derivatized required negligible amounts of reagent, a direct benefit of operating at the nanoscale.

### 3.2 Botulinum Neurotoxins Type A(BoNT/A) Affinity Tag

Further efforts were then taken to improve the yields and the purity in the synthetic preparation of the nanoaffinity heptapeptide complex. The synthesis was repeated on a half-scale, followed by splitting the starting material (fluorescently tagged peptide) into thirds. The first third was used for a mercaptopropionic acid-succinimidyl ester derivative coupling trial. Mass spectrometry confirmed the presence of the target species and impurities in this trial. The impurities resulted from side reactions of the coupled thiol to the other sulfur containing species (both cysteine and methionine) through dithiol exchange reactions. For this reason, the second batch of the synthesis was subjected to thiol derivatization via a protected thiol species (S-acetylthioglycolic acid N-hydroxysuccinimidyl ester) with the succinimidyl ester, which provided coupling to the

N-terminus of the fluorescently tagged octapeptide still bound to the resin. After removal from the solid-state resin, the resulting peptide/fluorescein/thiol specie was de-protected with hydroxylamine. This de-protection after detachment was designed to avoid side

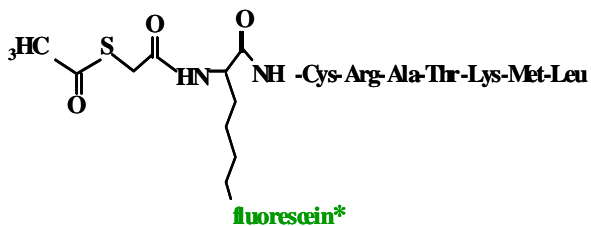


**Figure 1. BoNT/A affinity tag with protected thiol group.**

reactions during the coupling step. The formation of the protected thiol species (Fig. 1) was achieved in reasonable yield (~15%) and purity. A total of 400  $\mu$ g of the target affinity tag was obtained.

### 3.3 Size-dependent Gate Performance

Effective electrokinetic transfer from a Polydimethylsiloxane (PDMS) microfluidic channel to another microfluidic channel across a nanoporous molecular gate, independent of molecular size up to 2 MDa, (Da=Dalton, unified atomic mass number) had been previously demonstrated. Because reproducible behavior was achieved for the 200-nm pore diameter polycarbonate track-etch (PCTE) membranes, these pore-diameter membranes were targeted for the first molecular gate (molecular valve) within the Biofluidic Intelligent Processor (BIP). The next critical goal was to show size-dependent transport discrimination necessary for the third, and final, (mass selective) molecular gate of the BIP. Initial efforts with 15-nm pore diameter PCTE membrane gates showed no observable transport of a 2 MDa dextran (Figure 2). This pore-diameter dependent gating established a firm foundation for the use of these molecular gates as a digital fluidic transport gate with size discrimination.

Further interrogation of macromolecular (2 MDa dextran) transport across various pore-diameter membranes has been pursued using 100-nm pore-diameter membrane gates.

The preliminary results are depicted in Figure 3. The initial electrokinetic transport was noticeably slower in approaching a steady-state transfer value. Furthermore, the

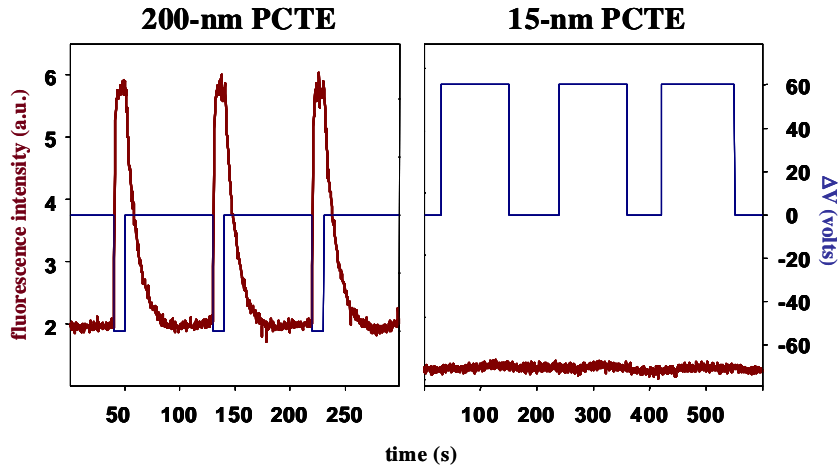


**Figure 2. 2 MDa FITC-labeled Dextran transport.**

Pore-diameter dependent gating. fluorescence intensity and applied bias as a function of time for 2 MDa FITC-labeled Dextran transport across (left) 200-nm pore diameter PCTE membrane and (right) 15-nm pore diameter PCTE membranes.

fluorescence intensity values show significantly lower concentration transfer efficiencies than for the larger pore diameters. These results can be interpreted in light of literature studies of electrokinetic transport of proteins across PCTE membranes, in which the Stokes radius is thought to be the determining factor in the electrokinetic transport within nanopores. Although solution characteristics affect Stokes radii, values for the 2 MDa dextran species have been reported to be approx. 40 nm. The ratio of 2.5 was within the range of the pore-diameter to Stokes radius ratio reported to be competent to support transport, and in agreement with literature studies of bulk transport.

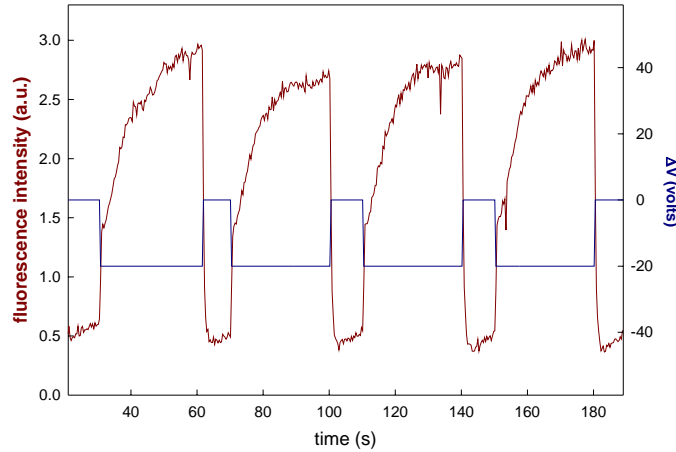


**Figure 3. Transport across a 100-nm pore diameter membrane.**

Fluorescence intensity and applied bias as a function of time for 2 MDa FITC-labeled dextran transport.

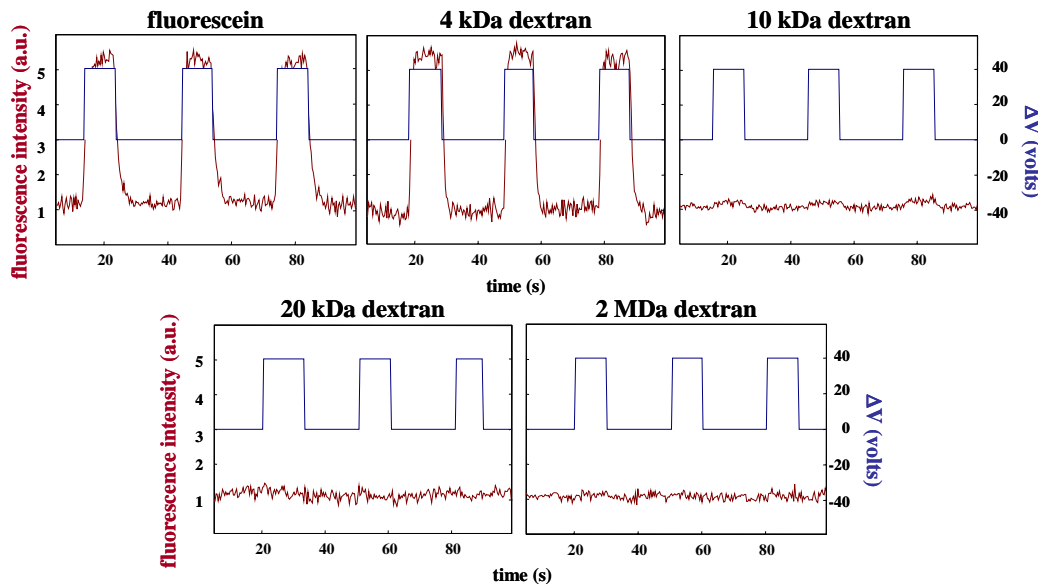


**Figure 4. Mass-diameter dependent gating.**

Fluorescence intensity and applied bias as a function of time for transport of small molecular and FITC-labeled Dextran of various molecular sizes across 15-nm pore diameter PCTE membrane.

To understand the effect of molecular size on electrokinetic transport better, a specific molecular weight cutoff value was needed for a given pore-diameter. A molecular cutoff weight of approximately 20 kDa had been proposed for the effective separation of affinity tag from the affinity tag/botox species. Building on the pore-diameter dependence work, molecular transport for the 15-nm pore diameter molecular gate was

interrogated by a series of Fluorescein Isothiocyanate (FITC)-labeled dextrans with varying molecular size (Figure 4). The 4 kDa dextran specie was transported with the same relative efficiency as the small molecular weight fluorescein probes. However, for the 10 kDa dextran sample, a significant decrease in transport efficiency was observed, and dextrans of 20 kDa and higher molecular weight showed no discernable transport, indicating the critical ability to discriminate the affinity tag alone (2 kDa) from the affinity tag with bound BoNT/A (52 kDa).

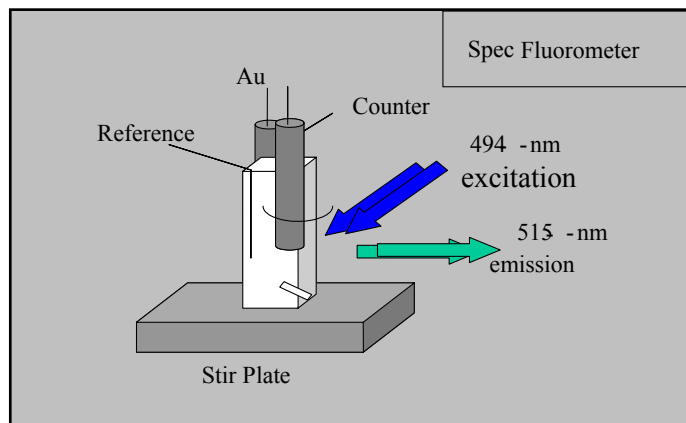


**Figure 5. Schematic of *in situ* fluorescence and electrochemical measurements.**

The electrochemical cell was placed inside the fluorometer, and a stir bar was in the cuvette to enhance mixing.

### 3.4 Affinity Tag Desorption.

Since the amount of synthesized affinity tag compound was limited, the adsorption and electrochemical desorption on gold (Au) surfaces of similar heptapeptide preparation reaction products was evaluated. Because the crucial determinant for Au adsorption was the thiol group, a working adsorption/desorption protocol from a similar compound was relevant to the final affinity tag.

A fluorescence spectrometer was coupled with the electrochemistry measurement to monitor the desorption process (Figure 5). The whole electrochemistry cell was placed

inside the fluorometer. A bulk gold (Au) electrode was dipped in a 0.5 mM solution of the model compound (HS-GK(FITC)-CRATLKM) for 2 hr, then rinsed thoroughly with water and 0.2 M  $\text{KF}_{(\text{aq})}$ . Upon insertion of the electrode, the fluorescence intensity increased due to desorption of the physisorbed tag molecules, but there was no significant increase in the intensity when electrochemical desorption was triggered (at 10 min.). However, a clear reduction peak was observed in the first cyclic voltammogram (CV), which indicated that electrochemical desorption took place (Figure 6).

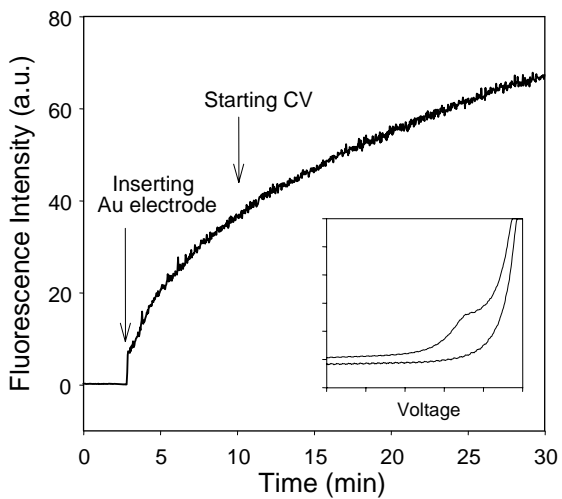


**Figure 6. Fluorescence intensity as a function of time.**

The insert is the cyclic voltammogram of the first cycle at the 10-minute mark.

The expected amount of adsorbed target compound was  $5 \times 10^{-12}$  moles, but the detected amounts were  $1 \times 10^{-9}$  and  $8 \times 10^{-12}$  moles from fluorescence and electrochemistry, respectively. It was encouraging that the mass amount from CV was close to the expected monolayer coverage. However, the number of moles determined from the fluorescence measurement was more than 2 orders of magnitude higher than determined by the electrochemical measurements, which indicated a large amount of physisorbed, and thus not electrochemically active, tags.

### 3.5 Electrochemistry in the Microdevices.

The electrochemical system was integrated into several microdevices to evaluate different designs based on the respective electrochemical performances. Figure 7 shows one of the first designs. Platinum (Pt) electrode patterns were sputtered directly on the PDMS surfaces, and electroless Au plated membrane were then inserted during assembly (Figure 7a,b). Clearly, the elastic nature of PDMS did not make it a good sputtering target, which resulted in a significant number of mechanical defects when the layers were peeled off the masks. Improved sputtering integrity was obtained when the PDMS layer was sealed to a glass substrate prior to sputtering. Subsequent cyclic voltammograms were performed, and  $\text{Fe}(\text{CN})_6^{3-/\text{4-}}$  in 0.2 M  $\text{KF}_{(\text{aq})}$  was used as standards to test the performances of the micro-electrochemical systems.

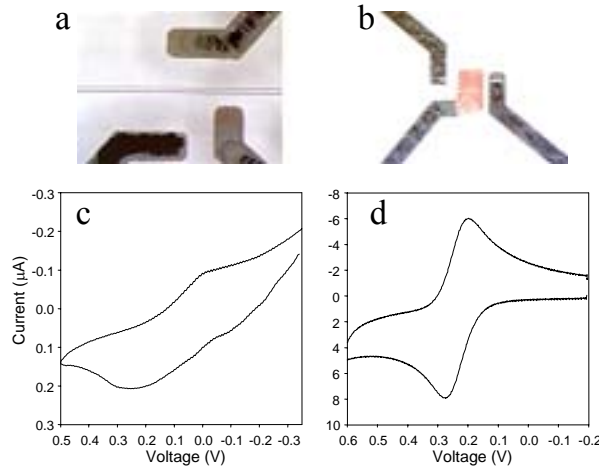


**Figure 7. Electrochemistry from the microfabricated devices.**

(a) Photograph of a Pt electrode pattern on the PDMS layer with a horizontal microchannel. (b) Photograph of an assembled device with a piece of Au membrane connected to one of the Pt leads. (c)&(d) cyclic voltammograms of  $\text{Fe}(\text{CN})_6^{3-/\text{4-}}$  for a microdevice (c) and a bulk Au electrode (d) in 0.2 M  $\text{KF}_{(\text{aq})}$ . The scan rate was 200 mV s<sup>-1</sup>.

Figure 7c is the CV with the Au membrane working electrode, and the reference and counter electrodes were Pt. The change in potential ( $\Delta E_p$ ) was 250 mV in the chip-based cell and *ca.* 75 mV for the bulk Au electrode (Figure 7d). The slower kinetics inside the microchip was expected from the high resistance of both the buffer and the electrodes.

### 3.6 Improvements in the Affinity Tag Synthesis.

The synthesis of the labeled heptapeptide shown in Figure 8 was completed at very low yields ( $1.5 \text{ mg} = 1 \times 10^{-6} \text{ mole}$ ). The reaction was further refined to improve both the yield and the purity. The synthesis had previously encountered obstacles associated with the solid-support build-up of the fluorescently labeled affinity tag. The products of several previous synthetic runs were characterized by DIOS-MS mass spectral analysis. Mass spectra before and after the seventh amino acid incorporation showed masses that

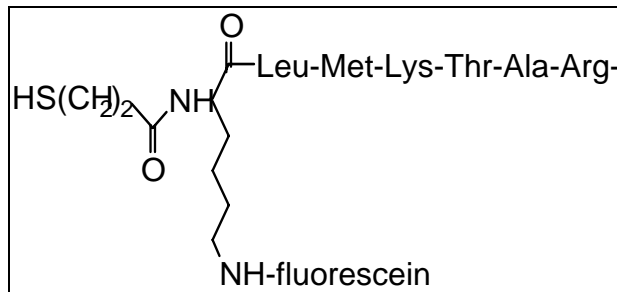


**Figure 8. Labeled heptapeptide.**

could not be easily assigned to possible peptide side products that occurred in this last step. Previously steric hindrance was suspected as the cause. Previous syntheses had added a fluorescein-derivatized lysine on the N-terminus, which was required for thiol addition. The synthesis route was then changed to introduce an underderivatized lysine at the N-terminus, followed by addition of the fluorophore. However, use of the standard fluorescein isothiocyanate chemistry still did not yield the correct product. A succinimidyl ester of fluorescein was then used to give the desired peptide product in good yield, as determined by Matrix Assisted Laser Desorption Ionization-Mass Spectrometry (MALDI-MS).

### 3.7 Size-dependent Gate Performance.

A key design goal of the first molecular gate (molecular valve) was to show that analyte species may be transferred across it independent of molecular size. Preliminary data with one series of structures (FITC-labeled dextrans of varying molecular weight) were obtained using 200-nm pore-size PCTE membranes in a PDMS microfluidic device. The lowest of the molecular weights in this series (4,000 Da – Fig. 9a) showed relatively fast electrophoretic transport into the detection region (directly at the gate in the receiving channel), as well as fast diffusion in the buffer solution (away from the detection area)

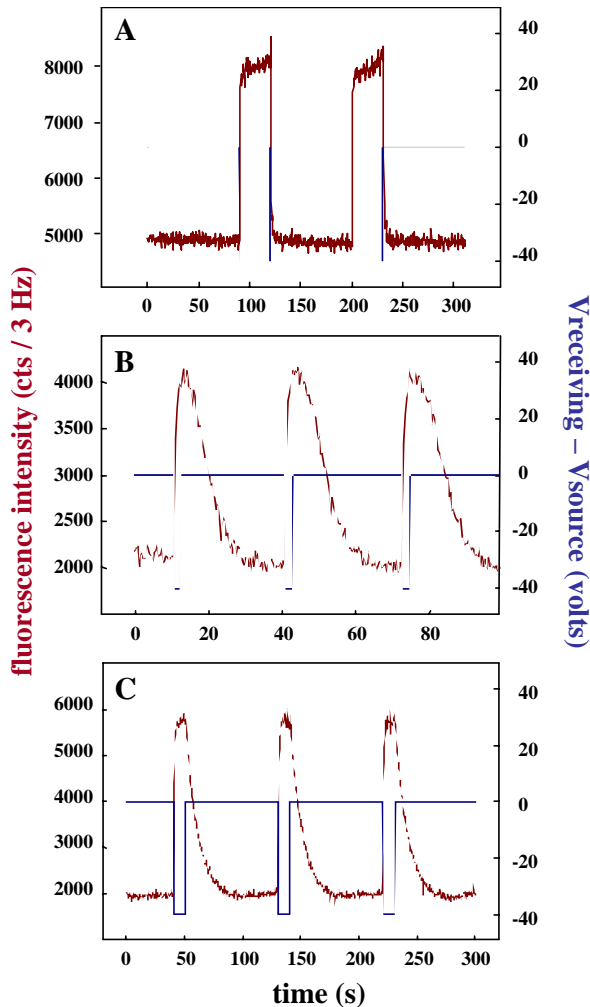


**Figure 9. Uptake of probe as a function of gating potential for fluorescein-labeled dextrans.**

Molecular weight (a) 4 kDa; (b) 10 kDa; and (c) 2 MDa.

after the transport potentials were turned off (system completely grounded). These data were analogous to that previously reported with low molecular-weight fluorophores such as fluorescein. The 10,000 Da FITC-labeled dextran series (Fig. 9b) was also characterized by rapid transport through the PCTE membrane, but with a slower diffusional component after the transport potentials were grounded. This result was expected, because the rate of diffusion depended on the molecular weight. In fact, much shorter transport times were necessary to observe this discrete plug transfer. At longer transfer times, this diffusional component extended even further out in time (larger plug to equilibrate with the buffer). Demonstration of mass-independent molecular gate function up to 150,000 Da was shown by the transport of 2,000,000 Da FITC-labeled dextran in Fig. 9c. Once again, the profile was composed of the rapid electrophoretic transfer of this large molecule across the membrane, with a slower diffusional component associated with equilibration with the buffer solution in the receiving channel. Experiments with 75 kDa and 250 kDa labeled dextrans followed the same general trends. Taken together these experiments demonstrated that effective electrophoretic transfer from PDMS across a nanoporous molecular gate was achieved that was independent of molecular size up to 2 MDa.

### 3.8 Memory Effects

Memory effects in the nanopores were investigated. Parameters such as the polarity of the gating potential, timing, polarity sequences (pos-neg vs. neg-pos vs. neg-neg, etc.), and concentration of analyte all have important influences on the observed response. Detailed, strictly controlled experimental design allowed for the interrogation of all of these important factors. One example was the polarity sequence. If the “wrong” polarity was applied first, then a buffer plug was moved from the receiving channel into the analyte-containing source channel. The subsequent transfer of analyte then depended on the time allowed for equilibration of concentration in the analyte channel. The membrane was reconditioned by the application of sufficiently lengthy pulses of the correct polarity. The reproducibility of transport (even with 2MDa dextran) was characterized, and even without extensive optimization, was  $\pm 15\%$ . This led to the postulation that these gates

could be developed as a novel injection method for microfluidic chip-based separations, in addition to the designed collection functions. Although the computer-control protocols ultimately prevented the accidental applications of the incorrect polarity sequence, it was helpful to understand the consequences.

### 3.9 Au-coated Nanoaffinity Gates.

Au was electrolessly deposited on the membrane surfaces and pores, and the electrical and electrochemical properties of the Au-coated pores were characterized by cyclic voltammetry (CV) and surface conductivity. The reductive desorption of organothiol from pores was also studied. To obtain signals from the pore surfaces only, strategies were developed that confined the exposure of the membranes to only the pores. The concept of affinity gating by using amino thiols as the gating agent was then demonstrated. The neutral bodipy fluorophore used in the transport task was determined to be a suitable amine-reactive probe, since it could bind to the thiol on Au-coated pore surfaces, and then be detected with laser-induced fluorescence once it was electrochemically desorbed from the surface.

### 3.10 Nanoaffinity Complex

The synthesis of the nanoaffinity heptapeptide complex was successful up to the coupling of the fluorophore to the N-terminus of the lysine-derivatized peptide, as verified by the correct mass of the major product by mass spectrometry. This was a positive step; since it overcame the obstacles associated with the solid-support build-up of the fluorescently labeled peptide, and provided the required material, *i.e.* thiol and peptide, to complete the final coupling reaction. The newly derived small-scale synthesis reaction yielded 10 mg of the fluorescently tagged peptide. Unfortunately, the initial effort to couple the thiol to the heptapeptide tag yielded an unknown product. Further mass spectrometry work revealed that the N-terminal protecting group (Dde) was not removed, and thus the mercaptopropanoic acid was not attached. Ongoing work then focused on repeating the synthesis on a small scale and implementing other protocols to remove the Dde. Because

the removal of the protecting group was easily confirmed by mass spectrometry, it was certain that the Dde was removed before the final coupling reaction was attempted.

### 3.11 Au-coated Nanoaffinity Gates

Electrochemical desorption of tag molecules from Au-coated nanopore surfaces was successfully demonstrated, a pivotal step towards the detection of the release of affinity tag-analyte complexes. Gold-coated membranes were fabricated from electroless depositions of Au onto polyvinylpyrrolidone-coated polycarbonate (PCTE) membrane

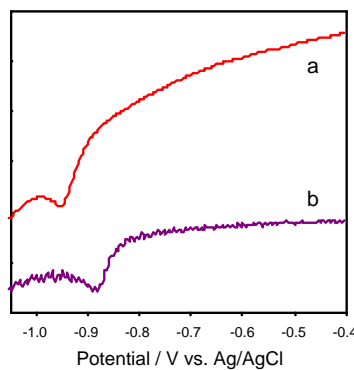


**Figure 10. Reductive scans (Current (a.u.) v. Potential) of adsorbed 1-hexadecanethiol.**

(a) Au-coated nanopore surface, and (b) bulk Au electrode in 0.1 M KOH<sub>(aq)</sub>.

surfaces in a flow cell, which ensured the coating of Au on the interiors of the pores, as well as on the outer membrane surfaces. The Au films were removed from the outer surfaces by peeling from one side of the membranes before the membranes were soaked with 100  $\mu$ M thiol in 0.1 M KOH/EtOH for 1 hour. The Au films on the other outer surfaces were retained for electrical contact, as the films were protected from exposure to thiol, and then cyclic voltammetry was performed to measure the adsorbed thiol on the Au-coated pore surfaces in aqueous solution. Figure 10 shows the reductive desorption scans of 1-hexadecanethiol (HDT) from a nanopore membrane electrode and a bulk Au electrode in 0.1 M KOH<sub>(aq)</sub>. The desorption peak of HDT from the nanopore surface was slightly (75 mV) more negative than that from the bulk Au electrode, indicating that

the electroless coated Au was microscopically smoother than the mechanically polished Au surface, thereby yielding a thermodynamically more stably packed adsorbed thiol layer in the nanopores. With this successful scheme, the electrochemical desorption of affinity tags with the affinity gate inside the 3-D microfluidic system was carried out.

### 3.12 Transport Rate and Efficiency

The continuous effort of understanding and controlling transport through nanoporous molecular gates yielded significant results. The same cross-channel PDMS/nanopore/PDMS three-dimensional design as previously reported was used. The

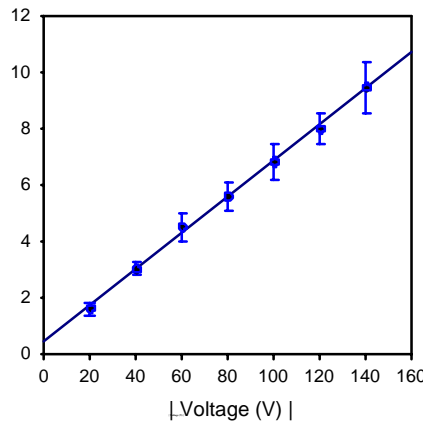


**Figure 11. Relative transport rate of fluorescein vs. absolute bias (Transport Efficiency (%) vs. Voltage) in a 200-nm device.**

The receiving channel was initially filled with 5mM PBS at pH 8.

transport efficiency was systematically studied with both 15 and 200 nm PCTE membranes (Figs. 11 and 12). To avoid interference from the fluorescence signal of the source channel at the intersection, the signal was detected from the receiving channel area

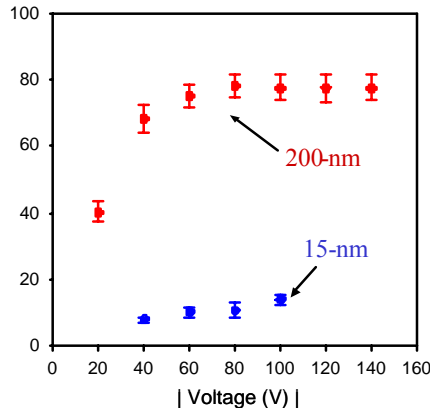


**Figure 12. Transport efficiency (%) of fluorescein vs. absolute bias in the PDMS devices.**

15-nm (blue) and 200-nm (red) PCTE membranes, The same experimental conditions as in Fig. 11.

200  $\mu\text{m}$  displaced from the intersection. The transport rate was obtained by calculating the total intensity normalized to forward bias duration, while the transport efficiency was based on signal height only. Transport efficiency was defined as  $N_{\text{trans}}/N_{\text{total}}$ , where  $N_{\text{trans}}$  was the number of analyte molecules transferred to the receiving channel, and  $N_{\text{total}}$  was the total number of analyte molecules passing the membrane during measurement. These devices exhibited linear transfer rate with bias for 15 nm and 220 nm pore sizes, indicating normal electrokinetic flow, i.e.  $v \propto E$ . Note: the 15-nm membrane devices possessed significant electrical capacitance, which complicated the I-V behavior after the initial rise of the signal for longer durations ( $> 5$  seconds). Therefore, the transport rate data was not reported here. For the 200-nm PCTE devices, the transport efficiency was nearly 80% with a bias  $\geq 60$  V, while it was only  $\sim 15\%$  with the 15-nm membranes. This result indicated only a minor loss of analyte was obtained when operating with a larger pore size membrane.

### 3.13 Molecular Transport Gating Functions

Previously a significant milestone was met by the preliminary demonstration of the mass-independent gating function shown by a series of FITC-labeled dextrans up to 2 MDa.

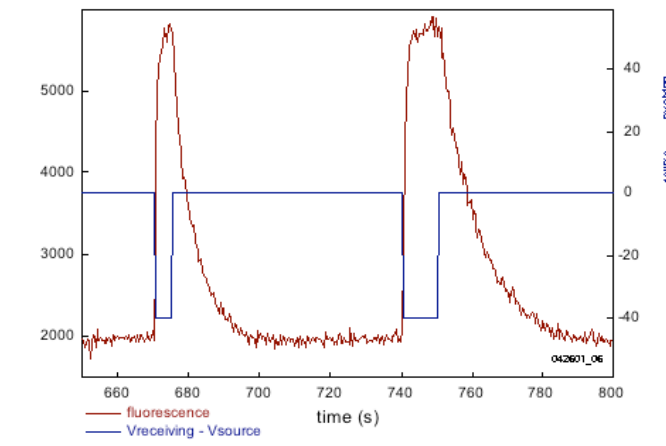


**Figure 13. Molecular transport of 2 MDa FITC-labeled dextran across a 200-nm pore size membrane in a 3-D PDMS/PCTE/PDMS structure.**

These transport profiles (Figure 13) were further reproduced with an emphasis on understanding the dynamics related to active transfer across the gate. Preliminary analysis of the fast rise times associated with a number of different size dextrans showed similar (relative to experimental parameters) average rise times. Thus, it appeared that the speed of transfer across the gate was largely independent of molecular mass.

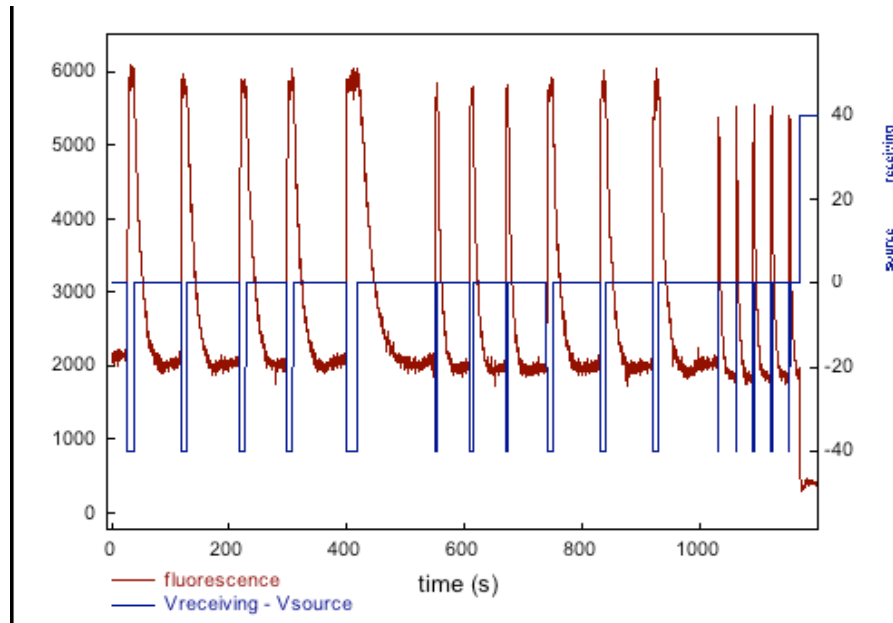


**Figure 14. Reproducibility of analyte injection into the receiving channel tested with 2 MDa FITC labeled dextran under varying transport conditions.**

Reproducibility for the transport of the large molecular weight dextrans was also studied (Figure 14). Earlier the reproducibility was estimated by peak areas to be approximately  $\pm 15\%$ . When normalized against the computer recorded time for voltage bias (area/time of injection), the reproducibility of transport for the 2 MDa dextran species was seen to decrease to  $\pm 3.6\%$  for 2sec voltage biases and  $\pm 5.4\%$  for the 10 sec voltage biases. The non-optimized reproducibility of the molecular transport of these large molecules resulted in the implementation of these active molecular gates as a novel injection method for microfluidic chip-based separations. Efforts in this area focused on the characterization of analyte transport for the development of the molecular gate sample injectors and the outcome on the resulting microfluidic separations. Newly designed channel constructs using optimized photolithography protocols were incorporated into these three-dimensional separation devices. Molecular gates collectively implemented in both the injection and collection modes delivered unique preparative and analytical manipulations associated with microfluidic separations of extremely low volumes.

An important consideration in hybrid micro/nano fluidic architectures was the time for mixing after the introduction of a switched stream into a receiving channel. Previously a cross channel system was used to investigate the mixing of fluids from the source channel with fluids in the receiving channel by monitoring the distribution of transported probes along the receiving channel with a fluorescence microscope. The fluorescence intensity profile along the receiving channel was monitored as a function of time. When the transport was turned on, the gradient of fluorescence intensity along the channel within the observing length reached steady state in less than 3 sec, and the intensity variations among the following temporal sections were negligible. The actual measured difference was 5% between the two ends of the profile at steady state. In these hybrid architectures the nanofluidic interconnects behaved like a nanomixer with the bulk electroosmotic flow driven behind it. Given an average distance of 0.6  $\mu\text{m}$  between two adjacent pores, and a typical diffusion coefficient  $D = 5 \times 10^{-6} \text{ cm}^2 \text{ sec}^{-1}$ , 0.36 msec would be required for molecules to diffuse one inter-pore spacing, which set the upper limit on mixing time. However, in these structures flow was driven electroosmotically, and for a typical flow

velocity of  $400 \mu\text{m sec}^{-1}$ , homogeneous mixing would be reached in less than  $0.2 \mu\text{m}$  from the intersection of two channels. Mixing was extremely fast with this nanofluidic interconnect, which provided an efficient way to manipulate chemical reactions inside these microdevices.

### 3.14 Nanoaffinity Channels

Electrochemical desorption of 1-hexadecanethiol from Au coated nanopores was previously demonstrated. Next the parameters of the electroless Au plating process were investigated to optimize the overall process to obtain reproducible Au coated nanochannels. Time dependent Au plating studies were carried out in both bath and flow methods. In the bath method, the pretreated membranes were placed in the Au plating solutions. In the flow method, the membranes were sandwiched in a flow cell to ensure the Au plating solution flow through the nanopores. Figure 15 shows several scanning

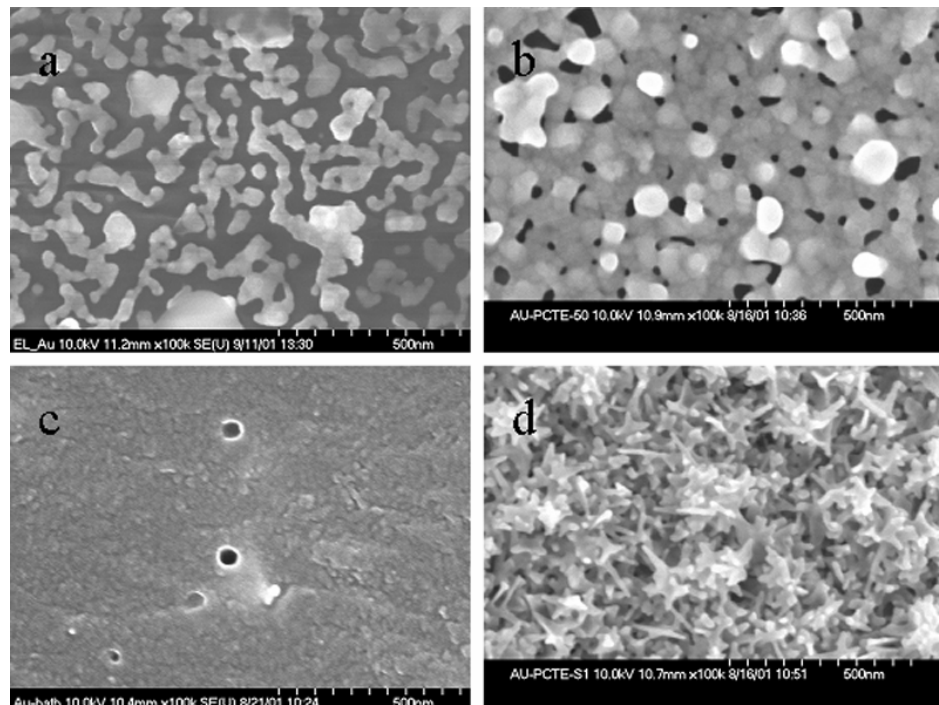


**Figure 15. Scanning electron micrographs of electroless Au plated 50-nm pore diameter membranes.**

(a). 15 minutes in the plating bath. (b). 4 hours in the plating bath. (c). The same membrane from (b) after the surface gold layer was peeled off. (d). 4 hours in the flow cell.

electron micrographs of the morphology of Au-coated membranes under various conditions. A discontinuous Au film was formed on the surface when the plating times were less than 30 min (Fig. 15a). Such films were undesirable, since the morphology would be expected to cause problems in performing electrochemical desorption. There were differences in surface morphology between the bath and the flow plated Au membranes, as shown in Figs. 15(b) and 15(d), which likely resulted from the faster mass-transport controlled deposition in the flow method compared to the diffusion controlled bath method.

The Au coated membranes were also integrated into the cross-channeled PDMS transport device. In the preliminary tests, no significant differences were observed in the assembly compared to that with non-treated PCTE membranes.

### 3.15 Affinity Tag

The synthesis of the nanoaffinity heptapeptide complex on a small scale was examined in more detail. Separate trial protocols to remove the Dde were begun by dividing the fluorescently tagged octapeptide into four equal samples. One of the four protocols was successful in producing a large yield of the final product, but it was accompanied by significant impurities. The best estimate for the mass yield of final product in this trial run was 1 mg (added to the 1.5 mg previously obtained). Finally after exhaustive efforts to synthesize the affinity tag at the UIUC Biotechnology Center, a few milligrams of affinity tag were synthesized. This amount was enough to be incorporate into a large number of devices. The probability of success of this technology was enhanced by a full working knowledge of nanoaffinity gating, for which an amount of tag sufficient to perform large volume assays was desired. Subsequently the synthesis of this affinity tag was contracted to American Peptide (Sunnyvale, CA) in an effort to improve affinity tag amounts. An initial quantity of 14 mg was provided at >80% purity, followed by 86 mg of > 90% purity.

### 3.16 Pore-size Measurement Devices

Decoration of the interior of the nanopores with Au must be followed by an accurate assessment of pore size to achieve the proper electrokinetic flow properties. A pore-size measurement device was constructed based on the Knudsen flow of gas through channels. The critical components consisted of a mass flow meter/controller and two capacitance manometers to measure the differential pressure across the membrane (Figure 16). The upstream capacitance manometer had a working range of 1 to 1000 Torr, while the downstream capacitance manometer had a working range of 0.001 to 1 Torr. The mass flow controller had an upper limit of 10 sccm. The system was evacuated through the use of a turbomolecular pump backed by a single stage rotary vane rough pump. A vacuum valve was placed between the pumping system and measurement cell, which allowed a flexible experimental arrangement. For example, with the valve open, continuous evacuation of the downstream side allowed steady-state pressure

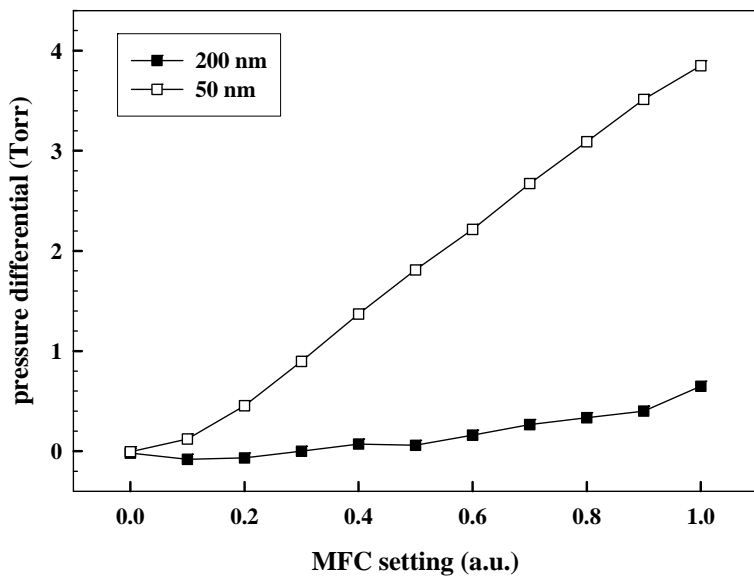


**Figure 16.** Scanning electron micrographs of electroless Au plated 50-nm pore diameter membranes.

differentials to be formed across the membrane. In another configuration, the system was evacuated, the valve (and thus pumping) shut off, and the upstream side was pressurized. This allowed the time dependence of pressure equilibration, which was dependent on the pore diameter, to be measured. These two types of experiments were investigated to optimize the range of pore sizes over which measurements could be made.

Initial experiments targeted larger diameter (50 nm to 200 nm) PCTE membranes, primarily because these were the pore diameters used for electroless Au plating and nanoaffinity gate immobilization. The steady state pressure differential across the membrane depended on pore diameter, as shown in Figure 16. Less than a 1-Torr difference was measured at a nominal gas flow setting of 1.0 for a 200-nm pore diameter membrane. Conversely, almost a 4-Torr differential pressure was observed for the 50-nm pore diameter membrane at the same flow rate. These data on a non-optimized system were instrumental in characterizing important measurement figures-of-merit, such as the reproducibility and the gas composition dependence.

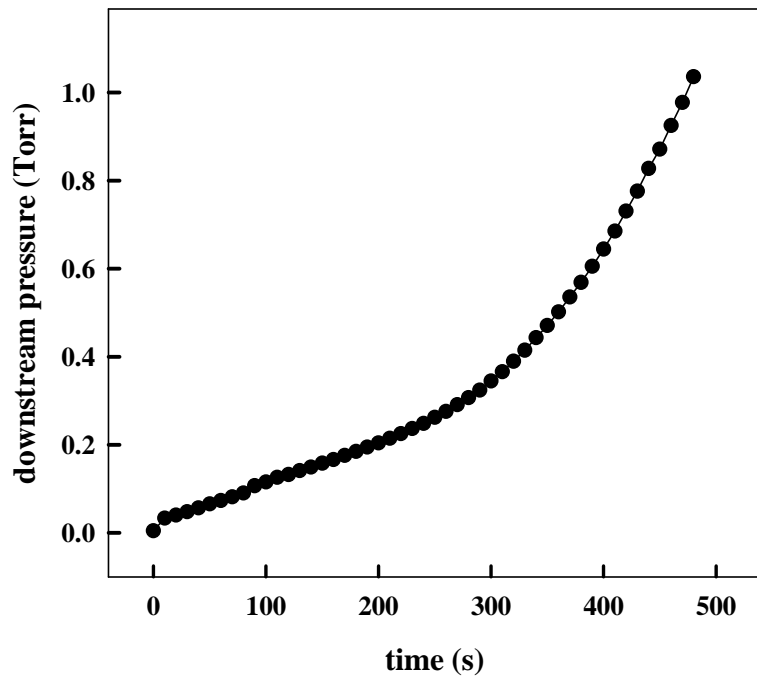


**Figure 17. Downstream pressure as a function of time for a 10-nm pore diameter membrane.**

Although the larger nanopore diameter membranes were targeted for the nanoaffinity gate membranes, the responses of small pore diameter PCTE membranes were also tested. The data for 10 nm diameter pores (Figure 17) showed that equilibrium was not established across the membrane, even for the smallest helium (He) gas flow rate used, which suggested that the nanopores were too small and too resistive to establish equilibrium with the turbomolecular pump. However, the temporal dependence of pressure equilibration showed promise for smaller pore diameters, since a time profile specific for each given pore diameter was obtained. These experiments indicated that with proper analytical protocols, pore-size measurement devices could provide a convenient means to determine the impact of membrane treatments, such as electroless Au plating, have on pore-diameters.

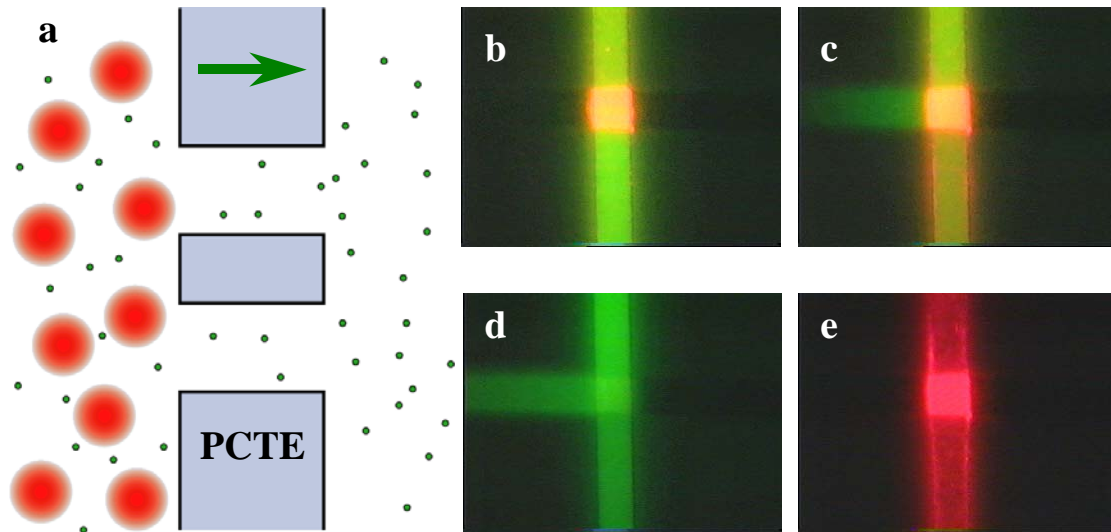


**Figure 18. Size selective transport with two-color detection.**

(a) Schematic of the size selective transport concept; (b) no bias applied; (c) 40 V biased. (b) and (c) were recorded in dual color mode. (d) and (e) were single color detection at 40-V bias.

### 3.17 Size Selective Sampling

Molecular gates with different pore sizes have different mass transport efficiencies and cut-off molecular sizes. To study size selective transport with a mixture of molecules of different sizes, different color fluorescent labels were used to differentiate the fluorescent emission from the probes of different sizes. Figure 18a demonstrates the concept of size selective transport. While large red-fluorescent molecules were stopped by the nanopores, small green-fluorescent molecules easily passed through the nanopores. Nanospheres ( $d \sim 200$  nm) tagged with a red-emitting fluorophore and green-emitting fluorescein ( $\sim 1$  nm in size) were used to show the selective transport through a 200-nm pore diameter PCTE gate. Figures 18b and 18c, recorded with dual-color fluorescence microscopy, demonstrated that effect. Initially the vertical channel was filled with a source solution which contained red-emitting nanospheres and fluorescein, and the horizontal channel was filled with a buffer. In the off-state, fluorescence was not observed in the horizontal channel (Fig. 18b). Upon the application of 40 V bias across the vertical channel and the left side of the horizontal channel, the left horizontal channel started to turn green, which indicated the preferential transport of fluorescein ions (Fig. 18c). Figures 18d and 18e were single color images obtained under 40-V forward bias. The red nanospheres were clearly stopped by the membrane (Fig. 18e), while the fluorescein ions flowed into the buffer channel (Fig. 18d). The red nanospheres tended to collect at the intersection (previously observed sample-stacking effect), but the transport of the smaller fluorescein ions was not hindered. When the bias was reversed, most red nanospheres moved away from the membrane surface by the buffer solution flow from the horizontal channel. This experiment clearly demonstrated that molecular gates could be used to extract selected components from mixtures under static conditions, and were a complement to the electrophoretic sampling experiments discussed below.

### 3.18 Affinity Gate

The initial attempts to carry out electrochemical desorption inside a cross-channel microchip with an affinity gate did not work well because of the poor contact the

electrode pattern made with the Au membrane (Fig. 19a). Meanwhile, sputtering Pt on polydimethylsiloxane (PDMS) also caused the Pt pattern to crack because of the non-

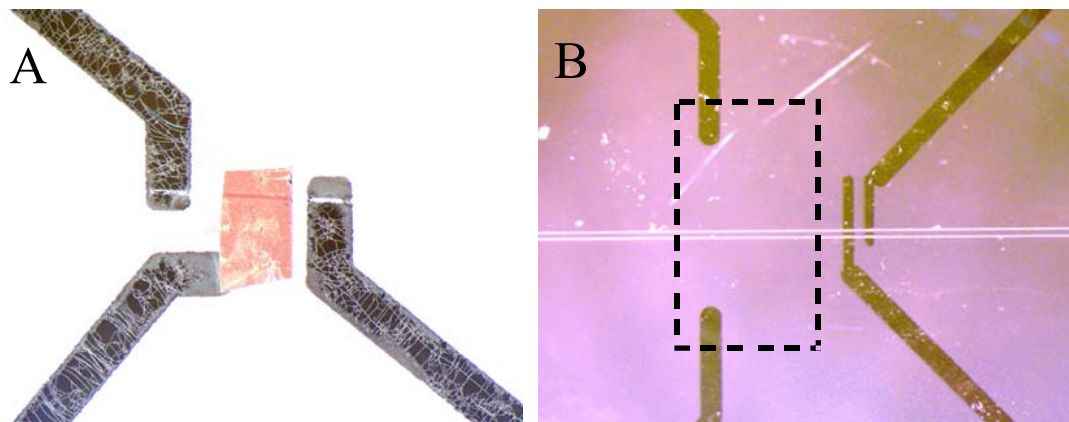


**Figure 19. A. Electrode patterning on PDMS directly. B. New design patterning on glass substrate.**

The dashed square indicates the position of Au plated membrane connected by two Au leads. In both A and B, a horizontal channel contacted all electrodes.

rigid nature of the PDMS elastomer. A different approach was developed in which Au was thermally evaporated onto the etched glass wafer (Fig. 19b). The rigid glass substrate provided a solid support for the electrode leads, and supported the contact between the Au membrane and the electrodes.

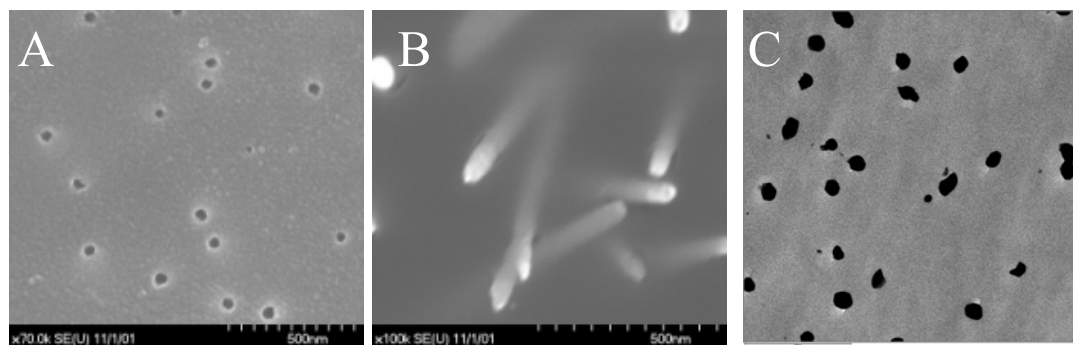


**Figure 20. Electron micrographs of 50-nm pore diameter membranes before (A) and after (B&C) 2 hr electroless Au plating at room temperature.**

A is a SEM micrograph of the surface. B is a SEM micrograph of the surface after peeling off the surface Au. C is a TEM micrograph of a section 2  $\mu$ m under the surface. The horizontal dimensions for the micrographs are (A) 1.18, (B) 0.70, and (C) 1.30  $\mu$ m.

One possible reason for the poor electrochemical results from affinity membranes was the electroless plating process itself. A variety of Au plating conditions were used to process PCTE membranes. The resulting membranes were examined by electron microscopy and pore size measurements. Typical plating conditions (7.7 mM Au solution at room temperature) were expected to result in a Au coating rate  $7 \text{ nm hr}^{-1}$ . Fig. 20 shows electron micrographs of a blank (A) and 2-hr plated membranes (B&C) (50-nm pore diameter PCTE). Transmission electron microscopy (TEM) (Fig. 20C) indicated that these pores contained more Au than had been planned, but the pore size measurements indicated that the pores remained open. It was possible that the fast deposition of Au at the room temperature resulted in a very heterogeneous Au deposition within the pores. By lowering the plating temperature to 3 °C, slower and improved plating results were obtained.

### 3.19 Reaction Profiling

Because of the massively parallel nature of the pore structures in molecular gates constructed from polycarbonate membranes, these gates made ideal passive mixing and reaction components in microfluidic systems. A similar cross-channeled transport construct was used to realize these applications, and the mixing and reaction profiles were evaluated by scanning confocal microscopy (SCM). Figure 21 shows the mixing profile of fluorescein in the receiving channel near the intersection area. Mixing was completed within 100  $\mu\text{m}$  from the center of the intersection, and the channel was 90  $\mu\text{m}$  wide. This was extremely fast compared to currently available passive mixers, which required millimeters to centimeters lengths to achieve complete mixing. At the same time, the ratio of mixing components was defined by the magnitude of applied bias, as was demonstrated previously.

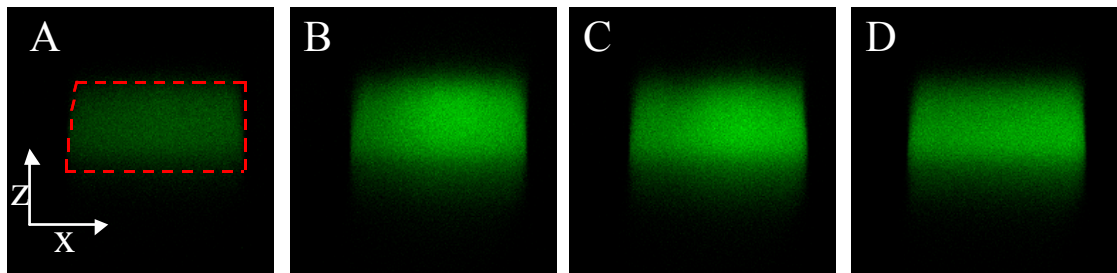


**Figure 21. Cross-sectional SCM fluorescence images of fluorescein mixing.**

The source channel was filled with 4  $\mu$ M fluorescein in 5 mM pH 9 phosphate buffer, and the receiving channel with the buffer only. At injection 100 V was applied to the source reservoir, while the buffer channel was biased for flow (80 V – 0 V). The images are in the xz dimension with the receiving channel, as indicated by the red dash box, perpendicular to the image plane. The images were taken at different y positions (A) 0  $\mu$ m, at the edge of the intersection; (B) 47.6  $\mu$ m, at the center of the intersection; (C) 95.2  $\mu$ m, at the other edge of the intersection; and (D) 190  $\mu$ m from the intersection, moving toward the grounded buffer reservoir.

The reaction used to demonstrate the microreactor concept also demonstrated the extent of mixing within a short physical distance (or time). One mM of o-phthaldialdehyde (OPA) and  $\beta$ -mercaptoethanol (BME) were used to fill the receiving channel, while the source channel was filled with 1 mM of glycine, and all three compounds were non-fluorescent. OPA will react with primary amine groups in the presence of BME to form fluorescent products. This reaction was monitored in a cuvette with a fluorometer at the same concentrations, and required approximately 1 sec to reach steady-state fluorescent intensity once the reagents were mixed. When this reaction occurred in a microchannel, the spatial fluorescence profile was determined by the inherent rate of the chemical reaction and the degree of physical mixing. Because the reaction could only start when the reactants met in the receiving channel, the intersection was the origin of the reaction, and the distance (x) in the receiving channel from the intersection was linearly proportional to the reaction time. The constant of proportionality was determined by the constant flow rate, which in turn was defined by the applied bias. When glycine was injected into the receiving channel under electric bias, the fluorescence increased as the injection plug flowed to the right side of the receiving channel. The flow rate (v) was linearly proportional to the applied bias, and the reaction time at position x was equal to  $x/v$ . The slope from a plot of fluorescence intensity vs.  $x/v$  was linearly proportional to the rate of this reaction. By fitting the lines of the fluorescence profiles before the plateaus, the ratio of the slopes for the applied biases of 100 V, 200V, and 300V were 3.4, 2.2, and 1.6, respectively. These ratios varied slightly from the inverse ratios of

voltages (6, 3, and 2), which may have been caused by the photobleaching of reaction products or uneven illumination. These results demonstrated the huge potential of nanofluidic gated microchannels as microreactors

### 3.20 Reactive Mixing

The ability to bring two reactive solutions together, mix them on short time scales, and then observe the products formed from the reaction is a critical enabling capability for future biofluidic devices. The hybrid three-dimensional nanofluidic/microfluidic architecture was shown to have significant advantages for these reactive mixing applications, and so the examination of reactive mixing continued. In this series of studies, the same transport device scheme previously reported was used. Two PDMS layers, with a single channel embedded in each, were sealed together with a 1 mm  $\times$  10 mm PCTE membrane between them. The channels were assembled at a 90° relative orientation. The source channel and reservoirs ( $S_1$  and  $S_2$ ) were filled with one solution, and the receiving channel and reservoir ( $R_1$  and  $R_2$ ) with the other solution or a plain buffer. The voltage scheme implemented had  $HV_1$  connected to both  $S_1$  and  $S_2$ ,  $HV_2$  was connected to  $R_1$ , and  $R_2$  was grounded. In the *off* mode, there was a constant flow from  $R_1$  toward  $R_2$  to replenish the solution in the receiving channel caused by  $HV_2$ . In the *on* mode, an additional flow caused by  $HV_1$  from  $S_1$  and  $S_2$  was transported through the membrane to mix into the active flow in the receiving channel toward  $R_2$ . A laser scanning confocal microscope (Leica SP2) was used to monitor the fluorescence images under the membrane inside the receiving channel.

A common amine derivatization agent, *o*-phthaldialdehyde (OPA), was used to demonstrate the micromixing and microreactor concept. OPA by itself is non-fluorescent, but it reacts with primary amine groups in the presence of  $\beta$ -mercaptoethanol to form fluorescent products. The source channel and reservoirs  $S_1$  and  $S_2$  were filled with 1 mM OPA and 2-mercaptoethanol (BME), and the receiving channel and reservoirs  $R_1$  and  $R_2$  with 2 mM glycine (Gly). The buffer was 50 mM borate at pH 10. Two experiments were performed, in which either the initial concentration ratio of OPA/Gly

was varied, or the initial concentration ratio was fixed but the total reaction time within the observing channel length was changed.

When  $HV_1$  was kept constant and  $HV_2$  was varied, changes were measured in the fluorescence spatial profiles along the reaction (receiving) channel under different mixing ratios. A typical fluorescence image is shown in Fig. 21. By taking the average of the intensity across the receiving channel cross-section for different axial positions, a fluorescence profile along the x-axis was obtained. Data in Fig. 22a show the effect of the  $R_V = HV_1/HV_2$  voltage ratio. Note that the zero position in the x-axis marks the intersection edge (nanoporous membrane). Two effects were immediately apparent. First, when  $HV_2$  was larger than 260 V, the reaction reached steady state within the observation region, and second, the larger  $HV_2$  and the faster the volume flow rate, the smaller the steady state concentration of fluorescent product. At smaller  $HV_2$  values the initial rate of reaction was larger, as expected. At the other extreme, when  $HV_2$  was too small, the slower rate of supply of Gly and the lower Gly concentration at the intersection caused a flat profile toward  $R_2$ , meaning the reaction was complete at the intersection. Furthermore, a significant increase of fluorescence was observed in the upstream ( $x < 0$ ) region, indicating significant backflow upon injection of the reactant plug.

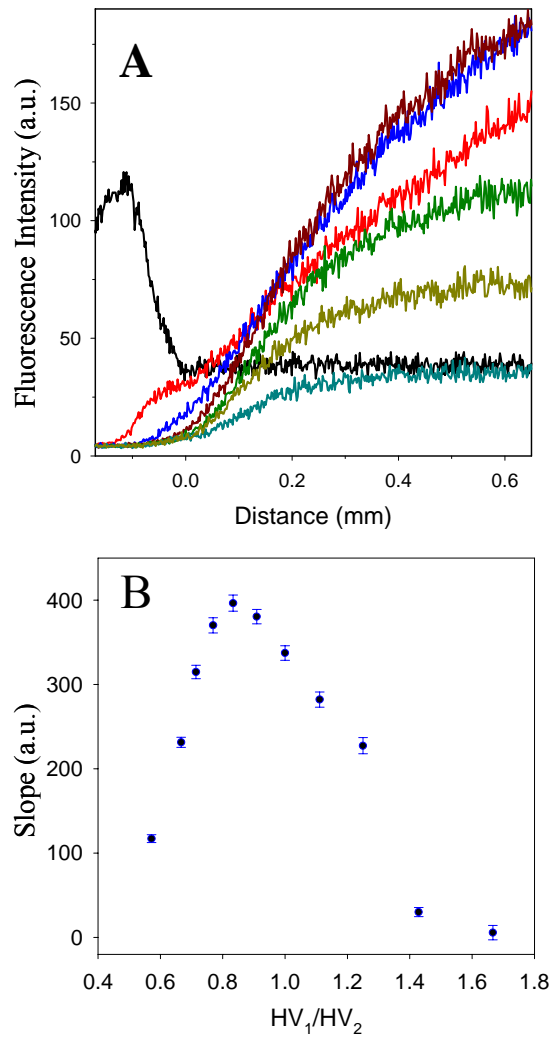


**Figure 22. Fluorescence profiles of reaction 1 along the receiving channel.**

(a)  $HV_1$  was 200, and  $HV_2$  was 120 (black), 160 (red), 200 (blue), 240 (dark red), 280 (green), 300 (dark yellow), and 350 (dark cyan) volts. (b) The initial slope of fluorescence versus distance ( $dI/dx$ ) as a function of applied voltage ratio  $R_V$ ,  $HV_1/HV_2$ .

Although the net flow rate in the receiving channel changed with the driving voltage, it was useful to visualize the change of fluorescence with distance  $x$  as a function of  $R_V$  to reveal the relative reaction rate under different mixing ratios. Fig. 21b shows the slopes of the spatial fluorescence profiles in the region  $0.02 \text{ mm} < x < 0.2 \text{ mm}$  from Fig. 21a as a function of  $R_V$ . The short  $x$  region was used to take only the initial reaction into account. Clearly the optimum reaction kinetics was achieved at an intermediate  $R_V$  value, which indicated a trade-off between deliveries of enough reagents to participate in

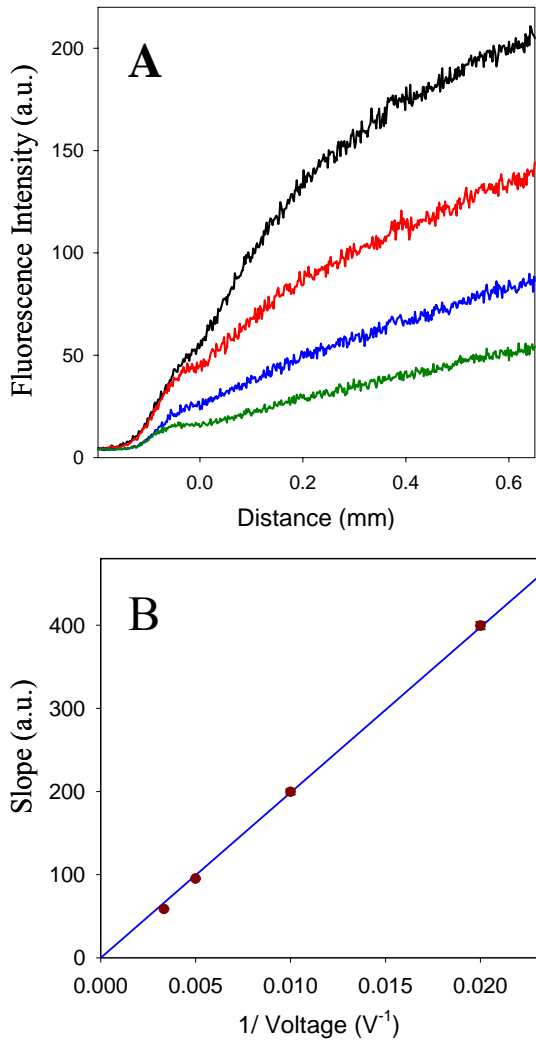


**Figure 23. Fluorescence profiles of reaction 1 along the receiving channel under different applied voltages.**

(a) The  $\text{HV}_1/\text{HV}_2$  for each curve are 50/40 (black), 100/80 (red), 200/160 (blue), and 300/240 (green). (n) The slope of fluorescence versus distance ( $dI/dx$ ) as a function of inverse  $\text{HV}_1$ .

the second order reaction and making  $\text{HV}_1$  so high that back flow effects were observed. Note that the mixing ratios obtained from varying the voltage ratio were expected to depend on the original reactant concentration ratio.

When  $R_V$  was fixed, the mixing ratio was fixed. The flow rate ( $v$ ) was linearly proportional to the applied bias, and was inversely proportional to the reaction time in the

same reaction length in the x-axis. Fig. 23a shows the fluorescence profiles for four different voltage combinations at  $R_V = 1.25$ . The higher the voltage was, the less the fluorescence increased. The fitting of the linear part of each fluorescent profile (keeping  $r^2 > 0.97$ ) resulted in a plot of the slopes as a function of  $1/HV_1$ , as presented in Fig. 23b. A linear relationship between the slope and  $1/HV_1$  was, as expected, observed. A reaction rate constant was extracted from these results. These results demonstrated that: (1) the hybrid microchannel/nanopore-membrane devices can serve as efficient micromixers and microreactors, and (2) microscopic kinetics can be obtained from single image measurements.

An immediate application which extended from the micromixing and microreactor concept was microsensing. Calcium ions ( $Ca^{2+}$ ) play important roles in many biological processes, such as neural transmissions, gene expressions, and muscle contractions. Numerous detection methods have been developed for  $Ca^{2+}$ . The common fluorescence probe Calcium Green was employed to detect  $Ca^{2+}$  with the hybrid microreactors developed here. In this study, the source channel and reservoirs  $S_1$  and  $S_2$  were filled with  $CaCl_2$  at various concentrations, and the receiving channel and reservoirs  $R_1$  and  $R_2$  with 2  $\mu M$  Calcium Green dextran (CGD) and 0.5 mM ethylene glycol-bis(2-aminoethyl ether)-N,N,N,N-tetraacetic acid (EGTA). The buffer was 10 mM 4-(2-hydroxyethyl) piperazine-1-ethanesulfonic acid (HEPES) at pH 8.6. In the on-state,  $Ca^{2+}$  was injected through the nanopores of the PCTE membrane into the receiving channel. CGD was already fluorescent, but the fluorescence increased drastically upon the binding with  $Ca^{2+}$  (Fig. 24a). A single-spot laser-induced fluorescence system was used to probe the change in fluorescence intensity upon  $Ca^{2+}$  injection across the membrane, and the change of fluorescence intensity was correlated to the concentration of  $Ca^{2+}$  (Fig. 24b). This calcium ion detection was a proof of concept in using molecular gates for microsensing. Many other sensor reactions can certainly be easily implemented, and the need of immobilization can be reduced because of the increase in sensitivity.

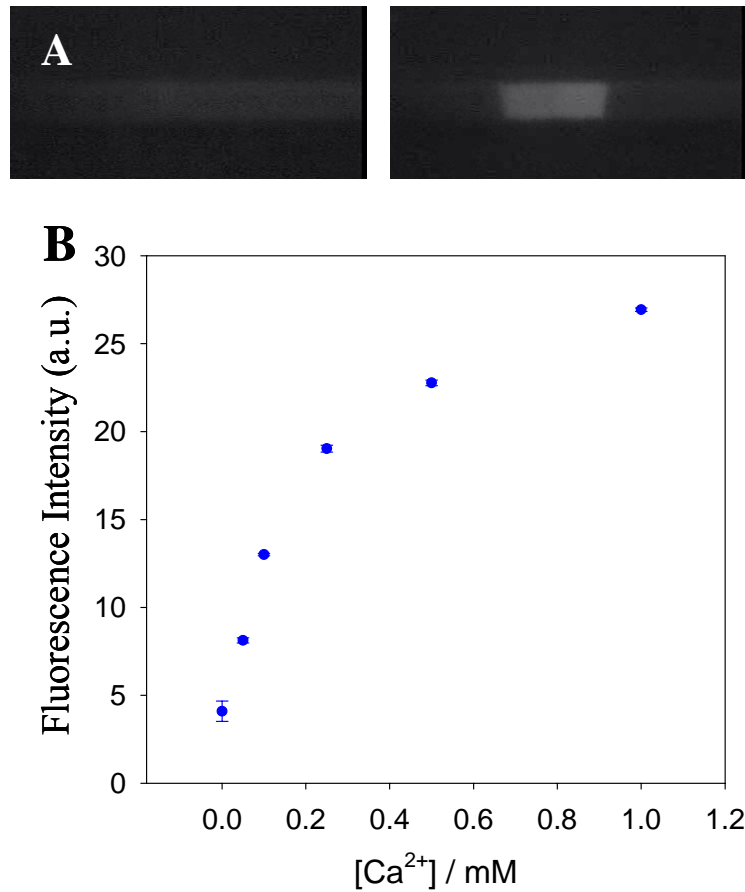


**Figure 24. Ca<sup>2+</sup> Detection.**

(a) Fluorescence images of Ca<sup>2+</sup> detection. *Left*, off state. *Right*, on state, Ca<sup>2+</sup> was injected into the horizontal CGD channel. (b) Fluorescence intensity as a function of Ca<sup>2+</sup> concentration. The source channel was filled with buffer containing various Ca<sup>2+</sup> concentrations, and the receiving channel with 2 μM CGD and 0.5 mM EGTA. The buffer was 10 mM HEPES pH 8.6. The fluorescence was measured at the intersection with single-spot laser-induced fluorescence (LIF). The applied voltage HV<sub>1</sub> was 100 V and HV<sub>2</sub> was 80 V.

The feasibility of applying this hybrid microfluidic-nanofluidic three-dimensional construct in micromixing, reaction and sensing was demonstrated. There was another special advantage worth mentioning. Because electroosmosis was the driving force for all fluidic motions at these experimental conditions, all mobile species inside the microchannel flowed into R<sub>2</sub>. When the system was switched to the off-state, it replenished the receiving channel with solution from R<sub>1</sub> reservoir, and the device was available for a new experiment without cleaning and refilling the whole system. The concepts developed and confirmed here added to the overall applicability in detecting chemical and biological systems in a variety of ways.

### 3.21 Membrane Chemistry

Further efforts focused on immobilizing the tag within the pores and demonstrating that it could be released electrochemically according to the proposed scheme for nanoaffinity separations. A thiol-labeled fluorescent analog (SAMSA) was used, since this allowed the correlation of the electrochemical and spectroscopic measurements of surface binding. Furthermore, considerable effort was made on another project that demonstrated that 20 nm Au colloids could be used as a scavenger for free thiol (SAMSA) in solution. It was a significant challenge to generate electrically continuous smooth Au films on the interior of the nanopores with varying internal diameter. These challenges were fully met, and electrically continuous Au coated nanopores of arbitrary diameter were generated.

The next step involved immobilizing the substrate on the interior of the nanopores. This was tested in both quiescent solutions and flow-through configurations to generate structures with Au-coated pores and Au on the external membrane surface on only one side. Such a structure was studied electrochemically, and the results are shown in Fig. 25. The broad ill-defined waves near the anodic end of the scan were integrated to yield coverage of the interior pores of  $1.2 \times 10^{-10}$  molecules/cm<sup>2</sup>.

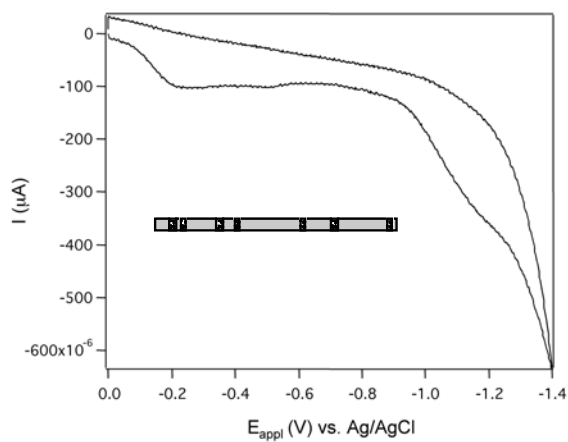


**Figure 25. Cyclic voltammogram of a Au-coated nanopore molecular gate membrane decorated with the S-terminated fluorophore SAMSA.**

The selective release of thiol-containing affinity tags immobilized within the interior of Au-coated nanopores was then focused on. Initially the membrane behavior was characterized with a thiol-labeled fluorescent analog (SAMSA). Later the fluorescently-tagged peptide was used as the affinity tag for the nanoaffinity portion of the final device.

### 3.22 Fluorescence/Electrochemical Desorption of SAMSA.

The electrochemical and fluorescent properties of the thiolated fluorescein analog, SAMSA, were studied extensively in Au-coated nanocapillary arrays as a model for the active peptide. Surface coverage of SAMSA on the interior of the gold-coated nanopores was determined by cyclic voltammetry to be  $1.9 \times 10^{14}$  molecules/cm<sup>2</sup>. For comparison, the coverage of SAMSA on planar evaporated gold films was found to be  $3.2 \times 10^{14}$  molecules/cm<sup>2</sup>. Given the fact that the nanopore was smaller and less accessible than the planar surface, the smaller surface coverage for the pore was not surprising.

After electrochemical reduction and release of SAMSA, it was detected by fluorescence. When the receiving solution was stirred, the SAMSA liberated from the Au film was rapidly homogenized, and the equilibrium concentrations were determined. As seen in Fig. 26, the fluorescence reached a maximum after 30 minutes of applied reducing

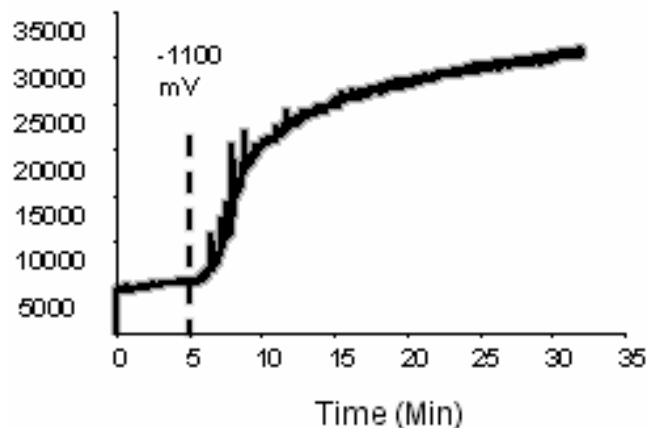


**Figure 26. Time dependence of the release of the fluorescent model SAMSA.**

potential, resulting in a maximum concentration of 11 nM in solution. The desorption kinetics of aromatic thiols is known to be much slower than alkanethiols of comparable molecular weight. After 30 minutes, photobleaching of the SAMSA became an issue. The expected concentration released from electrochemical data resulted in 26% of the released SAMSA being detected by fluorescence. In this experiment an electrochemical potential of  $-1100$  mV *vs.* Ag/AgCl was applied in the window  $5 \text{ min} \leq t \leq 35 \text{ min}$ . If, however, the same experiment was performed after acquiring a cyclic voltammogram, the population fraction recovered by fluorescence increased to 67%. The effect of the potential cycling prior to the stripping pulse was not well understood, although it was reproducible, and the beneficial effect was obtained under a variety of experimental conditions. Why the fluorescence was not in quantitative agreement with the surface population derived from charge integration was not completely understood. However, there were a number of mechanisms which could have been responsible for the smaller population by fluorescence, *e.g.* readsorption, spurious side reactions of the SAMSA, photobleaching, *etc.* The same general trends in the fluorescence measurements were observed when SAMSA was desorbed from Au-coated nanopores. In a typical experiment the fluorescence was observed to increase over time, and the desorbed SAMSA reached a maximum concentration of 69 nM in the receiving solution. When compared to the electrochemical experiment 21% of the electrochemical coverage was recovered by fluorescence. The recovery was increased to 58% when the potential was cycled prior to stripping, which was similar to the planar Au results. It was clear that applying a potential scan resulted in greater ultimate desorption of SAMSA from the substrate.

### 3.23 Fluorescence/Electrochemical Desorption of BoNT/A Affinity Tag

With the knowledge gained from the model compound SAMSA, experiments were begun on the BoNT/A affinity tag. This tag fit the general requirements for an affinity tag for the required nanoaffinity measurements, which were a thiol portion for attachment and subsequent release, a fluorophore for detection, and an amino acid sequence to specifically bind the A serotype of *C. botulinum* neurotoxin (KCRATKML). Surface

coverage of the affinity tag on planar gold was determined from cyclic voltammetry to be  $4.3 \times 10^{14}$  molecules/cm<sup>2</sup>. As seen with SAMSA, the coverage was slightly smaller in the interior of Au-coated nanopores,  $3.7 \times 10^{14}$  molecules/cm<sup>2</sup>. However, coverages of the affinity tag on both planar Au and within Au nanopores were higher than that determined by SAMSA.

### 3.24 Maintaining Salt Concentration Differentials

Previously the isolation and separation of two microfluidic environments were achieved utilizing a 15-nm pore diameter membrane. The capacity to provide fluidic isolation between microfluidic layers, while still allowing efficient on-demand analyte transport between layers, was advantageous for a number of microfluidic operations. For example, analytes in high salt environments, which are commonly found in biological systems, can be transferred to a lower conductivity fluid more suitable for efficient separations or detection techniques.

The 30-nm pore diameter interconnects were also found to have the ability to isolate phosphate buffer (low ionic strength, *I*) from phosphate buffered saline (large *I*), with over an order of magnitude difference in ionic strength. The ability to maintain this same salt isolation in the larger 30-nm pore diameter interconnects was significant, because the larger pore diameters allowed higher transport efficiency and larger molecular weight transport capabilities compared to the 15-nm pore diameter case.

The conductivities calculated from Ohm's law plots in either channel gave results for the individual channels similar to the values obtained in a device filled only with buffer. In addition to the obvious bias effect which arose from transport of species of differing molecular sizes, evidence was obtained for bias based on differing mobilities of ionic constituents of electrolyte solutions. Figure 27 shows a series of conductance measurements for the transport between two microchannels which were initially stocked with the same buffer solution. In the first set of transport events fluid was transferred from channel (12) to channel (34), as indicated by the increase in fluorescence in channel

(34) during the forward bias application. Afterward flow was established in the (34) channel, the current in channel (34),  $i_{34}$ , was measured. Initially  $i_{34}$  was diminished

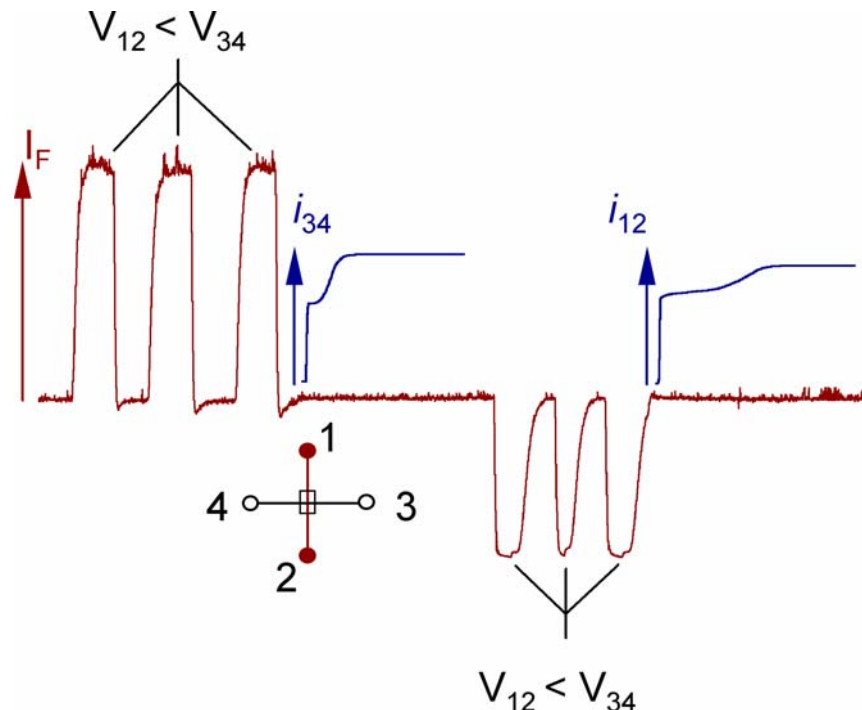


**Figure 27. Concurrent fluorescence and microchannel current measurements to assess biased mobility transport.**

Initially both channels (12) and (34) were filled with 10 mM phosphate buffer, while channel 1-2 also contained 1  $\mu$ M fluorescein. Throughout the experiment fluorescence was monitored in the (34) channel at the junction. In the first half of the experiment the nanocapillaries were biased for transport from (12) to (34) in three successive pulses, followed by a current measurement in the (34) channel. In the second half of the experiment the nanocapillaries were biased for transport from (34) to (12) in three successive pulses, followed by a current measurement in the (12) channel.

relative to its steady state value, which indicated the presence of a low conductivity region within the channel. As the low conductivity region was swept from the channel, the current returned to its steady state value. In the second half of the experiment an identical pulse sequence with opposite polarity was applied. Monitoring the current in the channel (12) elicited a similar response. In both cases the transferred solution was nominally the same composition as the solution on the receiving side of the membrane. And so, the question arose as to why the conductance decreased. The conductivity ( $\sigma$ ) can be expressed as the product of number density ( $\eta$ ) and mobility ( $\mu$ ) as shown in

$$\sigma = \sum (n_c \mu_c + n_a \mu_a) \quad (2)$$

equation 2, where the summation was carried out over all the cations ( $c$ ) and anions ( $a$ ) in solution. Because the initial solutions in microchannels (12) and (34) were the same composition, both solutions had the same conductivity. The observed reduction in conductivity from the bias pulse clearly resulted from the preferential transport of low conductivity species. In the present case the anions were  $\text{H}_2\text{PO}_4^-$  and  $\text{HPO}_4^{2-}$ , and the cations were  $\text{Na}^+$ . If the anions were preferentially transported, then a decrease in conductivity would be expected. Note that this was a biased transport effect in which size does not play a role, given that the hydrated radius of all ions was much smaller than the 30 nm channel width. This charge biased transport was not consequential in the context of simple molecular valving, as designated for the initial capillary electrophoresis layer in the BIP. However, this may be of consequence for advanced applications when samples are injected for separation or analysis from an analyte reservoir.

### 3.25 SAMSA Adsorption and Desorption Experiments

To elucidate the adsorption and desorption kinetics of thiols from the gold nanotubes, a model compound, SAMSA, was first employed. (SAMSA is similar to the botulism affinity tag in that both contain a thiol group for chemisorptive attachment to the gold and a fluorescein derivative for highly sensitive detection. The exact structure is presented in Figure 28).

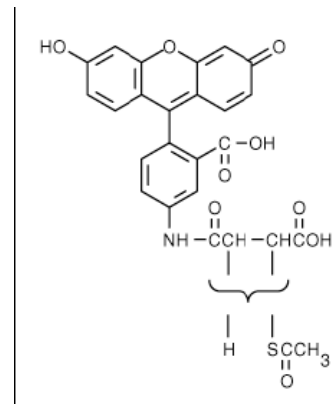


**Figure 28.** The exact structure of SAMSA.

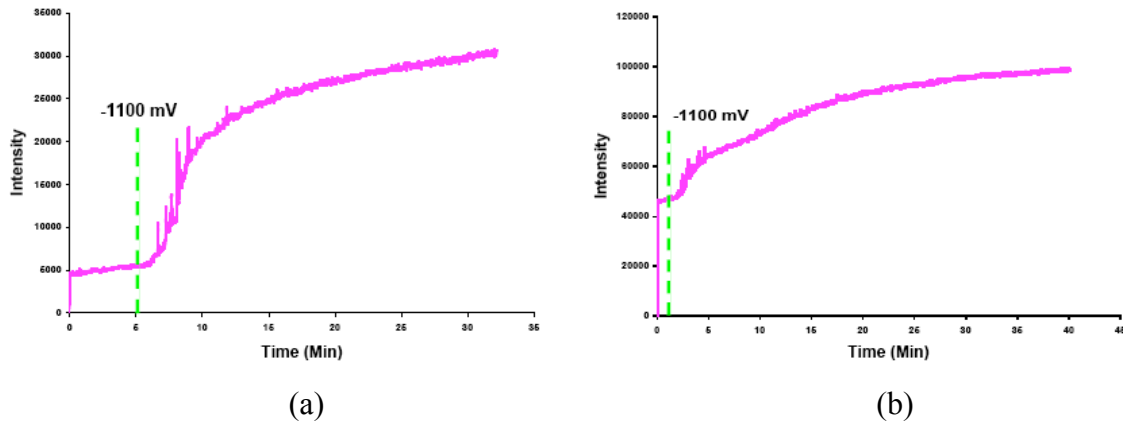


**Figure 29. Time dependence of the release of the fluorescent model SAMSA.**

Before (a)  $[\text{echem}]^* = 43 \text{ nM}$ ,  $[\text{fluor}]_{\text{max}} = 11 \text{ nM}$ , with 26% measured and after (b)  $[\text{echem}] = 67 \text{ nM}$ ,  $[\text{fluor}]_{\text{max}} = 45 \text{ nM}$ , with 67% measured, CV was performed on planar Au surfaces.

SAMSA self-assembled onto planar gold with a measured coverage of  $3.2 \times 10^{14} \text{ molecules/cm}^2$ , and onto gold nanotubes with a slightly lower coverage of  $1.9 \times 10^{14} \text{ molecules/cm}^2$ , as determined by cyclic voltammetry.

Since the ultimate goal of this work was fluorescence detection of SAMSA after its electrochemical release, experiments were performed to assess the concentration of SAMSA in solution by fluorescence after electrochemical release from a gold surface. A typical experiment is shown in Figure 29, where SAMSA was released from gold upon the application of a reducing potential of -1100 mV. The concentration of SAMSA from fluorescence was determined to be only 26%, as shown in Figure 29(a). This increased to 67% when a cyclic voltammogram (CV) was taken before electrolysis began (Figure 29(b)). Although this effect was not well understood, it was reproducible for the release of both planar gold and gold nanotubes.

Since only 60% of SAMSA at the high side was detected by fluorescence after the electrochemical release, the question was whether it was a fluorescence problem or an electrochemical problem. In other words, was SAMSA really not being released from the surface, or were other factors interfering with the ability to detect it all by fluorescence?

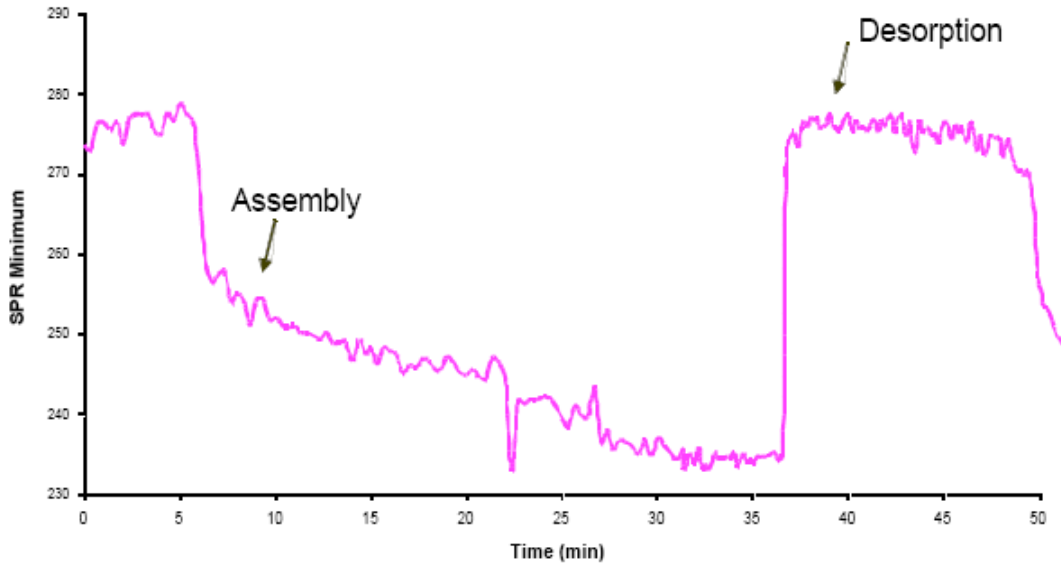


**Figure 30. Time dependent release of SAMSA from a planar gold surface measured by SPR.**

$\Delta\text{pixel}_{\text{assembly}} = -45$ , Thickness  $\approx 1.85$  nm,  $\Delta\text{pixel}_{\text{desorption}} = +42$ , 0.5 M KOH. Showed that 93% of the SAMSA was removed.

In an effort to address this question, surface plasmon resonance (SPR) spectroscopy was performed. SAMSA was assembled on a planar gold surface and electrochemically released, while the SPR shift was monitored at the surface of the gold. If all of the SAMSA was released, the SPR would have shifted back to its pre-assembly position. Figure 30 shows the SPR minimum shift as a function of time. The minimum decreased after the addition of SAMSA. When the electrochemical potential of -1100 mV was applied, the SPR minimum shifted back to the initial value, implying that all the SAMSA was removed from the surface. These results indicated that the problems were with the fluorescence measurements rather than with the release of SAMSA.

### 3.26 Affinity Tag Experiments

Utilizing the knowledge gained from experiments with SAMSA, similar experiments were preformed with the botulism affinity tag (SH-Lys-Fl-Cys-Arg-Ala-Thr-Lys-Met-

Leu). Cyclic voltammetry revealed coverage of  $4.5 \times 10^{14}$  molecules/cm<sup>2</sup> in gold

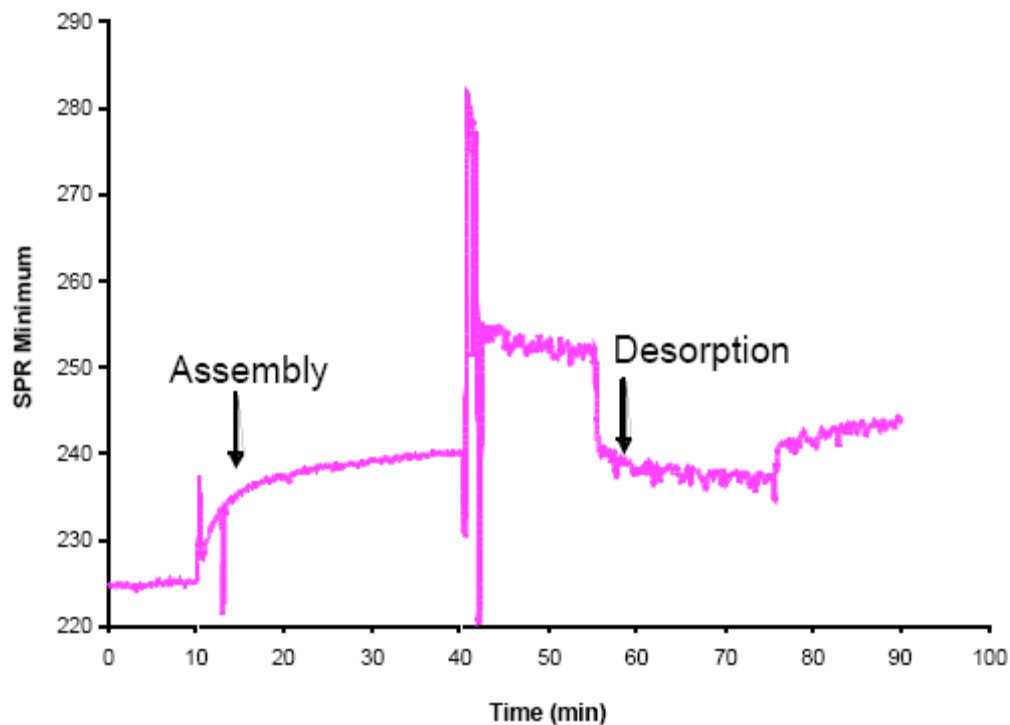


**Figure 31. SPR spectroscopy of the botulism affinity tag (SH-Lys-Fl-Cys-Arg-Ala-Thr-Lys-Met-Leu) in gold nanotubes.**

nanotubes. Fluorescence experiments were executed similar to those performed with SAMSA. The amount measured by fluorescence compared to electrochemistry was 17%, even less than with SAMSA. Once again, SPR spectroscopy was performed to determine if the affinity tag was actually being released by electrolysis.

Figure 31 shows the SPR shift as a function of time. Upon assembly, the SPR minimum increased, but did not return to pre-assembly conditions after desorption. According to this data, only 33% of the tag was actually released from the gold surface. The fact that only 17% was detected by fluorescence was most likely the result of both release and detection obstacles.

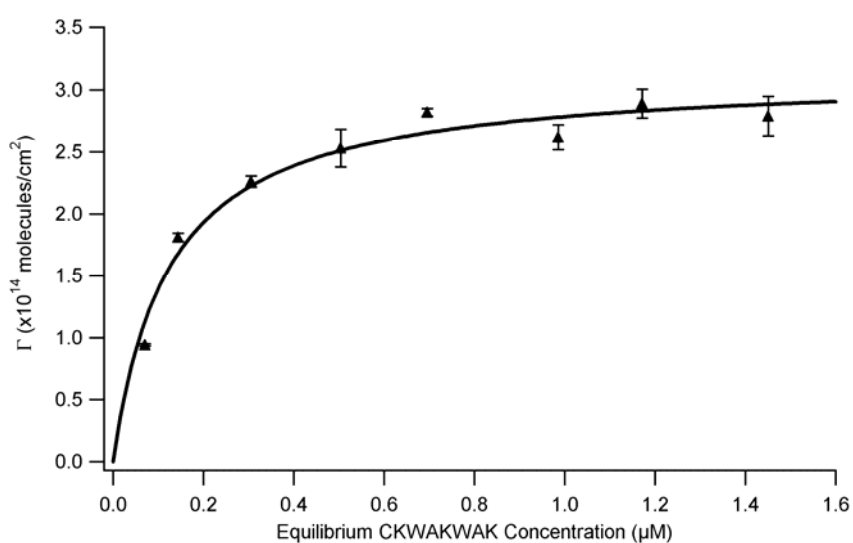


**Figure 32. Plot of the number density of surface adsorbed CKWAKWAK.**

23 nm Au colloid as a function of equilibrium solution concentration, determined by difference fluorimetry.

### 3.27 Post Processing of Collected Samples

To develop a method for the definitive confirmation of the target detection off-device, the use of colloidal gold as a mass-limited target carrier was tested. An octapeptide consisting of Cys-Lys-Trp-Ala-Lys-Trp-Ala-Trp (CKWAKWAK) was used as a model target for the capture, manipulation, and target identification on colloidal gold. The adsorption affinity of the peptide onto colloidal gold was determined, and the resulting conjugate was characterized to determine the proper modes of target manipulation.

The adsorption of CKWAKWAK onto colloidal Au was measured using difference measurements of fluorescence from the tryptophans. Figure 32 shows the isotherm for the adsorptions of CKWAKWAK onto colloidal Au at various equilibrium concentrations of CKWAKWAK. The surface coverage of CKWAKWAK reached a saturation coverage beyond the equilibrium concentration,  $[CKWAKWAK] = 0.5\mu M$ . Fitting the adsorption data to a Langmuir adsorption isotherm, shown in Fig. 32, yielded a maximum amount of adsorbed molecules ( $\Gamma_{max} = 3.1 \pm 0.1 \times 10^{14}$  molecules/cm<sup>2</sup>), and an equilibrium adsorption coefficient ( $K_L = 8.0 \pm 1.3 \times 10^6 M^{-1}$ ). Stringent precautions were

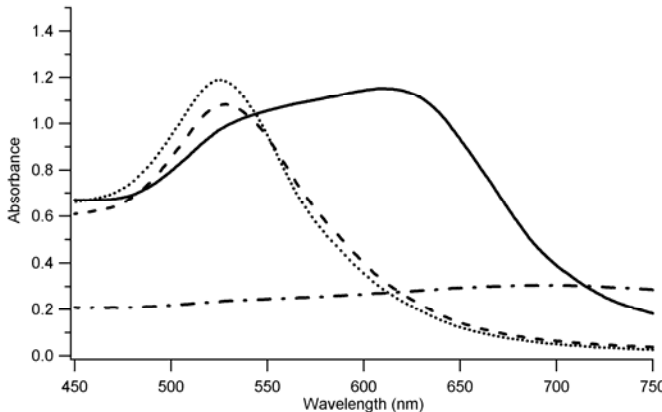


**Figure 33. UV-Visible absorption spectra of 2 nM CKWAKWAK/colloid conjugates under different conditions.**

(—) unbuffered (pH 5), (— - -) in 1 mM NaOH (pH 9), (...) in 1 mM HCl (pH 2), and (- - -) colloid conjugates from the pH 9 solution centrifuged, decanted, and then re-suspended in 1 mM HCl solution (pH 2).

taken to guard against multilayer formations, which would skew the saturation coverage to larger apparent values. Despite this, the saturation surface coverage ( $\Gamma_{\max}$ ) was somewhat larger than expected. The ultimate utility of the Au colloid-carrier strategy, however, depended on being able to capture macromolecular targets efficiently, and the isotherm data indicated that the Au-CKWAKWAK conjugates satisfied this criterion.

The absorption spectra of CKWAKWAK/colloid under various solution conditions illustrated the ease of manipulation of the conjugates, as shown in Figure 33. The unbuffered CKWAKWAK/colloid conjugate exhibited unresolved absorption maxima at *ca.* 530 nm and 620 nm, while the acidified conjugate displayed a single well-resolved absorption maximum at 525 nm. This suggested that in unbuffered solution the colloid was present in a state of intermediate flocculation, with a significant population still present as dispersed individual particles. The pH-controlled charge state of the adsorbate played a deciding role in determining the state of aggregation. The addition of base to the unbuffered conjugate solution removed the large spectral features, resulting in a spectrum with no discernible features, which is characteristic of a flocculated colloid. However, when this basic solution was centrifuged, decanted, and acid was added, the large absorption peak reappeared at 528 nm, which indicated dispersion of the colloid conjugate. A crucial feature of any strategy for manipulating mass-limited samples is the

ability to physically isolate the target compound and to transfer it quantitatively. Certainly the ability to bind, separate, and then re-suspend the Au-CKWAKWAK colloid conjugates satisfied this demand.

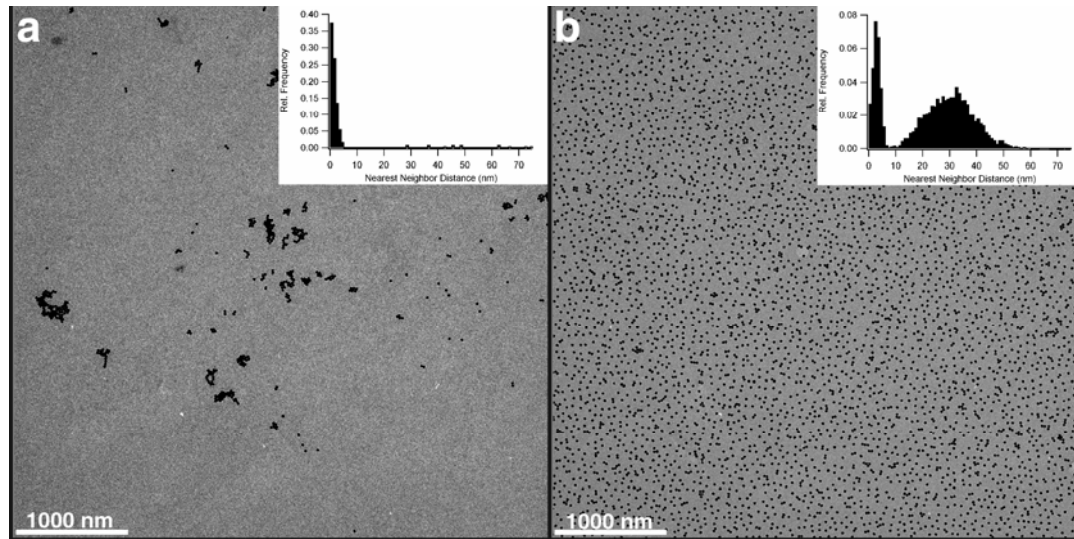


**Figure 34. Transmission electron micrographs and nearest neighbor distance histograms.**

(a) Unbuffered CKWAKWAK/colloid conjugates and (b) CKWAKWAK/colloid conjugates in 1 mM HCl.

The optical absorption spectra presented in Fig. 33 strongly suggested that the Au-CKWAKWAK colloid which conjugated in acidic media was dominated by well-separated single particles. To definitively address the aggregation state, electron micrographs of CKWAKWAK/colloid conjugates produced under various conditions were obtained, and are presented in Fig. 34. Also shown with each Transmission Electron Microscope (TEM) micrograph is the corresponding histogram of measured nearest neighbor distances between colloidal particles. Electron micrographs of dry colloid on the surface of a TEM grid were not completely accurate representations of the inter-colloid spacing in solution, since flocculation may have occurred as the solvent evaporated. However, the electron micrographs presented a lower limit on the solution inter-particle spacing, since flocculated colloid was not be expected to disperse upon

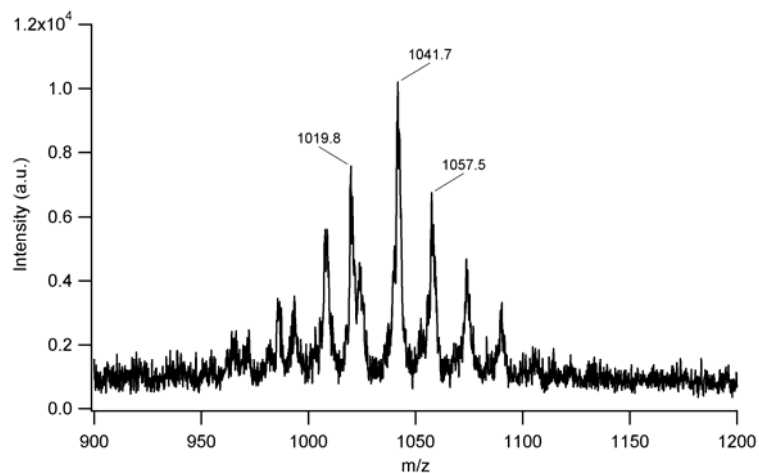
solvent evaporation. Thus, these TEM micrographs showed highly dispersed colloids on the surface of the TEM grid, and were interpreted to have resulted from highly dispersed colloids in solution.

Figure 34(a) shows the unbuffered CKWAKWAK/colloid conjugate. Single colloids, as well as clusters of colloids, are presented in the image. The presence of single colloids, in addition to small clusters of flocculated colloid, was consistent with the observation of two peaks in the UV-Visible absorption spectrum of this solution. The presence of single colloids explained the existence of the significant absorption at 530 nm, a feature characteristic of dispersed colloid, while the presence of flocculated colloid was likely responsible for the red-shifted absorption feature near 630 nm.

The micrograph in Figure 34(b) shows the CKWAKWAK/colloid conjugate deposited from acidic solution. Most of the colloids present in the micrograph were single colloids, with only a small fraction of the colloids present in clusters. The histogram of inter-particle distances shows that the majority of the population was present in the single particle band, with meant that the inter-particle spacing ( $\bar{d}$ ) was 32 nm. Because the settling of colloids onto the surface of the TEM grid was controlled by the same repulsive electrostatic forces that kept the conjugates dispersed when in solution, and because solvent evaporation was expected to increase the state of flocculation, these data confirmed that the colloid conjugated in acidic solution were well-separated. The straightforward interpretation of this was that at low pH the large fraction of protonated amines produced a large net positive charge on the nanoparticles, which resulted in a well-dispersed collection of particles.

After removal of the target/colloid conjugate from the microfluidic device, one possible identification method of the target was by matrix-assisted laser desorption/ionization mass spectrometry (MALDI-MS). A typical MALDI-MS of a CKWAKWAK/colloid conjugate is shown in Figure 35. The molecular weight of CKWAKWAK was 1018.5 Da. Thus the peak at mass to charge ratio ( $m/z$ ) of 1019.8 was assigned as  $(M+H)^+$ , and the peaks at 1041.7 and 1057.5  $m/z$  were 23 and 39 Da larger than the molecular weight,

those peaks were assigned to  $(M+Na)^+$  and  $(M+K)^+$ , respectively. Control experiments performed on MALDI samples prepared from colloid without CKWAKWAK, and with CKWAKWAK but without the colloid, showed no significant mass spectral peaks in this molecular ion region.



**Figure 35. Expanded molecular ion region of the MALDI mass spectrum of the CKWAKWAK/colloid conjugate.**

Prepared in 20 mg/mL 2,5-dihydroxybenzoic acid.

Definitive molecular ion information was obtained from the Au-CKWAKWAK conjugates by the simple expedient of mixing a buffered colloid solution with adsorbate under pH conditions designed to keep the colloidal particles charged, and thus well dispersed. Clearly, optimization of the physical isolation process was expected to enhance the yield of single nanoparticles and, thereby, improve the limit of detection of peptide, pushing peptide identification to the levels needed for mass-limited samples.

### 3.28 Development of a catalytic DNA-based $Pb^{2+}$ sensor

In collaboration with the Lu research group, a lead ion ( $Pb^{2+}$ ) sensor based on cleavage of a fluorescently labeled substrate strand was developed from double stranded deoxyribonucleic acid (DNA). In this scenario one strand of DNA, called the enzyme

strand, had a thiol tether for immobilization to gold substrates and a fluorophore for high sensitivity detection. The complementary strand, called the substrate strand, contained a quencher. When the DNA was hybridized, fluorescence was quenched. Interactions with  $\text{Pb}^{2+}$  caused cleavage of the double stranded DNA, which rendered the enzyme strand fluorescent. Upon electrochemical release from the gold, this fluorescence was measured to quantify the concentration of  $\text{Pb}^{2+}$ .

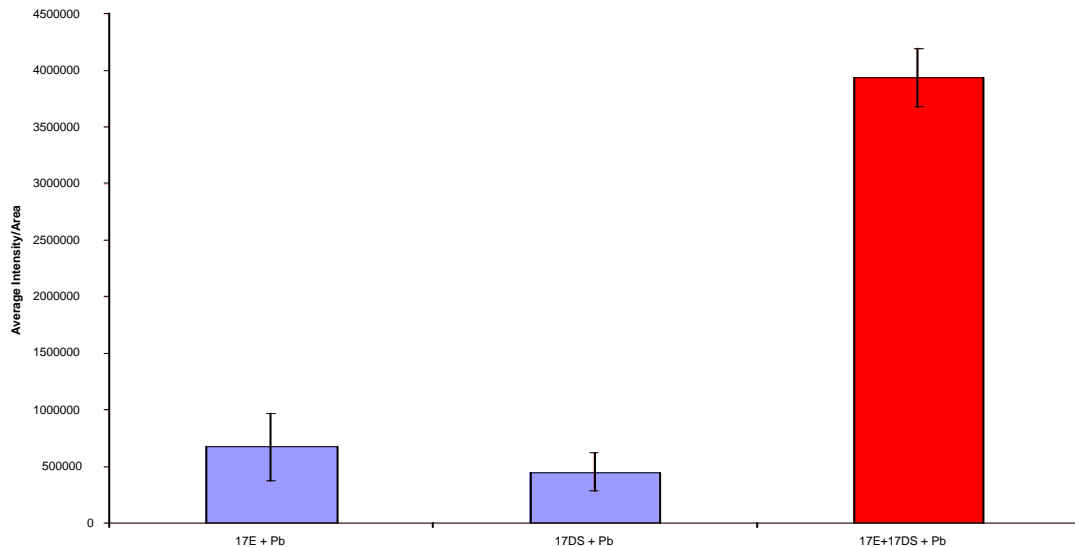


**Figure 36. Comparison of concentration of  $\text{Pb}^{2+}$  induced DNA released with controls.**

Experiments showed that the catalytic DNA could be successfully immobilized on a planar gold surface. Electrochemical reductive desorption of the thiol-terminated DNA resulted in a coverage of  $2.8 \times 10^{14} \text{ cm}^{-2}$ . Subsequent measurements of the fluorescent DNA after electrochemical desorption from the gold by fluorescence revealed that the DNA was difficult to completely remove from the gold surface. The activity of  $\text{Pb}^{2+}$  on the immobilized DNA was investigated by labeling the substrate strand with a fluorophore instead of a quencher, which enabled the direct measurement of the cleaved strand by fluorescence. In Figure 36 is shown a five-fold increase in fluorescence of the double stranded DNA over each of the two single strands when reacted with a  $10 \mu\text{M}$

solution of  $\text{Pb}^{2+}$ . Since the substrate strand did not contain a thiol group, this experiment revealed that the physisorption of the substrate strand was effectively negligible. The background fluorescence of the  $\text{Pb}^{2+}$  solution showed that the majority of the fluorescence observed with the two control experiments was due to the  $\text{Pb}^{2+}$  buffer solution itself. Though further experiments needed to be done, these preliminary results indicated that the DNA was catalytically active on a planar gold surface.

### 3.29 Proton Gradient Homostasis

Many bio-analytical techniques, such as Polymerase Chain Reaction (PCR) and protein analysis protocols, require multiple sample processing steps that must be carried out while conserving already mass limited samples. In addition, frequently each processing step must be carried out in different physiochemical environments, which poses a challenge for the integration of analytical unit operations into a complete analysis within a single micro analysis system. The possibility of sustaining unique chemical environments across spatially distinct microfluidic channels that are coupled via nanofluidic interconnects was investigated.

A key capability was the ability to establish and maintain chemical gradients within microfluidic devices across the nanofluidic array membrane. Novel interconnects provided fluidic communications between microfluidic channels such that mass transport between channels was possible, while maintaining the unique chemical environments in each channel. Figure 37 shows a series of confocal micrographs of the intersection region of two microfluidic channels that were coupled by a nanofluidic interconnect. The top channel was filled with a 5 mM phosphate buffer solution adjusted to a pH = 6. The bottom channel (horizontal) was filled with a series of phosphate buffered solutions in the range  $6.5 < \text{pH} < 8.0$ . Both channels contained equal concentrations of the pH indicator SNARF-1 (long-wavelength fluorescent pH indicator developed by Molecular Probes), with the interconnect region being imaged at the emission maximum of the protonated form of the probe (580 nm) and the isoemissive point (614 nm), simultaneously. As expected, the images recorded at 614 nm showed equal fluorescence intensities for both

channels. However, the images recorded at 580 nm exhibited a diminution in the fluorescence intensity for the bottom channel as the pH of the bottom channel was varied from pH 6.5 to 8.0. A decrease in fluorescence intensity at 580 nm was caused by the conversion of the fluorescent probe molecules to the deprotonated form at high pH, which gave direct evidence that the top and the bottom microfluidic channels were held at different pH's.

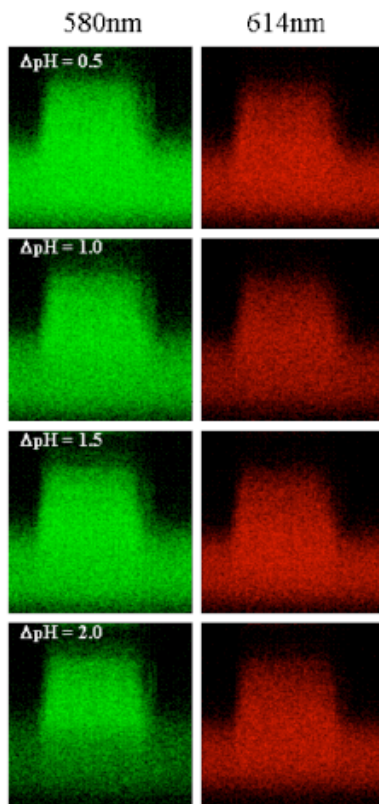


**Figure 37. Confocal optical xz microsections of the nanofluidic interconnect regions under conditions of varying pH.**

### 3.30 Dynamic Mixing Studies with Fast Scanning Confocal Microscopy

Reactive mixing within microfluidic devices was a critical enabling capability for the neurotoxin sensor development. Hybrid microfluidic-nanofluidic devices have shown great promise in the area of reactive mixing, a beneficial operation for various botulism neurotoxin detection schemes. The previous successes in reactive mixing have also

generated interesting fundamental questions that must be answered for the full utilization of the nanofluidic gate structures in sensing devices. Specifically of interest was the question of efficient mixing in the  $z$ -direction underneath the nanofluidic gate. The extension of the spatial profiling experiments to the dynamic injection schemes helped to understand the efficiency of the static mixer schemes. Confocal fluorescence studies with high temporal resolution ( $\sim 200$  ms) were used to detail the spatial and temporal profiles of reagent injection from one microchannel into another channel by biased

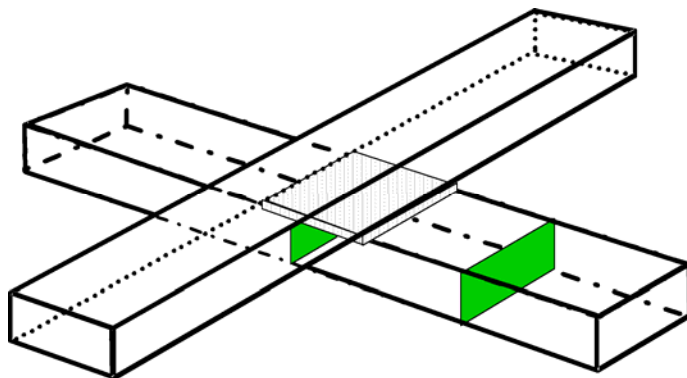


**Figure 38. Schematic of a multilayer device.**

Showing positions for confocal  $x$ - $z$ - $t$  series used for studying dynamic mixing (i.e. gated injections).

electrokinetic flow across a nanocapillary array membrane. A fast  $x$ - $z$  scanner to generate images of the receiving channel during the injection of a fluorophore was employed. Of particular interest was the development of a model of how the electric fields drive the transport of materials in the microfluidic channels when those fields are coupled to the electric fields in the nanofluidic capillaries.

As shown in the schematic in Fig. 38, fluorescence probing was limited to a line scan in the  $x$  direction at the  $y$  center point. Transport was probed in the  $z$ -direction both at  $5\text{ }\mu\text{m}$  and  $35\text{ }\mu\text{m}$  below the gate. This data was displayed either as an  $x$ - $t$  image or quantitatively on a graph using image processing software such as Image J. Line scans were taken every 1 msec, which provided better temporal resolution (64x) than earlier studies. Plots of the temporal characteristics of transport  $5\text{ }\mu\text{m}$  below the intersection as a function of gate biases showed that for a  $40\text{ V}$  bias, transport was never saturated, as

evidenced by the fact that the spatially integrated fluorescence intensity never achieved the levels observed at higher voltages. Steady state fluorescence did saturate for the 60 V case, but it took longer to achieve than in the 80 and 100 V cases. The time to achieve steady state did not dramatically increase between 80 V and 100 V. Figure 39 shows the  $x$ - $t$  transport profiles at 5  $\mu\text{m}$  and 35  $\mu\text{m}$  below the gate. It was important to obtain data regarding the  $z$ -component of transport, because this direction defined the limiting time for full mixing within the receiving microchannel. These data supported previous qualitative models, and provided highly temporally resolved data.

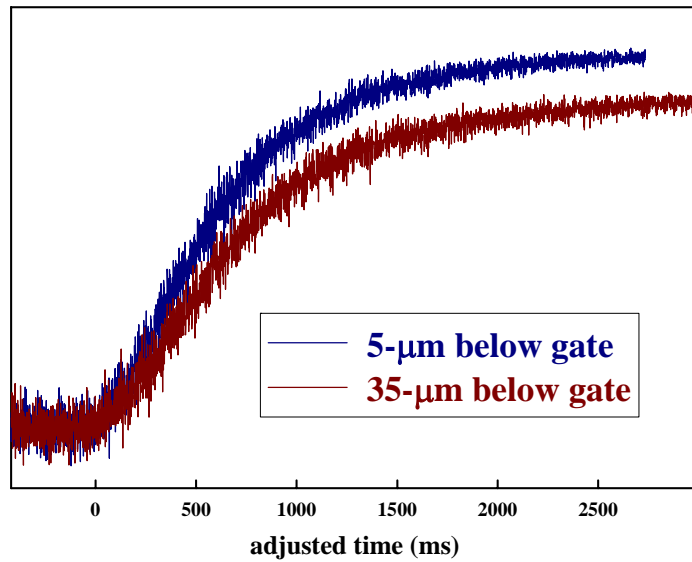


**Figure 39.** Fluorescence intensity as a function of adjusted time at 5- $\mu\text{m}$  and 35- $\mu\text{m}$  below the gate.

## 4. FABRICATION

The objective of this part of the effort was to fabricate a prototype Biofluidic Intelligent Processor (BIP). The first stage was to fabricate the basic microfluidic testbed for developing the key fabrication steps, and to test each type of nanofluidic element, as outlined below. The key fabrication steps were to integrate the membranes, compartments, electrical leads, and electrokinetic flow channels and cells together, via layer patterning and bonding.

The first goal was to fabricate electrokinetic flow microchannels and to integrate nanochannel membranes with the channels. To do so, the major goals to meet were: (i) patterning of channels in two glass substrates and connecting channels to create electrophoretic flow between the channels, and (ii) low-temperature bonding of polycarbonate membranes between the glass substrates. With a straightforward test bed, the effect of a wide variety of fabrication processes were investigated, and the performance of the nanochannel interconnects were tested.

### 4.1 Designed and fabricated masks for test bed prototypes

The test bed followed a simple schematic, as shown in Fig. 40, in which the electrolyte, sample, and/or a reference were introduced into different length separation channels, and

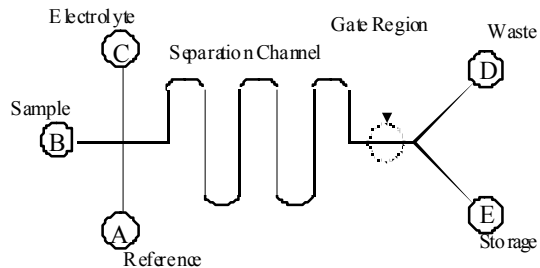


**Figure 40. Schematic of the initial test bed electrophoretic channels in the substrate.**

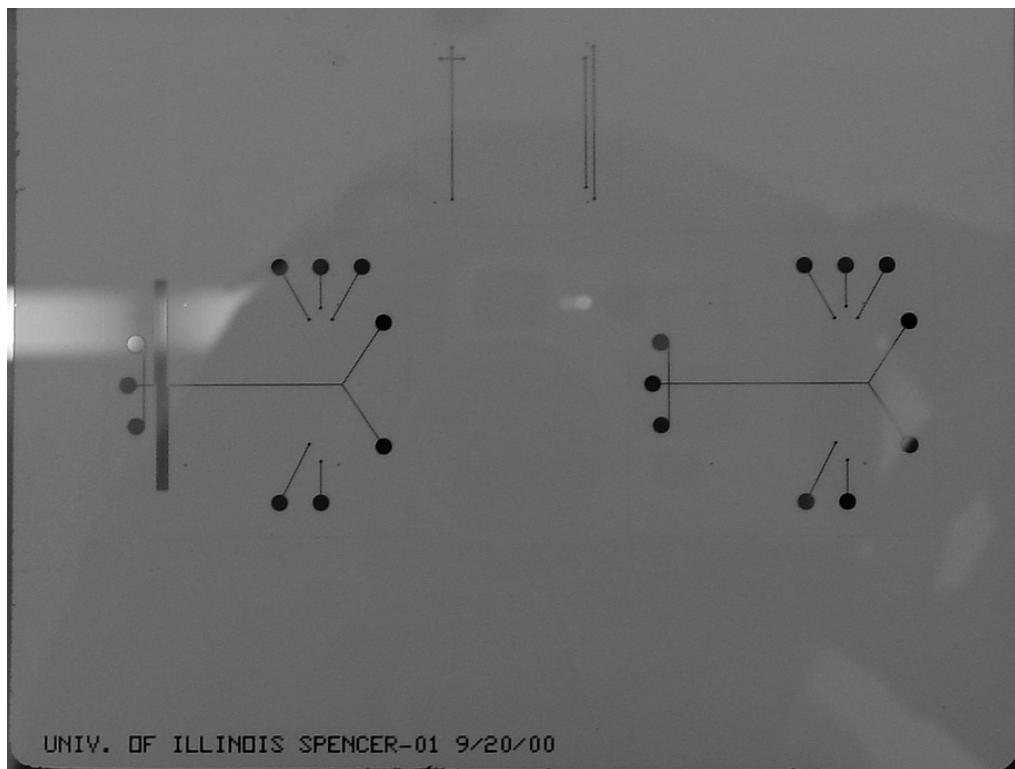


**Figure 41. Photograph of the masks designed to create the test bed.**

passed through the gate region, before being sent to either the waste or the storage ports. The gate region was a nanochannel membrane that was patterned via additional channels in the glass bottom and top layers between which the membrane was bonded. The mask design is shown in Fig. 41. The left side shows a 10 cm separation path achieved via serpentine channels with constricted channel bends (not visible). The right side shows the separation length of approximately 1 cm. In addition to the ports shown in Fig. 40, both the left and right sides show 5 additional ports, which allowed fluid to be routed through the nanochannel membranes via channels etched in the second glass layer in the bond. Although difficult to see, two different sets of these channels were shown in the top center of Fig. 41.

#### 4.2 Developed a method for patterning fluid channels

The processing steps were developed to etch electrophoretic microchannels in glass substrates. While straightforward, this part of the project was used to train the new personnel in the process, purchase the supplies, and set up the etch station in the clean room.

#### 4.3 Determine compatible membrane for nanochannel

This task was very important for the development of the BIP. Starting with commercially available nuclear-tracked polycarbonate (PC) membranes, an upper limit of about 140°C was set for any processing. The key process step that was limited by temperature was the bonding of the membrane between the glass layers in the test bed. Commercially available adhesives were focused on that could be applied via standard microfabrication methods. Initially a fully suitable membrane was not identified which could be used with the existing process capabilities (see next section).

#### 4.4 Develop membrane transfer process to substrate

This task requires the adhesive to be selected, as discussed above. The membrane was placed on different carrier plates, which were used to process the membranes, and then aligned and bonded to the substrate, once the adhesive process was developed.

#### 4.5 Etching of silicon

Anisotropic etching of silicon (Si) was necessary for the eventual incorporation of through-holes, routing channels, and glass frit in the BIP. The double-sided alignment, etching and passivation process was developed to achieve 50  $\mu\text{m}$  through-holes, to etch channels and to shape the wafer. In Fig. 42 is presented photographs of channels and through-holes etched into Si Wafers.

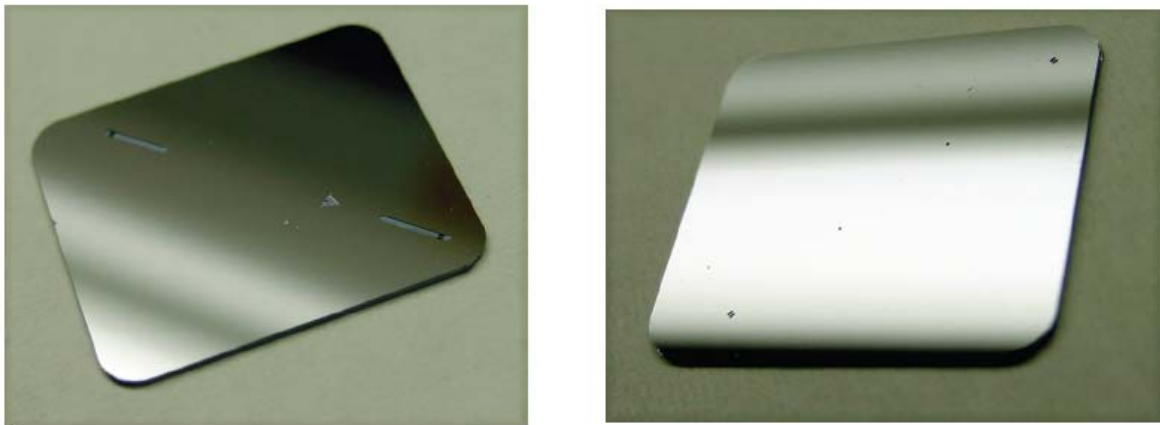


**Figure 42. Photographs of channels (left) and through-holes (right) etched into Si wafers.**

#### 4.6 Start-up Challenges

The first difficulty encountered was to size the channel structures for the electrophoretic flow, such that sufficient pre-separation was achieved, without significantly shearing of the bands. Constricted channel bends were used, which were 1/3 to 1/2 the width of the main electrophoretic channel width. Since the test bed was relatively large, the mask needed to be multiply stepped. Cumulative misregistration caused misalignment at the channel bends, which created undesirable constrictions. When the misregistration problem was corrected, the problem was solved.

Along similar lines, hydrofluoric acid (HF) was used to etch the glass channels in the testbed. Initial attempts used chromium (Cr) as the mask. Buffered Oxide Etch (BOE) plus concentrated HF resulted in the excessive pitting and the uneven etching of the glass (Figure 43). The next iteration used a commercially available glass etchant, and a 100 nm Au layer was added as an etch stop. This solved that problem.

An expected challenge was finding the optimum adhesive for bonding polycarbonate membranes to the substrates. Spinning or spraying the adhesive on the wafers resulted

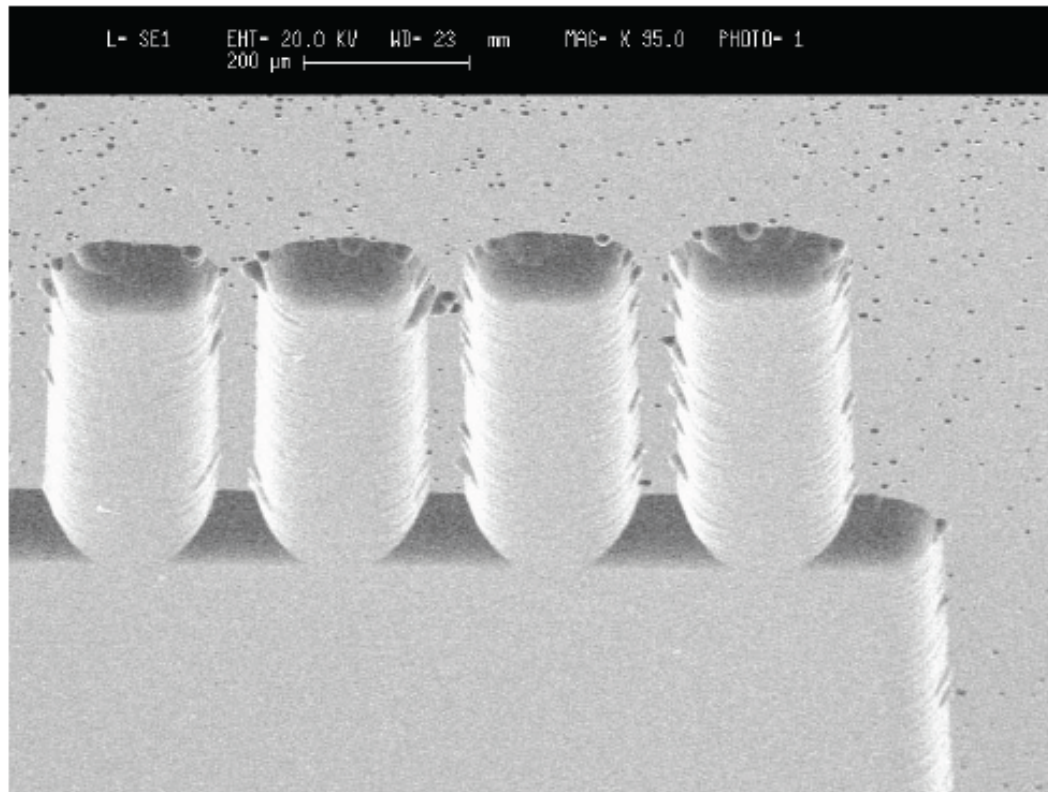


**Figure 43. SEM micrograph of glass etching which showed excessive pitting.**

in thin, uniform coatings that were a few microns thick. Several different commercially available adhesives were tested.

The main result in the early phases of fabrication was the development of a process to pattern etched microchannels in glass substrates. Etch channels in glass were achieved with a minimum width of about 10  $\mu\text{m}$  that were greater than 5  $\mu\text{m}$  in depth. Since the smallest dimensions were far larger than this for the initial test bed, this step was completed.

A process to etch through Si wafers using the PlasmaTherm ICP-DRIE system was also developed. A minimum through-hole of 50  $\mu\text{m}$  in diameter that also simultaneously etched far larger structures of up to  $\text{mm}^2$  areas was achieved. This accomplished the etching of small access ports through Si wafers, while at the same time was used to etch through large cavities for the reservoirs.

#### 4.7 Second stage of fabrication of a first plus generation of BIP

Three tasks were then focused on: (1) using phenolic adhesive bonding of the polycarbonate nanopore membrane to etch glass, (2) development of high-aspect ratio frit structures in silicon for filtering influent, and (3) the development of a specialized e-beam evaporator used for fabricating the membrane and glass structures, as originally detailed in the proposal.

#### 4.8 Phenolic adhesive bonding

A key work for fabricating the BIP was to optimize the phenolic bonding process and to improve the bonding to glass. A chrome evaporation and patterning process was developed to prevent the blockage of the nanopores in the membrane when using the phenolic adhesive. The scheme employed was to deposit chrome via a shadow mask on the region of the membrane that was to form the nanogate. After plasma treating the membrane with oxygen and forming gas plasma, the phenolic adhesive was spun on, dried, and patterned to re-expose the chrome layer. The chrome was subsequently removed with an etchant. The membrane was then transferred to the substrate employing the transfer process discussed previously, and thermally bonded when the thermosetting phenolic as the resin cured.

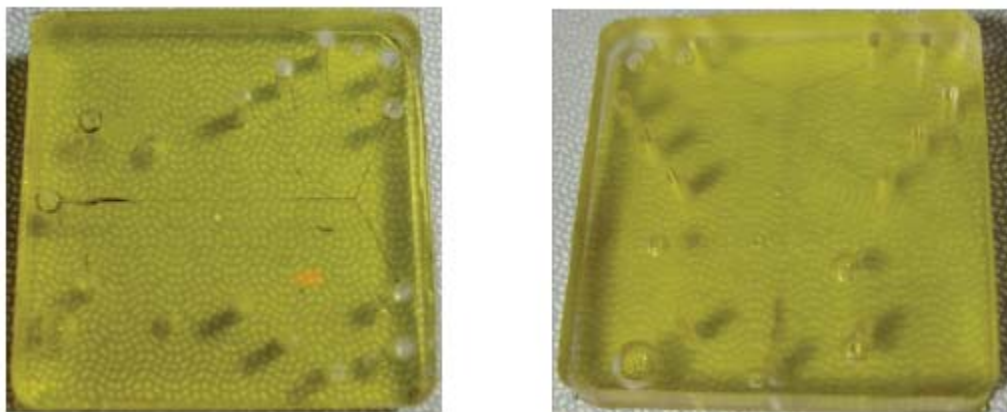


**Figure 44. A nanogate membrane bonded to glass with phenolic.**

Top (left) and bottom (right) views of PDMS interconnects and access ports to transfer fluid dye from a microchannel through a gate to the top across channels.

Figure 44 shows the next step pursued in the BIP development, with a nanopore membrane bonded to etched glass, and patterned PDMS bonded to the membrane. The PDMS on top contained the ports needed to access and test each of the cross channels.

The strength of the bonding made with phenolic adhesive weakened when the membrane was soaked in various basic and acidic aqueous solutions that might be encountered in fabrication of the BIP. The strength of the bonding was increased by employing two different types of chemical treatments to the glass and membrane.

Work also continued with developing the adhesives for bonding the membranes to glass and to other membranes. The main issue impeding this method was controlling the kinetics of bromide (Br) addition to the deprotonated alpha site on the polyvinylpyrrolidone (PVP) molecule that was on the surface of the hydrophobic polycarbonate membrane. The kinetics for this reaction was very slow, and thus only relatively weak bonds were achieved. Since the phenolic resin adhesive provided a satisfactory solution, work on the linkers was discontinued.

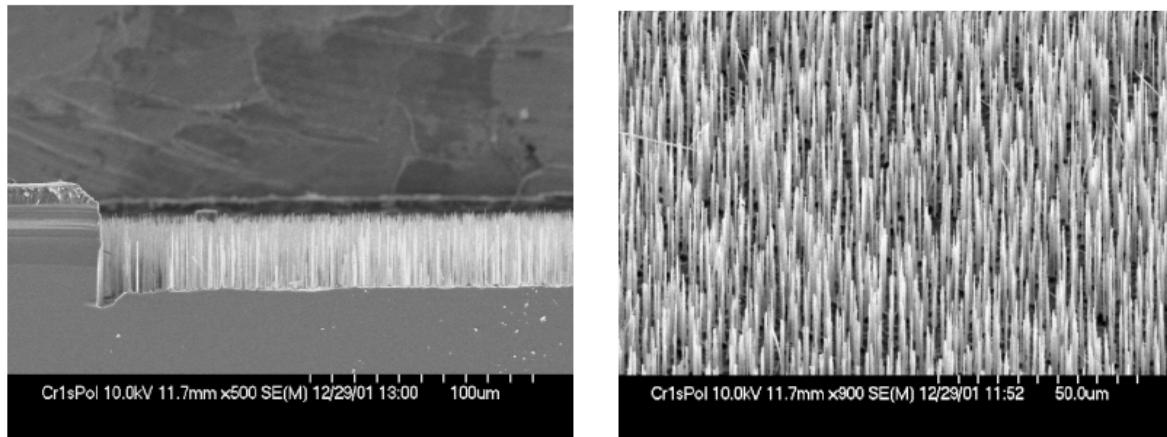


**Figure 45. Development of micro-'grass' structures for making low-pressure loss glass frits for ultra-high area filtering of influent.**

(left) Shows the side view of frit structure etched into Si wafer, and (right) shows the top view of high-aspect ratio, low flow resistance frits.

#### 4.9 Development of high-aspect ratio frit structures

The second main task in this period was to develop a process for creating glass frit structures in Si to create low-flow, low-pressure drop filters. Figure 45 shows very high aspect ratio needle-like structures etched into Si using a new inductively coupled plasma-dry reactive ion etch (ICP-DRIE) process that was developed. The goal was to produce a randomized bed of Si “grass” with monodisperse micron-sized diameters, with spacing of a couple of microns. The hydrophobic Si surface could then be subsequently oxidized to create a hydrophylic surface. Cohesive particles larger than the spacing could be trapped within the micrograss, thereby filtering the medium. Work continued on techniques to set the size of the grass diameters and the density of the spacing, to create graded filters. This work was expected to optimize the fabrication, and to test the effectiveness of the filtering.

To use both the sputterer and the evaporator in the same operation, the evaporator was connected to a cluster tool assembly, as shown in Figure 46. The 4-pocket e-beam evaporator is shown in Figure 47.



**Figure 46. Cluster tool evaporator and sputterer (left).**

Used to fabricate the bases and membranes.

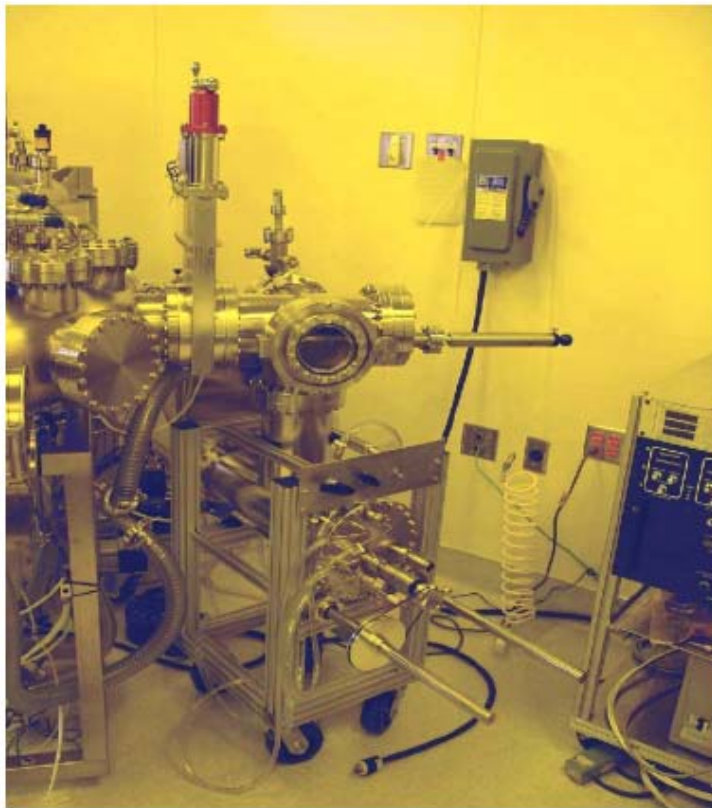


**Figure 47. Evaporator system developed for fabricating the membranes.**

#### 4.10 BIP Multilevel Fabrication

The next generation of BIP was to be a multilevel interconnect device. The first generation BIP's reported had three layers, a bottom and a top cap with a nanopore molecular membrane in between. To begin the multilevel fabrication work, new mask sets and dies were developed. A new bonding method was developed to replace the commercial glues previously reported that would permit multiple membrane layers, and a method of molecule manipulation was required.

To advance the BIP into multiple level interconnects from the first generation two-level devices just reported, mask sets (Figure 48) and dies were designed and fabricated that permitted the flow and control across the full 7 layers. The seven layers were comprised of: (1) the bottom layer in which the main electrophoresis channel resided, (2) the first

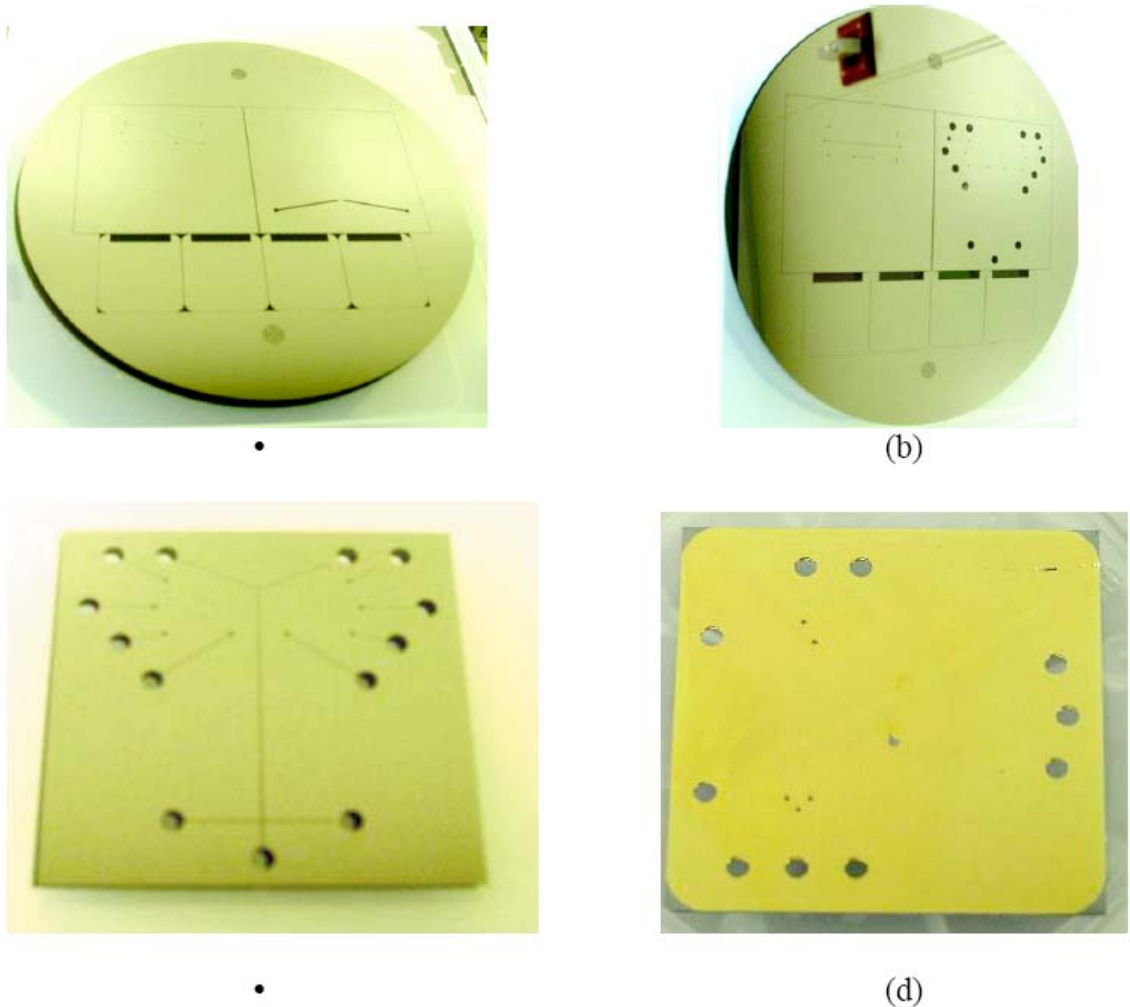


**Figure 48. Mask sets to etch 6 of the 7 layers in the BIP.**

nanopore membrane for molecular separation, (3) the first interchannel, (4) the second nanopore membrane, (5) the second interchannel membrane, (6) the third nanopore membrane, and (7) the top optical access cap.

The overall scheme of routing fluid through all the layers changed only slightly. The main differences were that glass was used for both the bottom and top layers, to allow the optical characterization of the fluid flow and separations for testing, and the fluid interconnects to the laboratory test equipment were made through the top layer via port holes. Over six sets of masks were made, which included shadow masks to RIE through

the polycarbonate layers to open up the fluid ports between the layers, and/or to open the cross channels of the interconnects. The main issues to be resolved were (i) developing the correct 3-D geometry to allow all the tests desired to be conducted, and (ii) to develop a method to open the etch holes through the top optical access layer.

The top optical access layer was fabricated differently from the other layers, in that through-holes were also etched to open the access ports. Because of well-known difficulties in etching through glass wafers with hydrofluoric acid, ultrasonic milling was used. To maintain an accurate spacing between the 13 through-ports, a tool steel mill head for the ultrasonic mill was designed and fabricated that simultaneously milled through all of the holes at once. Due to the high surface finish required for bonding (as discussed below), a method to protect the bottom surface during the abrasive cutting of the glass was developed.

#### 4.11 A new method of transferring and bonding multiple layers

The basic method employed was a transfer process. The main process steps were:

- (1) Mount the as-received polycarbonate membrane on the carrier, without wrinkling or deforming it in any way. Recall the membrane was approximately 4 microns thick, so this first step was not trivial.
- (2) Adhere the membrane on the carrier sufficiently to hold it in place for subsequent handling, but not so tightly as to permanently bond it to the carrier.
- (3) Apply an adhesive layer over the membrane, such that smooth coverage occurred, without the adhesive seeping through the nanopores, clogging the holes and/or permanently bonding the membrane to the carrier plate.
- (4) Align the membrane and carrier to etched glass substrate and tack in place.
- (5) Thermally cure to activate the adhesive, without degrading the polycarbonate.
- (6) Release the carrier from the membrane to leave a free standing membrane.

The main issue with multiple layer bonding was to achieve the bonding of the polycarbonate layers to the glass, and then to each other, without clogging the nanopore channels. The commercial adhesive used to adhere one polycarbonate layer to the glass substrate would not bond the polycarbonate to the polycarbonate layers. In addition, subsequent spins on top of the nanoporous membrane clogged the pores. To resolve both these issues, a new adhesive was developed for the polycarbonate to glass adhesion and for the polycarbonate to polycarbonate adhesion.

One of the keys to achieving the desired bond, without clogging the nanopores, was to use self-assembled monolayer linkers, with reactive end groups to adhere to glass and to the polycarbonate. For the glass/polycarbonate combination, the heterobifunctional linker 11-bromoundecyldimethylchlorosilane was used. The chlorodimethylsilane moiety provided linkage to glass, while the bromoalkyl portion of the molecule attacked the pyrrolidone side chain of the Polyvinylpyrrolidone (PVP) surface coating of the polycarbonate track-etch (PCTE) membranes. The polycarbonate/polycarbonate combination used a homobifunctional linker, 1,3-dibromopropane. For both adhesives, the linkers were diluted to a very low concentration, and the surface to be bonded was either dipped in the solution or the solution was spun on. After the solvent was evaporated, a very thin layer (ideally a monolayer) remained, with the desired reactive group exposed on the surface to be bonded with the nanopore membrane. The bonding was then created by applying pressure and heat.

Two major issues arose in achieving the repeatability of the assembly process: (1) the surface to surface conformation of the surfaces, and (2) the process order for the preparation of the linkers. Issue (1) dealt with the local and global surface roughness and inhomogeneities between the polycarbonate membranes and the glass substrates. The glass substrates had a local surface roughness of 100 to 1000 Angstroms ( $\text{\AA}$ ), which depended on how the substrates were fabricated by the suppliers. The glass substrates also had between 0.01 to 5  $\mu\text{m}$  curvatures per mm, which depended on the manufacturer's polishing. The membranes had different local roughness, depending on the side; the "smooth" side had a roughness of about 100 to 200  $\text{\AA}$ , and the "rough" side between 400

to 1000 Å. The membranes conformed globally to the substrate. The main problem with roughness was that when bonding with self-assembled monolayer linkers, whose lengths were on the order of 10-30 Å, the two surfaces had to come into direct contact for bonding to occur. If the local roughness and global positioning were much greater than this, bonding occurred only on the asperities. Previously, to overcome this problem, significant pressure (0.1 – 1 kbar) was applied to force the surfaces into contact. While successful, this pressure caused problems with the cracking of the glass and the plastic flow of the membranes. These new bonding methods reduced the need for applied pressure, particularly when the second glass slide was applied to create an optical cap.

The methods to reduce applied pressure included: (a) using a planarization layer to fill both the local and global roughness, and (b) changing the linker processing to effect more complete bonding. A spin-on phenolic resin process was developed for the planarization. The planarized layer conformed and adhered strongly to glass, as well as to one of the types of polycarbonate membranes. The layer, when cured, reflowed and then set up, so that the interface between the glass and membrane was completely filled and smooth. The layer was approximately 0.25 microns thick, which was sufficient to fill the voids without adding inhomogeneities. It could also be patterned, so that it did not plug the active areas of the membrane. This planarized layer was used on the outer glass layer, which allowed bonding of the full stack without the application of undue pressures.

Along with the planarization layer development, the linker chemistry processing was also changed. This change was desirable to control the stack bonding order and to reduce the bonding pressure. For instance, it was advantageous to first adhere the linker to the polycarbonate layer before it was bonded to the glass substrate, so that the entire PC surface had the linker bonded, rather than only the asperities that occurs when first adhering to the glass surface. This work required the development of non-aqueous linker chemistry.

#### 4.12 BIP Fabrication

The fabrication of the BIP continued to focus on bonding issues for making multilevel interconnects for the next generation of BIP device. Three parallel paths to fabricating devices were explored: (1) improved PDMS/membrane/glass structures for the transport and integraton to continue conducting experiments, (2) aqueous phenolic resin adhesives for bonding glass to membrane and membrane to membrane, and (3) self-assembled monolayers (SAM) for direct glass to membrane and membrane to membrane bonding.



**Figure 49. PDMS bonded membrane on etched glass slide.**

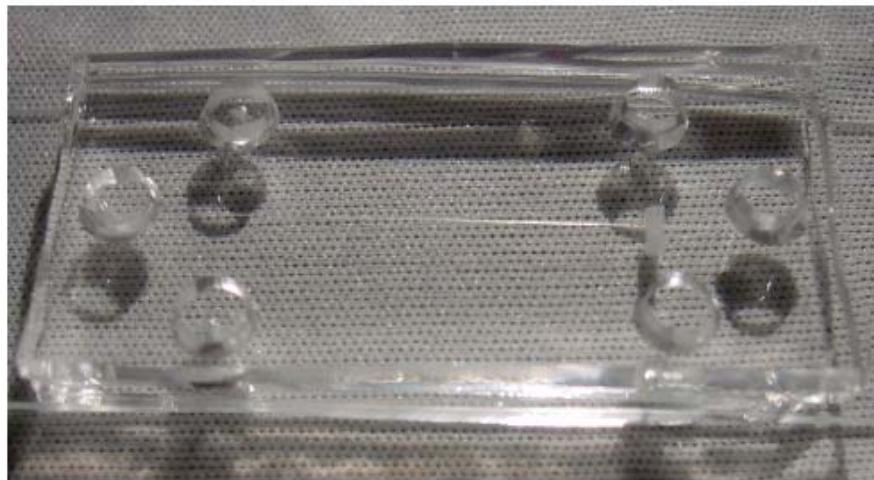


**Figure 50. PDMS channels integrated with a membrane.**

The key work was to optimize the phenolic bonding process and to develop new chemistries for the SAM work. Figures 49 and 50 show PDMS on glass and membrane BIP's fabricated for testing of the gates, and for testing processing parameters on the membranes for improved first generation BIP's. In Fig. 49, the microchannels were etched in glass, and in Fig. 50, the microchannels were developed in PDMS.

A key issue being resolved by the phenolic adhesive effort was the bonding of non-planar 100 to 400 nm surfaces (conceptually shown in Fig. 51) with sub-micron bond thickness



**Figure 51. Concept of phenolic conforming to a "rough" membrane topography and planarizing for  $m$  multiple stacked layers.**

“dry” adhesives. Sub-micron adhesive planarizing agents are an active field of research, and the development of an aqueous phenolic adhesive that will thermally set and planarize, without plugging the pores of a PVP-free polycarbonate nuclear track-etched membrane, is significant. The PVP-free PC membranes were hydrophobic. Thus, the plasma treated membrane in forming gas ( $N_2/H_2$ ) plasma, followed by an oxygen ( $O_2$ ) plasma to control the wetting angle such that the aqueous phenolic resin would spin-on the membrane, did not wick into the nanopores by capillary action. Figure 52 shows such a membrane bonded to glass with this new process.



**Figure 52. A hydrophobic PC membrane bonded to glass with an aqueous-based thermosetting phenolic adhesive.**

Progress was also made on the bonding the membranes without plugging the pores. The goal was to bond membranes to silica using molecular bonding linkers that were approximately 2 nm long, such that the pores were not plugged. A three-part process was developed, where the PC membrane was coated with PVP. Relatively weak bondings

were achieved at atmospheric pressures and room temperature due to small bond areas at the asperities.

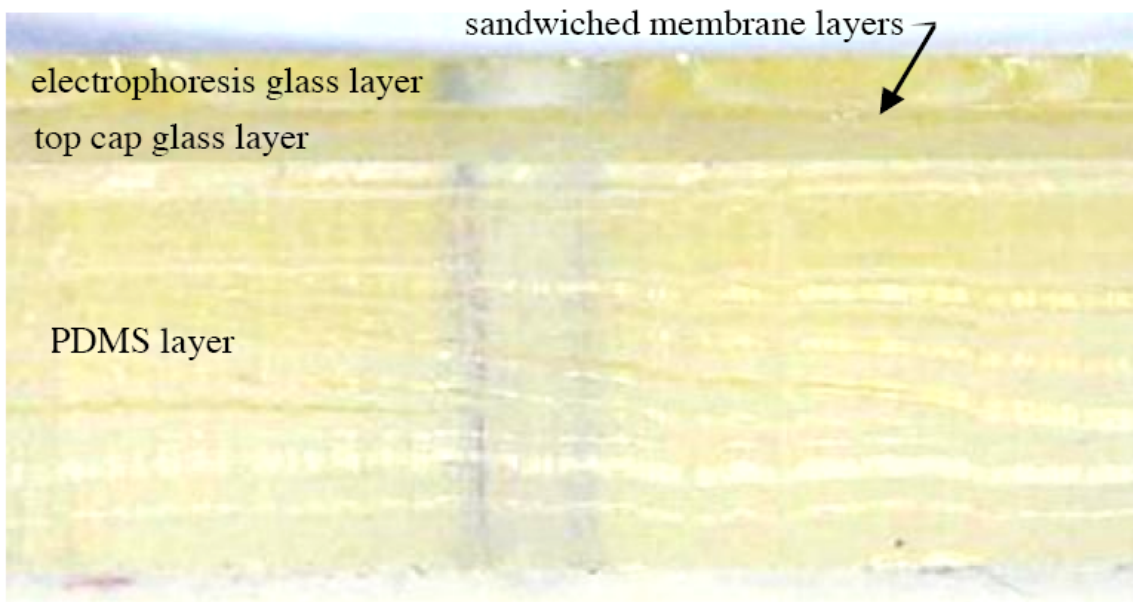


**Figure 53. An enlarged side view of a five-layer second generation BIP.**

Between the two glass layers were two nanopore polycarbonate membranes patterned and bonded into place.

#### 4.13 Five Layer Second Generation BIP

The development of a five-layered second generation BIP was focused on. A side view is shown in Fig. 53 of the five layered BIP that has two polycarbonate membranes sandwiched between two glass layers, and was topped with a PDMS layer that facilitated the input and output of the fluids. The bottom glass layer served as the bottom cap and the electrophoresis pre-separator, and the top glass layer was the optical cap. The middle two polycarbonate layers served as the nanopore molecular separators, and the crossed microchannel delineated the gate.

The top PDMS layer served as the fluid wells, ports, and electrical connections. Two glass layers were used in the second generation BIP, along with a clear PDMS cap, so

that each side of the gate could be viewed optically for testing, including the observations of separations and of the gate functions.

The key work was to further optimize the phenolic bonding process detailed previously, and to improve the clarity of the adhesive. During testing of the 1+ generation BIP, fluorescence of the phenolic-based adhesive was identified as a potential problem for optical detection. Three steps were taken to mitigate this problem. The first step was to thin the bond layer further, which required reformulation and an additional filtering of the solution to remove sub-micron gels that were present in the adhesive. A parametric study was conducted using 5 solvents (acetone, butanol, methanol, polyglycidyl methacrylate (PGMA), and toluene) to determine which solvent or combination of solvents reduced the gel concentration without decreasing the processing characteristics (spinning, wetting, uniformity) of the adhesive solution. These solvents were chosen for high solubility with phenol and formalin, which were the two major components of the phenolic-based adhesive used. The PGMA and butanol combination provided the best performance, and the relative amounts used for each were then further optimized. Figure 54 shows the



**Figure 54. Second generation BIP made with etched glass sandwich of two polycarbonate membranes that were patterned to form gate and microfluidic channels.**

A PDMS layer was used for input/output (IO) of the fluids.

clarity of the adhesive bond between two glass layers, without the membranes present. The characteristic yellow of the phenolic was reduced, although it was still detectable.

The second step was to adjust the cure schedule of the adhesive by dropping the cure temperature by 10°C and to increase the cure time and pressure. Decreasing the cure temperature slightly reduced the yellow color of the adhesive, which appeared to reduce the fluorescence of the glue layer. The increased cure time and pressure were needed to achieve the desired bond strengths and to further thin the bond thicknesses. Interestingly, the reformulation, filtering, and cure schedule adjustments also appeared to result in the stronger bonding of the polycarbonate membranes to the glass layers.

The third step was to change the order of the transfer process for the membranes. The membrane was transferred to the substrate employing the transfer process discussed earlier, and thermally bonded while the thermosetting phenolic resin was curing. Previously, each polycarbonate membrane was bonded on top of the next, starting with the semi-rigid substrate. The final optical cap layer was bonded last. Using this method, the final adhesion layer had to be the thickest, so that all the voids were filled that had accumulated because of the imperfections in each layer. As such, the top bond layer was the thickest, which was exactly where the fluorescence of the phenolic-based adhesive needed to be the lowest. Therefore, the procedure was changed to bond the stack starting with both glass substrates, and finished with the final bond in the interior layers, which were furthest away from the optical access.

Figure 55 shows the top and bottom of the second generation BIP, with a patterned PDMS layer bonded to the top glass layer. The PDMS on top contained the ports needed to access and test each of the cross channels. The previous 1+ generation used a single glass substrate with the electrophoresis layer with a membrane, capped by the PDMS input/output (IO) cap. However, the final generation BIP was designed with silicon and glass layers, and had intervening polycarbonate membranes. Therefore, the second generation BIP design met this design constraint.

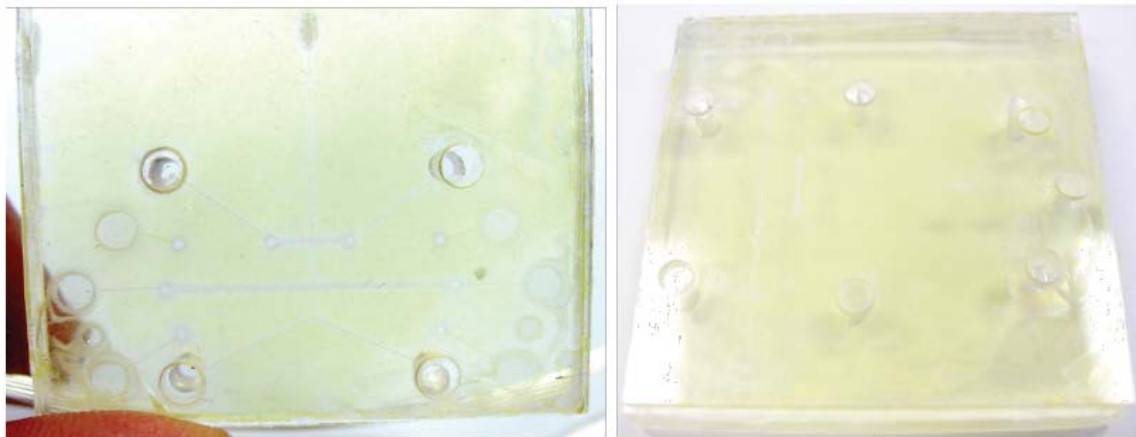


**Figure 55. Second generation BIP made with etched glass sandwich of two polycarbonate membranes.**

The two membranes were patterned to form the gate and the microfluidic channels. A PDMS layer was used for the IO of the fluids.

#### 4.14 A New Second Generation BIP

A new form of a second generation BIP was developed, which was used to test fluid flows for the separation, and included a platform for the active affinity gate. This BIP had glass slides for both the top and bottom layers, with 3 layers of polycarbonate nanopore membranes sandwiched in between them. This type of BIP was needed to test the sampling and the active gating. The key issue that needed to be resolved from the previous generation BIP was avoiding the plugging of the nanopores and the inner channels when the layers of the polycarbonate membranes were being built.

The bonding scheme developed used a phenolic adhesive spun on the polycarbonate membranes, which was mounted on a carrier. The phenolic/polycarbonate was then processed and bonded to the glass substrate. This process was repeated for each layer, and then the layers were partially cured. Isopropyl alcohol was then passed through the channels, which opened up the pores. The system was then fully cured. However, a problem arose with multiple layers. With the inner channels, a full flushing of the pores was not possible, and clogging of either the pores or inner channel often resulted,

reducing yields to a very low point. Therefore, a newer fabrication process needed to be developed.

Rather than spinning on the phenolic adhesive, the adhesive was sprayed on, and the areas for the pores were shadow masked. Figure 56 shows a polycarbonate nanopore membrane with a PDMS shadow mask, which was sprayed with phenolic adhesive. The PDMS mask was then removed, and the membrane was then bonded to the substrate. This process was repeated for each layer.

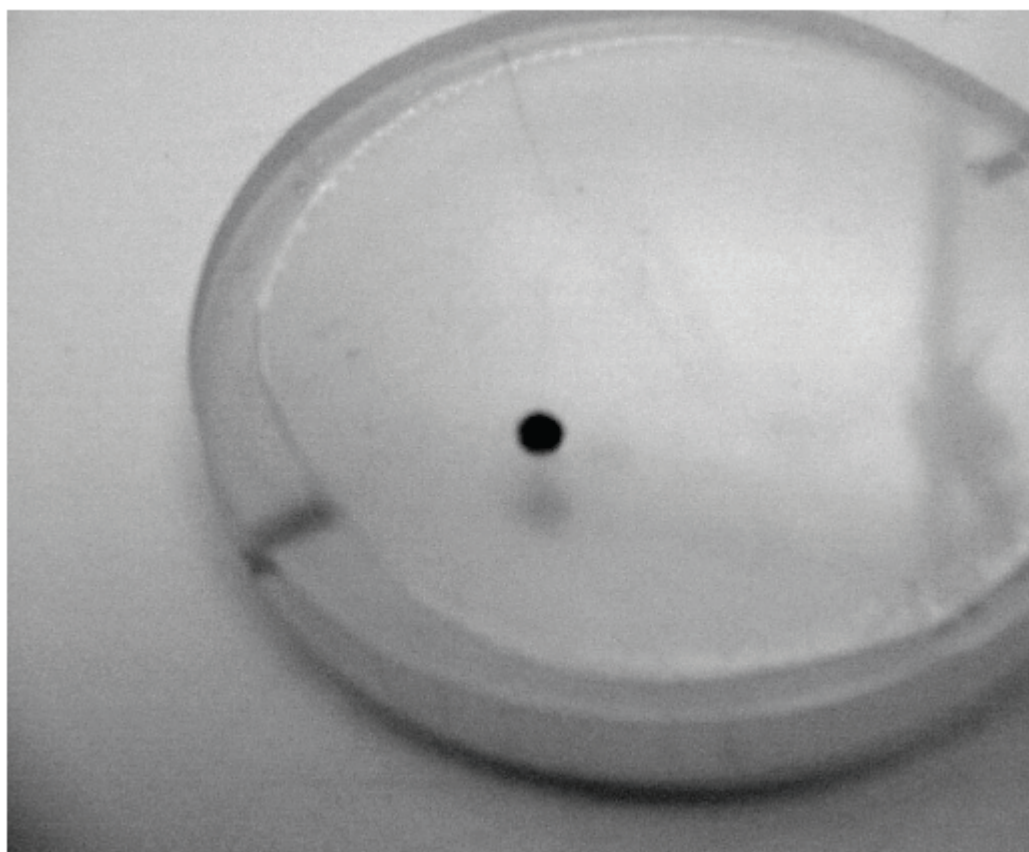


**Figure 56. A photograph of a nanopore polycarbonate membrane on a carrier that was sprayed with the phenolic adhesive.**

The black dot on the photograph was a PDMS shadow mask to shield the adhesive from plugging the nanopores.

This process produced better yields than the previous spinning process produced, but further improvements were still needed in both the masking and the spraying.

Difficulties were still being experienced with the full coverage of the adhesive, and a better way was needed for the shadow masking.

#### 4.15 Atomization Spray

For the first issue, an atomization spray was used. This type of spraying has issues with generating a relatively large distribution in droplet sizes, which makes very uniform thin layers difficult to create, and there are problems with the turbulent fluid dynamics stochastically altering the flows around the shadow masks. To solve these issues, two tacks were taken: one was to investigate electronic- (e-) spraying the phenolic adhesives, and the other was to investigate ultrasonic atomization for smaller droplet size in a low pressure container, which would mitigate turbulence.

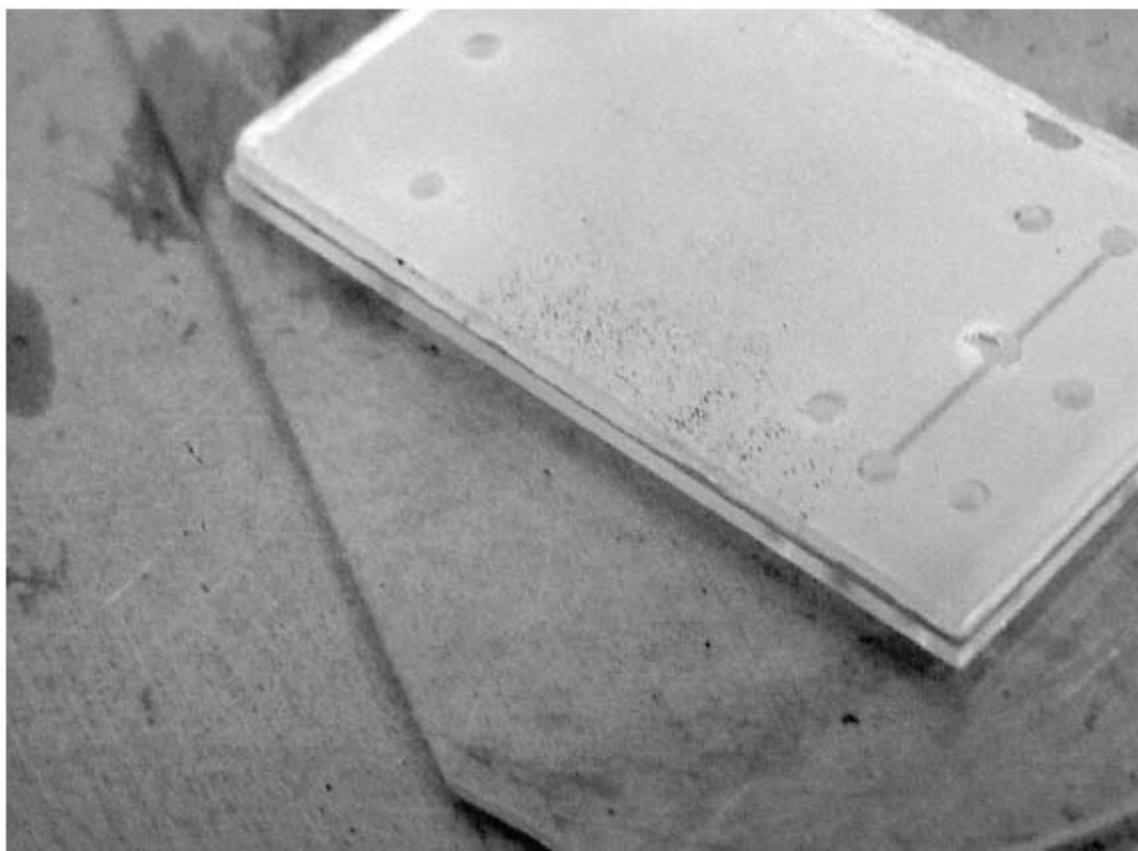


**Figure 57. The next generation BIP.**

Two etched glass layers that sandwiched polycarbonate membranes that were patterned to form gate and microfluidic channels. In this version, the spray process was utilized.

#### 4.16 Fabrication of the next generation BIP

The fabrication of the next generation of BIP began by incorporating active gates in the sandwiched structure as previously reported. This new device was revised from previous versions to better test the gating functions, which required new mask sets, substrate sizes and membrane processing, as noted above. The photograph in Figure 57 shows the new configuration, which had simpler crossed tees for the three gate layers. This device used the atomization spray process described above. Further work was needed on mask alignment for the gates, and in more closely delineating the gating regions.

#### 4.17 Active Nanogate Fabrication

For the active affinity gates, the polycarbonate was coated with a thin gold layer so that the thiol compound interactions would occur. The Au layer was first deposited with an electroless deposition technique. The Au was needed on the inside of the pores. The Au on the surfaces of the membranes first either had to be removed or covered with a dielectric layer that prevented fluid contact. The electroless deposited Au was very thin (1 to 10 nm). This deposited Au was removed simply by applying adhesive tape to the membrane and pulling it off. This worked fairly well, but some Au was left behind, and the remaining Au was uneven. Therefore, different methods were investigated to remove the surface Au, but leave the pores coated with Au.

Some Au was also needed outside of the pores to conduct the bias to the gate regions. For the electrical contact and for strength, electrical leads on the outside of the pores needed to be fabricated, and this Au needed to be thicker than the Au for the pores.

Two methods were investigated to remove the surface Au. A surface was sputtered using a low power argon plasma, and another surface was selectively etched using a Au

etchant. The sputtering appeared to work well, but it was then necessary to verify that sufficient Au remained within the pores. The second method of using an Au etchant was useful, since the Au leads also needed to be patterned. Thus, it was possible to chemically removing the Au from all places except the pore and lead region. The extra Au was applied using the e-beam evaporator built for this project. Issues that still needed to be addressed included applying the Au at low enough power levels to prevent the polycarbonate from being damaged.

#### 4.18 Improving the fabrication of the BIP

To solve issues with patterning gates in the multistacked layers, the fabrication of the affinity gates with Au patterning was examined. In previous work, a phenolic based adhesive was developed to bond multiple layers of polycarbonate together within a sandwiched etched glass structure. To overcome plugging of the nanopores caused by spinning the phenolic adhesive, a spraying process was developed, using a shadow mask to cover the gate region. This process was successful in bonding the stack together. However, there were three main drawbacks. The shadow mask required pick-and-place masking, making alignment very difficult and not truly scalable to larger numbers of gates. The spraying was uneven, with too much adhesive supplied in some regions and not enough in others. This problem was potentially solvable with further engineering of the spray system, and continued to be addressed due to its many advantages in processing multiple layers. However, the most difficult issue to be resolved was that this method generated large address areas, and thus leakage occurred around the crossed gate region.

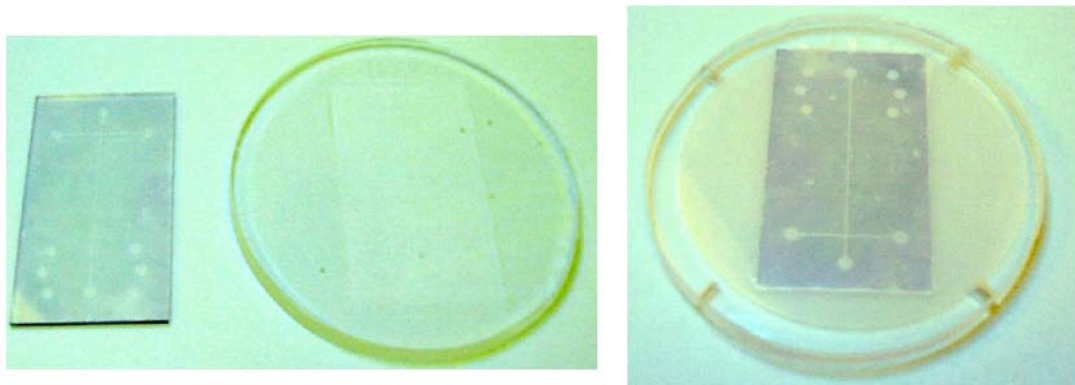


**Figure 58. (Left) Phenolic adhesive transferred to glass using a PDMS platen. (Right) Polycarbonate nanopore membrane transferred to glass.**

#### 4.19 Transfer Printing Process

To solve the issues with shadow mask spray adhesion, a new modified adhesive transfer printing process was developed. In Fig. 58 is shown the transfer printing process, in which a specially formulated phenolic adhesive was spun on a PDMS platter, which was then subsequently used to pattern the glass wafer that was already etched. With this scheme, only the glass in contact with the PDMS glue layer received adhesive. The etched-in portions remained free of adhesive, and thus a subsequently bonded polycarbonate membrane was not in contact with the phenolic where the etched channels were, therefore preventing any potential plugging of the nanopores. In addition, the adhesive layer was automatically patterned by the substrate to which the adhesive was transferred, which resulted in high quality bonds around the gate areas, as well as achieving the same resolution and size as that defined by the channels. Note in Fig. 58(left) that the glass pattern was transferred to the PDMS carrier platen, such that where the glass was in contact with the phenolic adhesive, it was transferred to glass substrate. While this method had proven successful, there were several issues that needed to be addressed for it to work optimally.

The method worked when the solvent and the solute completely wet the PDMS platen with thin, uniform layers (1  $\mu\text{m}$  thick). Wetting and feature transfer were highly

dependent on the solute and the solvent. If either the PDMS did not wet properly, or if the PDMS wetted better than the substrate, then the pattern did not transfer evenly. For these conditions to be met for both the PDMS and the glass (which was the first desired substrate), the phenolic resin needed to be reformulated to use pure ethanol as the solvent. For this case, Fig. 58(*right*) shows the transfer of the polycarbonate membrane to the glass substrate. In addition to being very robust for the polycarbonate to glass bonding, the reformulated mixture also had the added benefit of greater clarity and less yellowing than the previous mixtures that were used.

The same transfer printing scheme was not possible for transferring the phenolic resin from the PDMS to a polycarbonate substrate, as would occur when bonding the middle channel layers. The issue was wetting. The polycarbonate layer wetted much less than the PDMS, therefore, the phenolic adhesive did not transfer cleanly and sharply. The Polyvinylpyrrolidone (PVP) free Polycarbonate Track Etch (PCTE) nanopore membranes used for the molecular valves, mass selective, and the affinity gates were strongly hydrophobic, and thus wet poorly with the alcohol and polar solvents used for the phenolic adhesives. Methodologies for making the surfaces more hydrophilic, such as using oxygen plasma treatment followed by mild ammonium hydroxide treatment, did improve the transfer, but were still not good enough for these purposes. Using PVP coated PTCE limited the separation capabilities (both surfaces needed to be available), and it still did not wet sufficiently well for transfer. As discussed below, other methods to improve the transfer of an adhesive layer to the PCTE substrate from the PDMS platen were investigated.

#### 4.20 Transfer of Polyimide Middle Channel Layer.

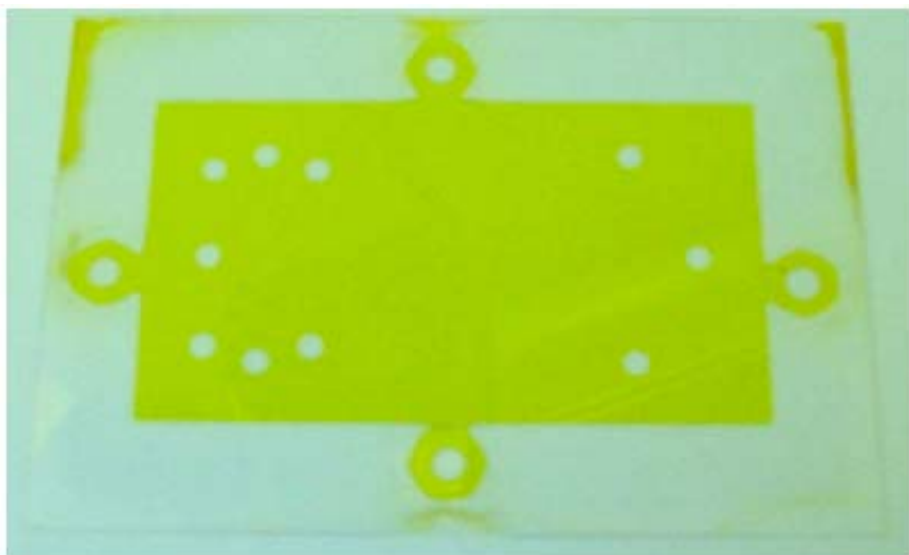


**Figure 59. Polyimide patterned on a carrier glass.**

Polyimide is a polymer that could use the transfer printing process using PDMS, as it can be made to have greater affinity for polar solvents. Fig. 59 shows an etched and patterned polyimide layer on a glass carrier plate. Fig. 60 shows the polyimide middle channel layer transferred on top of a nanopore PCTE membrane, which was supported on an etched glass substrate. The process was robust, did not leak, and was sufficiently

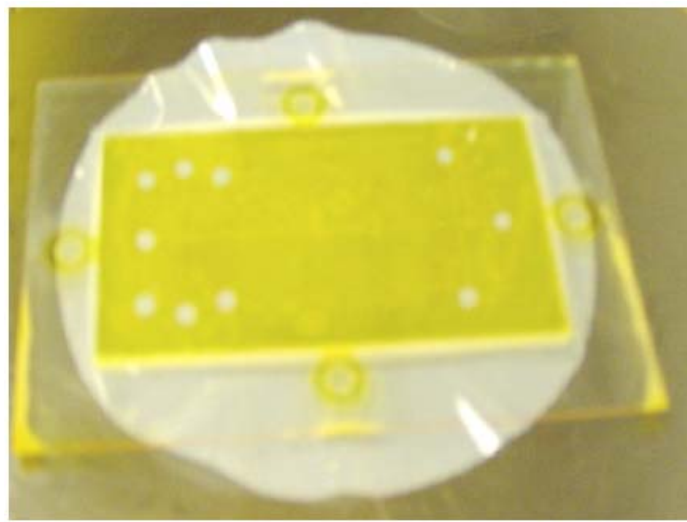


**Figure 60. Full stack bonded via transfer printing and bonding.**

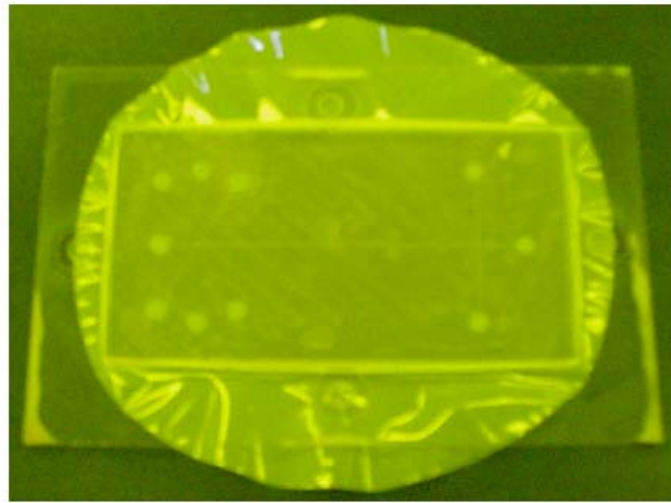


**Figure 61. Bonded PC membrane to bond the polyimide middle layer.**

repeatable to build a multilayer stack. In addition, the polyimide was easier to pattern than polycarbonate, which took longer and was more sensitive to degradation in an oxygen plasma. The main issues with using polyimide as the middle channel layer (Figures 61, 62) were the potential for the fluorescence of PI interfering with detection signal, and separations being less efficient by having a mixture of polycarbonate and polyimide channel walls.

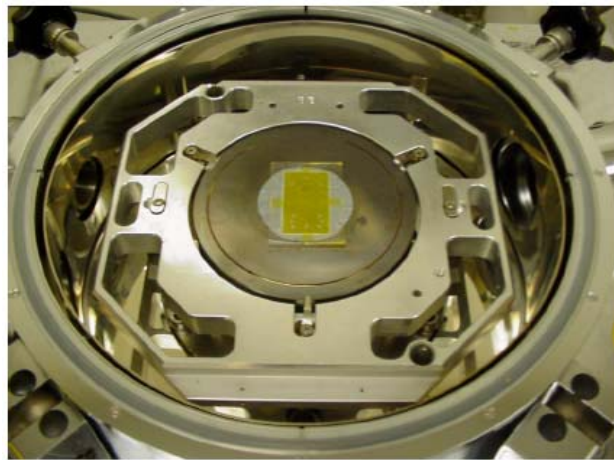


**Figure 62. Thermal bonding of the polyimide middle layer to the nanopore polycarbonate layer.**

Other methods were also investigated that avoided using the polyimide middle layers. One method was to functionalize the PCTE to make it sufficiently wettable for use in the transfer printing process. The other was to use an adhesives composed of a low molecular weight polycarbonate oligomers in appropriate solvents that could wet polycarbonate.

#### 4.21 Gold Deposition for Affinity Gates

Au was electrolessly deposited on PCTE nanopore membranes, and was then patterned to individually address each crossed channel region defining a gate. Figure 63 shows a TEM micrograph of a section through a membrane which was Au plated within the pores, which left the pores opened for fluid flow. The pores were originally 650 nm in diameter, and were reduced in size by approximately 30%. The plating of smaller pores was evaluated, but there was blocking of the pores. With electroless plating, all of the surfaces were coated with Au. The first method tried to remove the surface Au was to use tape and simply remove the unwanted exterior surface Au mechanically. This method left smatterings of Au and other compounds on the surface, which was not desired. In addition, the Au was not easily patterned.

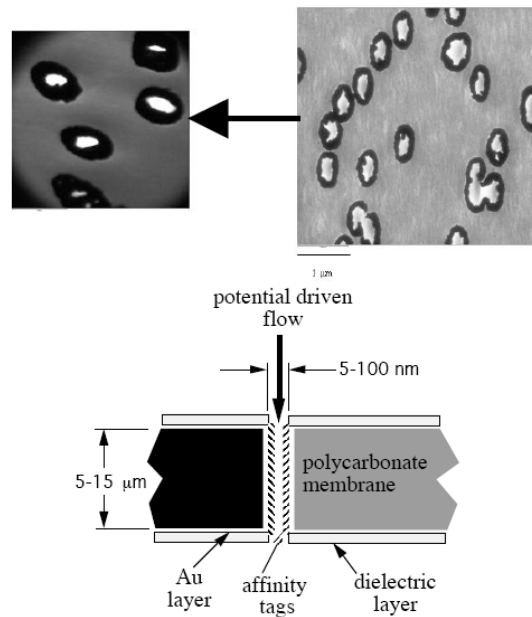


**Figure 63. Deposition of Au in nanopores for the fabrication of the affinity gates.**

#### 4.22 Increased Clarity of the BIP Stack.

A new fabrication process was developed to improve the clarity of the BIP stack. A phenolic based adhesive that was previously developed to bond multiple layers of nanopore polycarbonate together with polyimide as the intervening microchannel layers within a sandwiched etched glass structure lacked clarity. A new fabrication process incorporated two innovations to improve on the last BIP: (1) a low temperature adhesive, and (2) Polymethyl Methacrylate (PMMA) channel layers. The PMMA channel layers replaced the polyimide layer to reduce the fluorescence of the polyimide and to make the layer optically clear. The new low temperature adhesive replaced the previous phenolic-based adhesive to achieve better bond strengths at lower temperatures ( $<120^{\circ}\text{C}$ ), which improved the performance of the nanopore polycarbonate membranes. The previous bond temperature needed to be above  $150^{\circ}\text{C}$  for maximum strength, which was above the glass transition temperature of the polycarbonate. In addition to the lower bond temperature, the new adhesive was optically clear, whereas the phenolic took on a yellow tint as the cross-linking increased, even at the lower temperature ( $<140^{\circ}\text{C}$ ) formulation.

The new low temperature adhesive (i) spin coated well, (ii) contact printed with sufficient resolution so as not to block the channel gaps, (iii) bonded polycarbonate to glass with sufficient strength for carrier removal and further processing, (iv) bonded PMMA to polycarbonate with sufficient strength for carrier removal and further processing, (v) did not fluoresce (optically clear), and (vi) bonded at temperatures below  $120^{\circ}\text{C}$  to be compatible with all the materials used. In Figure 64 is shown a photograph of a glass substrate with etched channels. Processing with this new adhesive formulation required a great deal of process work to balance each of the competing parameters. Balancing the adhesion of the PMMA to its carrier (coverglass), and the release after transfer, were also significant developments.

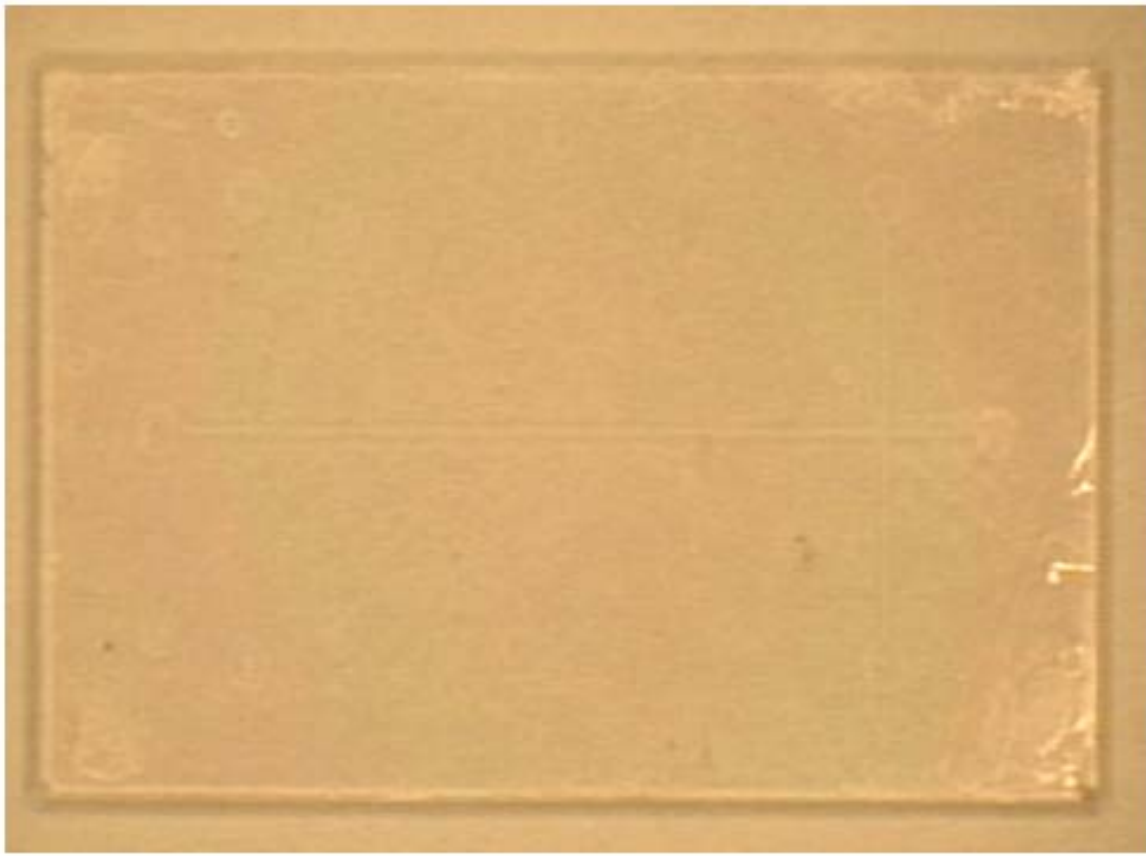


**Figure 64. Photograph of a glass substrate with etched channels which has a thin layer of the new thermoplastic adhesive covering the top surface.**

This adhesive layer was transferred to the top surface of the glass channel piece via a process called contact printing. In contact printing an adhesive carrier, e.g. a PDMS puck, was first coated with adhesive. This carrier was then pressed into contact with the glass and the adhesive transfers where it makes contact.

In the following photographs the structures appear much darker than they actually were so that the etching features of the BIP are clearly visible, since now all the layers were quite optically transparent. A completed stack of glass (Fig. 65), polycarbonate nanopore membrane (Fig 66), and then PMMA channel layer (Fig. 67 and Fig. 68) are presented, all of which were transfer bonded. This demonstrated that an optically transparent multiple stack BIP could be fabricated with the nanopores open between microfluidic channels. The remaining images show different aspects of the process steps, with close-ups of the cross channel molecular gate structure.

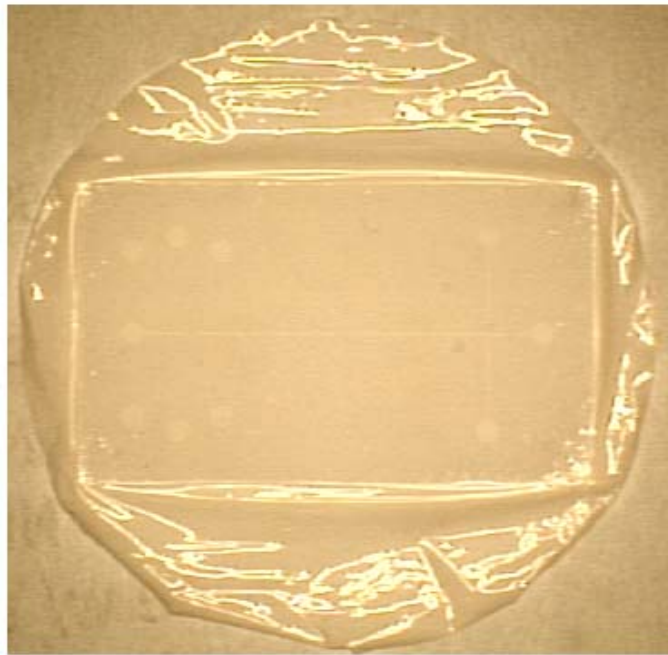


**Figure 65. Photograph of a polycarbonate membrane bonded to a glass channel piece.**

This image demonstrated that the glue layer bond was uniform and sharply confined (i.e. did not extend into or across the channel).

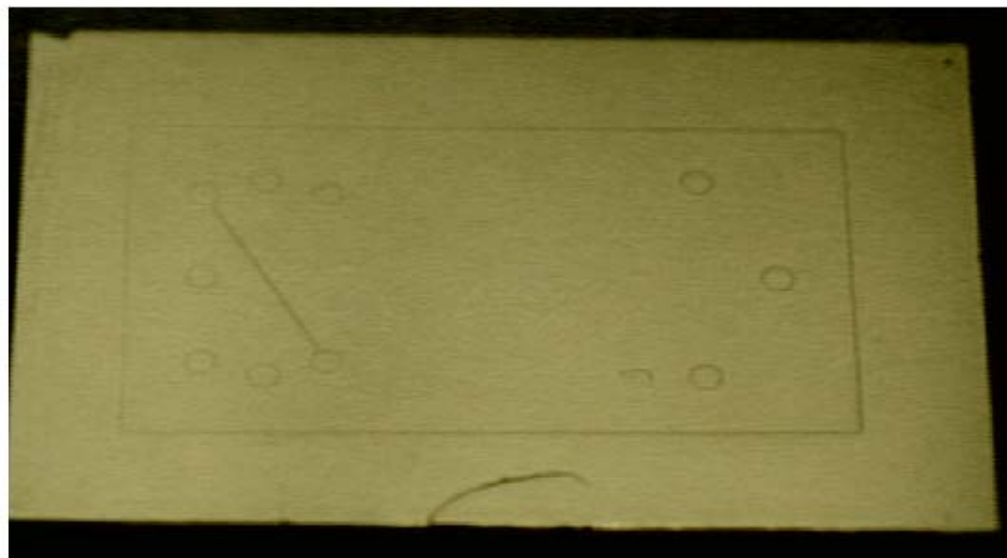


**Figure 66. Photograph of a PMMA channel layer on a coverglass carrier.**

The PMMA layer was patterned using an oxygen plasma and a shadow mask. Sharp feature contrast and good resolution pattern transfer were obtained. Manipulation of the surface chemistry of the coverglass enabled the balancing of the bonding strength of the PMMA to its carrier. Too much bonding, and the layer would not transfer off the carrier, too little and the layer would peel, buckle, and form creases before bonding, which would interfere with the processing.

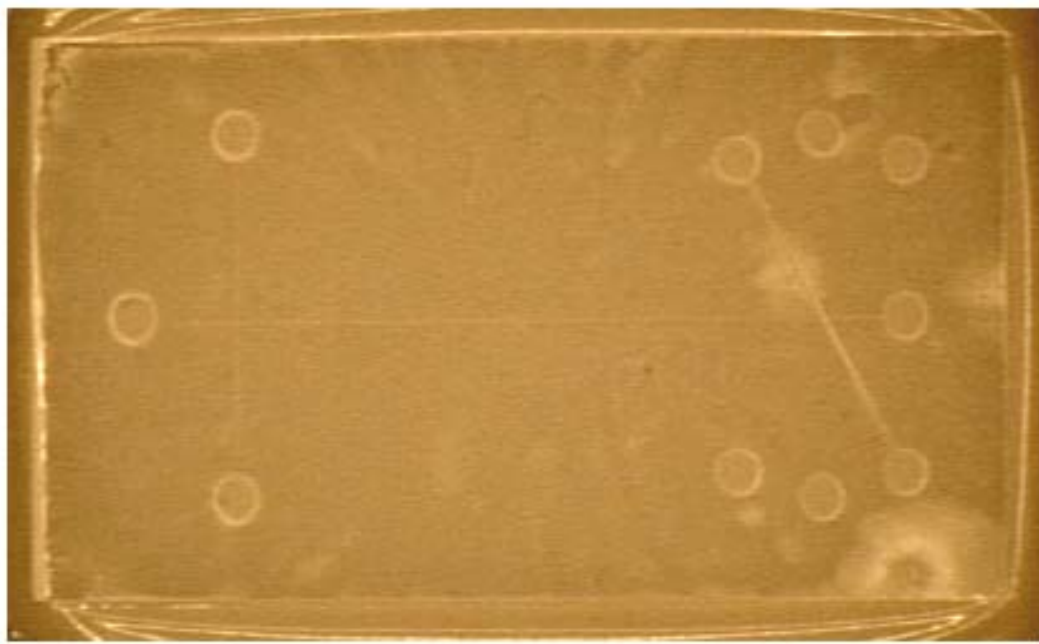


**Figure 67. Photograph of a bonded stack of layers.**

(a) glass channel piece on bottom, (b) a circular polycarbonate membrane in the middle, and (c) a PMMA channel layer still attached to its carrier on top. On the right side of the image the glass channel and the PMMA channels cross.

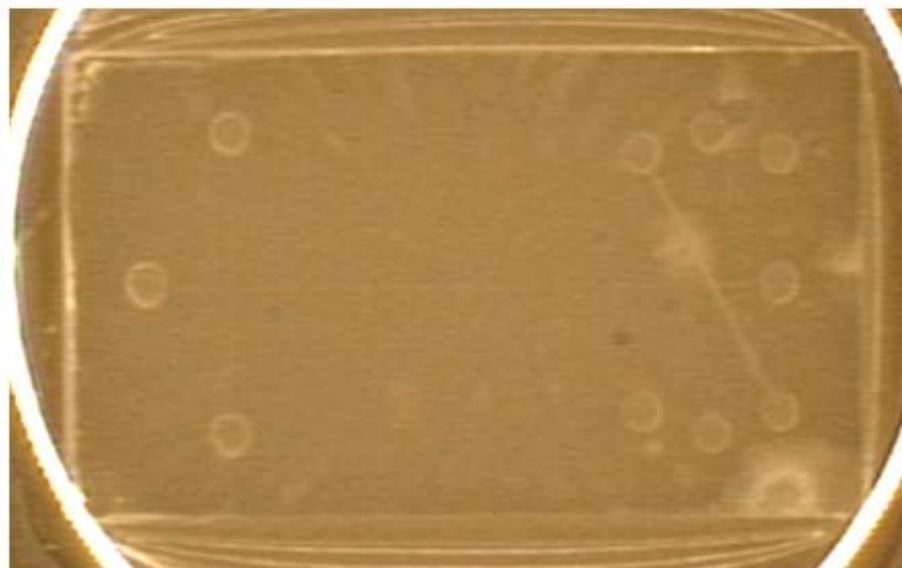


**Figure 68. Another photograph of the bonded stack of layers.**

Similar to Fig. 64, but with a farther viewpoint to show more clearly the extent of the polycarbonate membrane and the PMMA carrier.

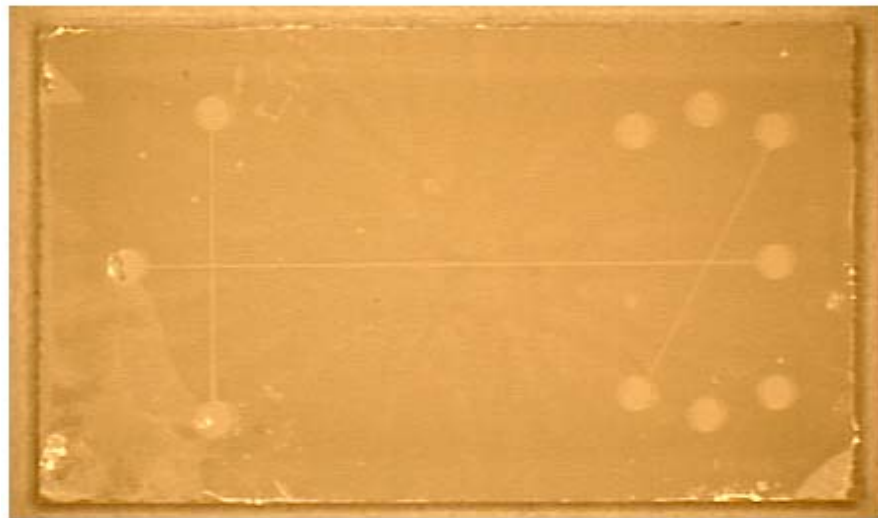


**Figure 69. Photograph of the stack of Fig. 67 with the PMMA carrier and the polycarbonate excess removed.**

The image demonstrated the successful bonding and transferring of a PMMA channel layer (the first successful transfer).

The new fabrication process incorporated an optically clear low temperature adhesive, and PMMA channel layers were developed. Both changes needed to be tested for fluorescence and separation performance, and the process and chemistry optimized. With respect to fluorescence (Fig. 69) the signal from the previous generation of device that used polyphenol and polyimide exhibited relatively low contrast between the fluid channel and structure, which was thought to be an issue at very low concentrations. The same test showed in Fig. 70 the high contrast for the new fabrication process with the optically clear and low fluorescence adhesive and PMMA channel layer.



**Figure 70. Magnified photograph of the crossing channels (Fig. 69).**

A sharply defined channel intersection is shown. The double images were caused by reflections off the glass slides.

#### 4.23 Eight Layer Stacked BIP

In Figure 71 is presented a photograph of an 8 stacked layered BIP chip with a glass based separation layer, three nanopore polycarbonate membranes, three PMMA microchannel layers, and a Polyethylene Terephthalate Glycol (PETG) capped layer.

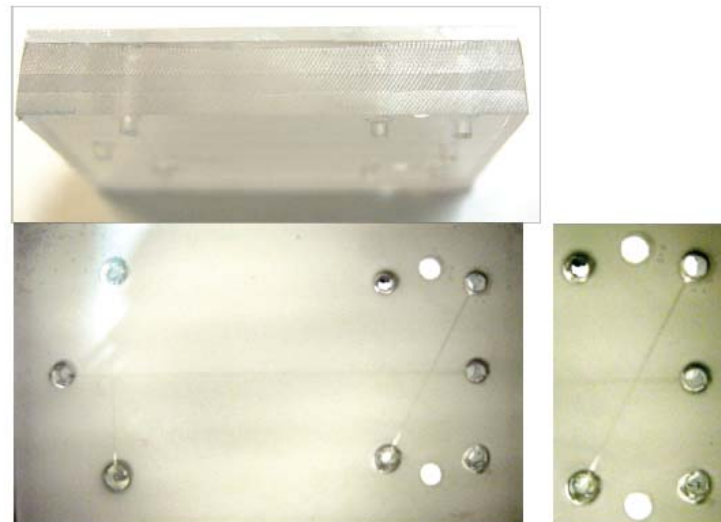


**Figure 71. Photographs of the 8 Layered BIP chip.**

8 stacked layers of a glass based separation layer, 3 nanopore polycarbonate membranes, 3 PMMA microchannel layers and a PETG cap layer.

Figure 72 showed 220 nm outer diameter (OD) Au nanotubes quiescently plated from one side. A number of techniques were investigated for Au patterning using contact printed masks of polymers. The polymers were patterned either photoactively or via shadow masks. The Au was then removed from the exposed areas by etching.

The ability to coat the interior surfaces of polycarbonate track-etched nanocapillary arrays with initial diameters of 200 to 650 nm with gold via an electroless deposition procedure was demonstrated. These nanotubes were easily imaged by SEM after the surrounding polycarbonate was etched away. Thin sections of the gold nanotubes imaged by transmission electron microscopy (TEM) showed that the gold lining extended uniformly throughout the structures in Figure 73.

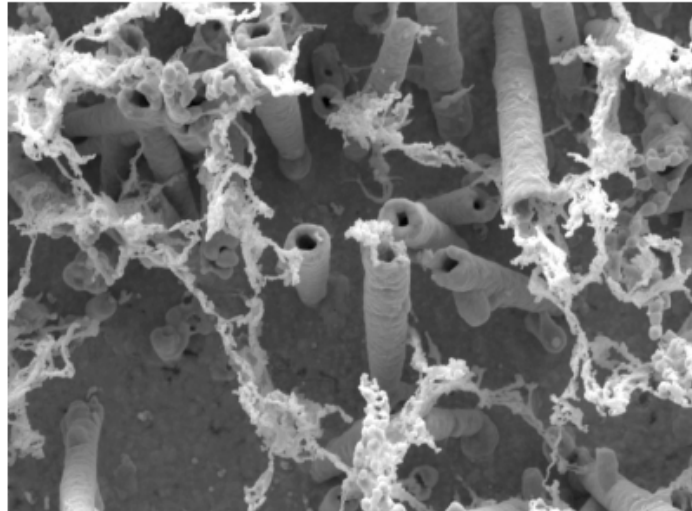


**Figure 72. Gold nanotubes that were electrolessly plated into 220 nm polycarbonate nanopore membranes.**

The membrane was plated from one side only. The opposite side was then etched back in an oxygen plasma to remove the polycarbonate to reveal through Au nanotubes, with inner diameters of 100 nm.

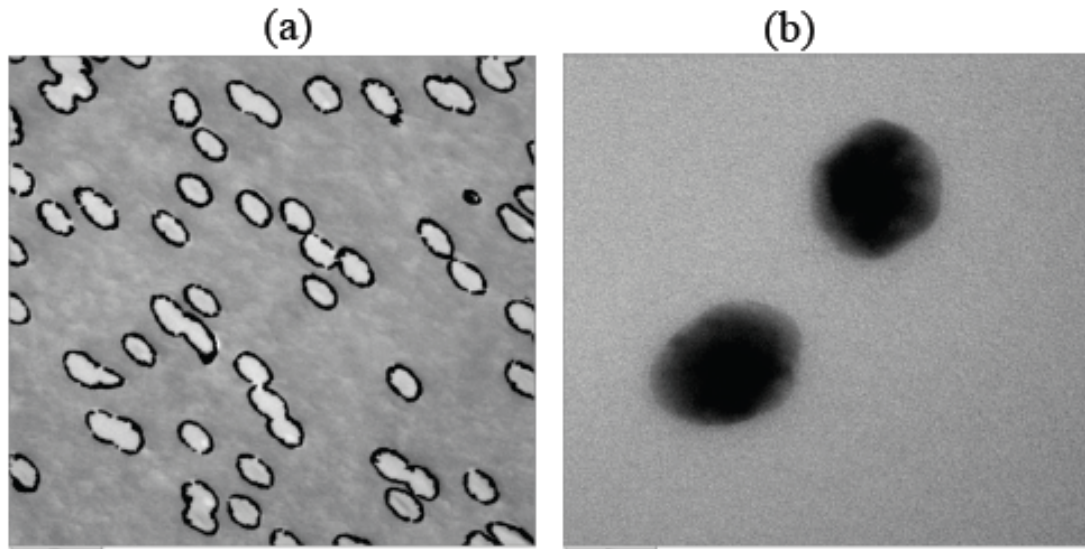


**Figure 73. TEM micrographs of gold plated nanopores.**

Gold coating of smaller nanocapillary arrays (< 200 nm) provided a greater challenge, both in terms of reproducible compositions and microscopic imaging. For example, TEM images of the gold-lined 30 nm pores seen in Figure 73b reveal gold wires rather than tubes, which implied a process whereby gold had completely filled the pore. However, gas flux measurements from Charles Martin's group at the University of Florida showed that these gold plated nanopores actually had an average inner diameter of 2-3 nm.

For affinity to the botulism affinity tag, gold coating of the larger nanocapillary array was sufficient. The goal here was to create a high surface area template that would allow botulism neurotoxin A to pass into the pore, where it could be captured by a surface bound affinity tag. After capture, the two could then be electrochemically released. Tags bound with botulism could be easily separated from unbound tag by molecular weight, and subsequently detected by fluorescence.

#### 4.24 BIP Chip Fabrication

Channel definition was markedly improved by the optimization of the conformal bonding technique. Dimensional uniformity was controlled and reproducible, and side seepage from the channels was virtually eliminated. Bonding of the top cap layer continued to persist as a difficult final hurdle to overcome. Polyethylene Terephthalate Glycol (PETG) was investigated as a good candidate as a cap layer due to its (a) low temperature thermoforming, (b) its optical clarity, and (c) its strong bond to properly treated polymer and glass surfaces. The ability of PETG to thermoform to the membrane stack was important in two regards. First this cap layer must be easily machineable to accept connection to the macro-fluidic world of pipettes and micro-tubes. Secondly, it must “seal” to the membrane stack to maintain the integrity of fluidic paths.

The degree of thermoforming required by this cap layer was significant due to the polycarbonate membranes having a non-uniform thickness, which would incorporate a sinusoidal “waviness” to the membranes thickness with a period of 6-8 mm across the surfaces, and would be evidently inherent from the nanopore fabrication process. PETG exhibited excellent bonding to the membrane stack and demonstrated excellent thermoforming ability. At this point the BIP microfluidic design included the membrane stack, the PETG layer, and the top acrylic layer, as shown in Figure 74. However, the thermal stresses incorporated were so great that within a day or so after bonding the bottom glass layer in the BIP cracked and the microfluidic channels were filled. A new approach, where the PETG layer was significantly thinner and was sandwiched between the membrane stack and an acrylic layer to minimize its thermal expansion effects, was tried next.

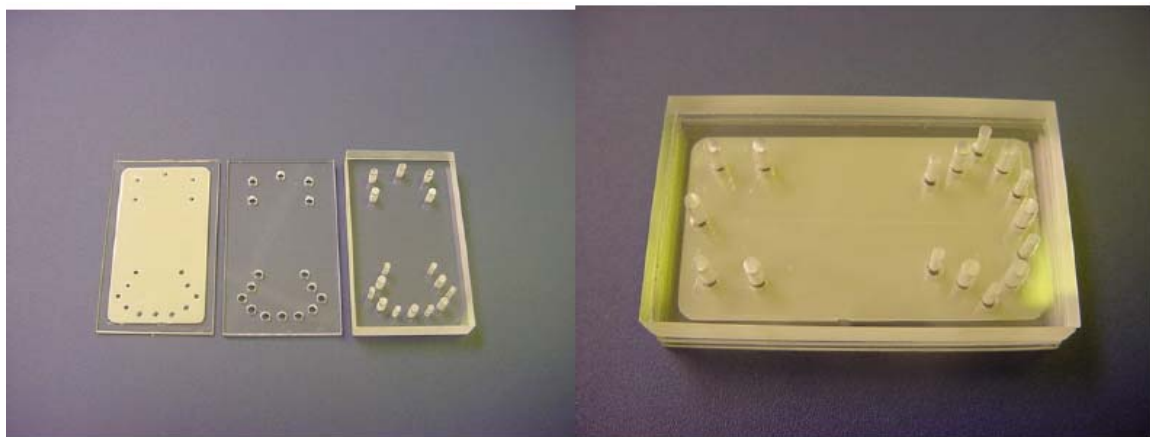


**Figure 74. Photographs of the BIP chip design showing (left) the cap assembly before bonding and (right) the assembled BIP.**

The cracking of the BIP glass layer, when the microfluidic channels were filled with water, highlighted a potential problem with the adhesive. In addition, electrical testing of the chip raised other areas of potential concern. These two concerns revolved around Nafion as the choice for the backbone of the polymer adhesive. Nafion tended to swell slightly in the presence of water. The adhesive layer was exceptionally thin, and the membranes decently malleable, such that these pressures were deemed to be manageable, but any additional pressures normal to the surface of the chip were of concern. Also, Nafion had a tendency to be a proton conductor. Once again, the layer was sufficiently thin to minimize such an effect, but this effect might add to the electrical noise level of the chip.

An alternative to the use of Nafion was Cytop, which was similar to Nafion in that both were fluorinated polymers with excellent optical clarity and low temperature bonding. There were a number of chemical and physical similarities, but most importantly, Cytop did not absorb water, nor did it conduct protons. Initial trials for the substitution of Nafion with Cytop in the adhesive mixture were encouraging.

#### 4.25 Nano-Affinity Gate Fabrication

The patterning and electrical connection of the nanopore membrane and intermediary layers was investigated. Shown in Figure 75 is a bottom glass layer patterned with electrode leads to the channel crossover area. Shown in Figure 76 is the electrical connection pins that were attached to the top acrylic cap layer, which were then connected to the electrodes patterned on the intermediary layers.

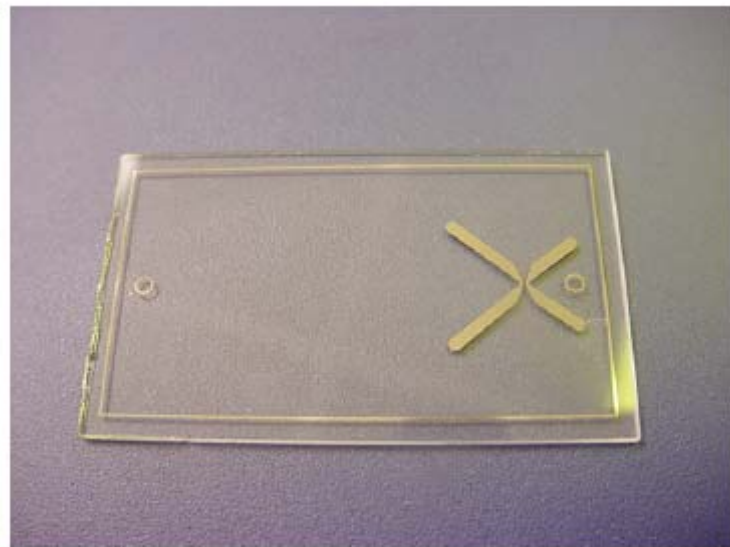


**Figure 75. Glass bottom layer with patterned metal leads for molecular gate interconnection.**

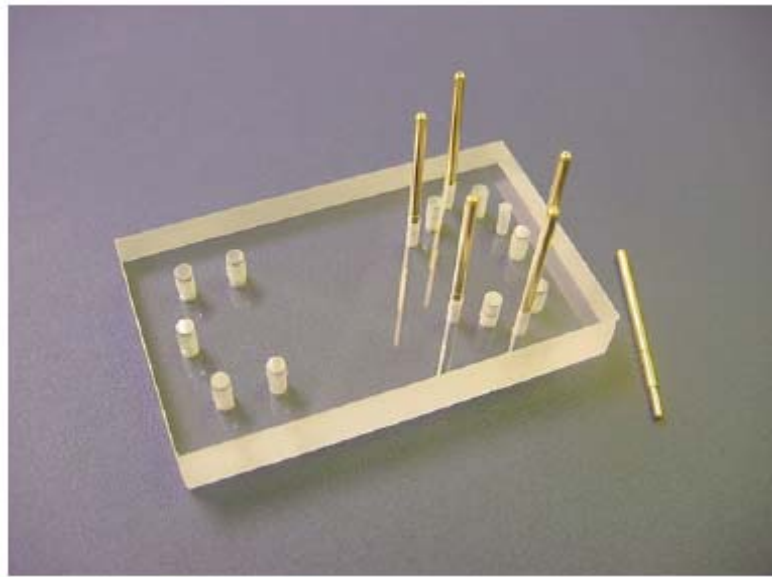


**Figure 76. Top acrylic layer with pin connectors to serve electrical connections from the outside world to the molecular gate region.**

#### 4.26 Affinity Gate Fabrication/Operation

Advances towards fully integrating the gold-coated affinity gates within the microfluidic devices continued. One challenge that had to be overcome was that of performing an electrochemical desorption on the complexed and uncomplexed thiolated affinity tags on the surface of gold-coated nanopores. Transporting the desorbed affinity elements via conventional electrokinetic transport required complicated chip fabrication and/or instrumental strategies to effectively decouple the 1.1 V electrochemical potential applied to the Au membrane from the 500-1000 V potentials applied across the microfluidic channels, which were required for electrokinetic transport. To circumvent this problem, a new Pt electrode configuration was explored which allowed fluid in the microfluidic channels to be pumped electrokinetically while positioning the Au coated affinity gate in a field free region of the microfluidic channels (Fig. 77). In this way, the electrochemical potential applied to the membrane was decoupled from the potential applied to the microfluidic channels.

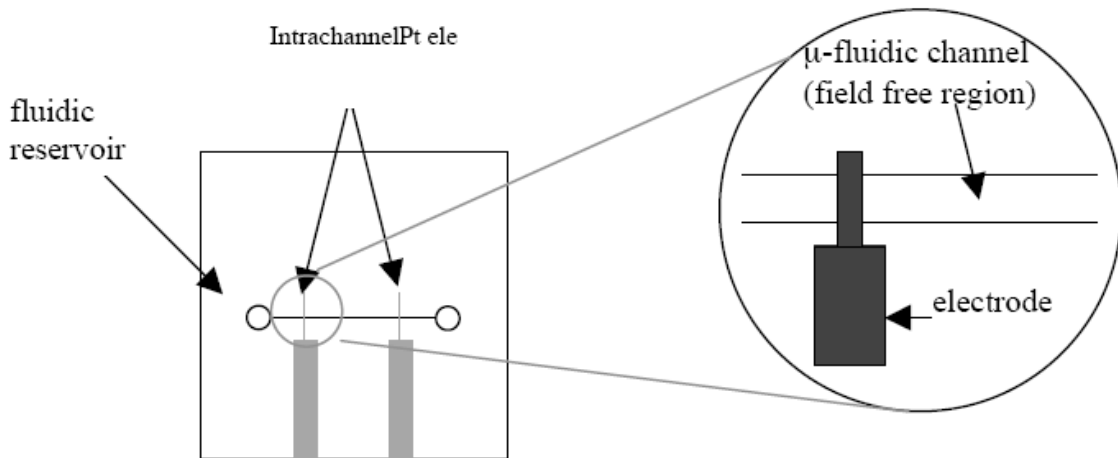


**Figure 77. Schematic of the proposed arrangement of Pt electrodes to be fabricated within the microfluidic channels.**

These electrodes served as the cathodes while Pt wire electrodes, placed in on-chip fluidic reservoirs, served as the anodes. Potentials applied between these electrodes would establish an electric field, which would drive the electroosmotic flow of fluid between the inlet via of the reservoirs and the intrachannel cathode electrodes. The remainder of the microfluidic channels constituted of a field free region. Fluid flow in this region would still be established because of the displacement of fluid occurring between the anode and cathode.

Devices fabricated according the schematic shown in Fig. 77 were constructed by first creating Pt electrodes on glass surfaces. Once the Pt was patterned onto the glass, microfluidic channels were created in PDMS using the rapid prototyping techniques. Monoliths of PDMS contained the channel features, were treated with O<sub>2</sub> plasma, and then bonded to the Pt coated glass substrate to form a microfluidic channel containing Pt electrodes.

A device within a structure that conducted electrokinetic separations and manipulations was fabricated with microfluidic channels that carried the bulk of the fluid flow, and were separated by nanofluidic membranes. The design and fabrication of the device incorporated patterns of microfluidic channels into multiple stacks of polymer layers on

rigid silicon and glass substrates, and allowed optical access. To realize the device, a multi-layer fabrication construct was developed. An important issue within this construct was the adhesive layer that held the polymer layers together. A custom adhesive was developed due to the unique and restrictive constraints on this material. The adhesive had to be (a) optically clear (for fluorescent inspection of the channels), (b) curable at low temperature (the nanoporous membranes can handle a maximum temperature of 140 C), and (c) patternable to a resolution of a few um. Improvements in our adhesive chemistries resulted in: (1) improved sealing of the polymer layers when exposed to water (further improvements were necessary to withstand the large wicking forces of liquids within the nanopores), (2) improved bond strength (significant improvements were made in this area to accommodate the thermal stress inherent in the multi-layer stack design), and (3) improved resolution, or geometric control, of the adhesive layer.

Another critical issue within this construct was the top layer attachment (or “cap” layer). For both macroscopic fluid connections and macroscopic electrical connection this final layer needed to be significantly thicker than the other layers. The fabrication process for the nanoporous membranes inherently produced a sinusoidal variation of thickness across the membranes, resulting in a non-planar top surface onto which the cap layer needed to be bonded. Polyethylene Terephthalate Glycol (PETG) was investigated for this role due to (a) its low temperature thermoforming, (b) its optical clarity, and (c) its strong bonding to properly treated polymer and glass surfaces. However, PETG bonding incorporated significant thermal stresses into the polymer layer stack, a problem which was addressed with changes in the bond process, the addition of strain relaxing layers, and further improvements in adhesive layer bond strength. Almost the entire thickness of the device was the top cap layer. Good optical clarity and sharp channel resolution were achieved.

A final critical issue with this construct was the electrical connections within the device, especially to the nano-porous regions at the intersection between the microfluidic

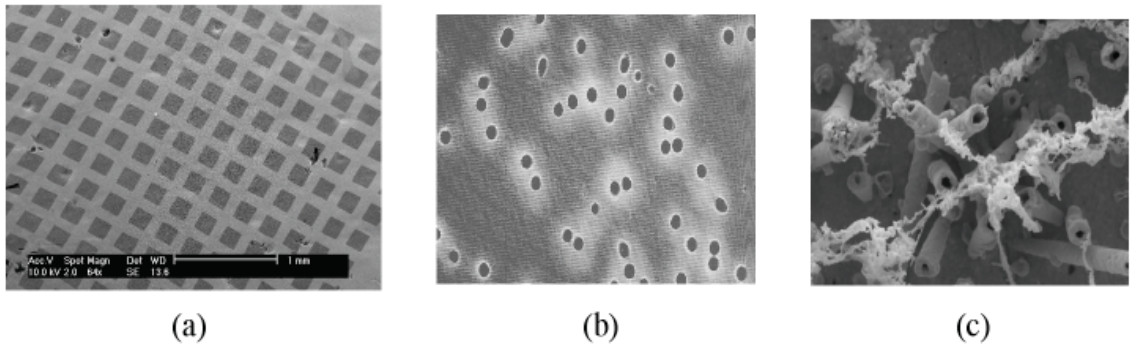


**Figure 78. Electrical connection to the interior of the nanopores.**

(a) Selective patterning of the polycarbonate membranes. (b) SEM micrograph of the nanopores, (c) Au-filled nanopores followed by etching of the polycarbonate to produce free-standing Au nanotubes.

channels. Figure 76 shows how electrical connection were made from the outside world though pin connections along patterned electrodes to the nanoporous region, and Fig. 78 shows how electrical connection were made to the nanopores. Metal electrodes were patterned on the nanoporous material, getting the electrical connection to the pores, and then the interiors of the nanopores themselves could be uniformly coated with metal, thereby providing electrical control, or monitoring, of the nanopore potential during operation of the device.

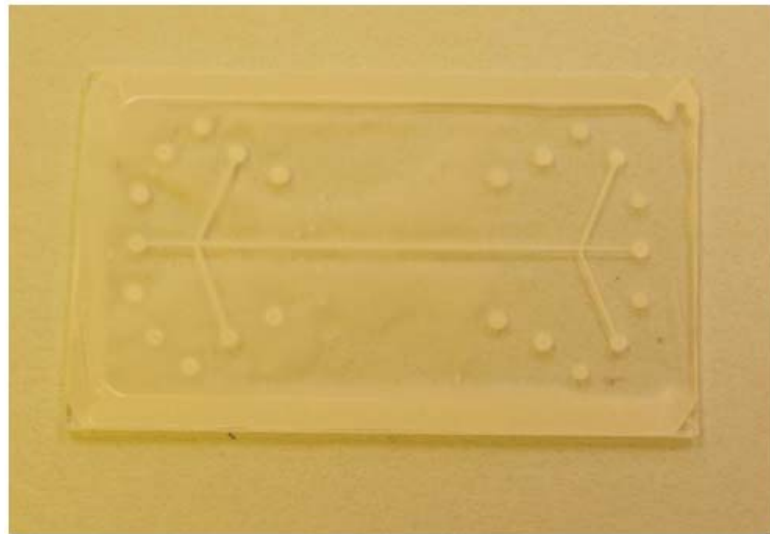


**Figure 79. Device design having three microfluidic channels.**

The channels connected through a 200 nm sized nanofluidic membrane, which made two nanofluidic gates.

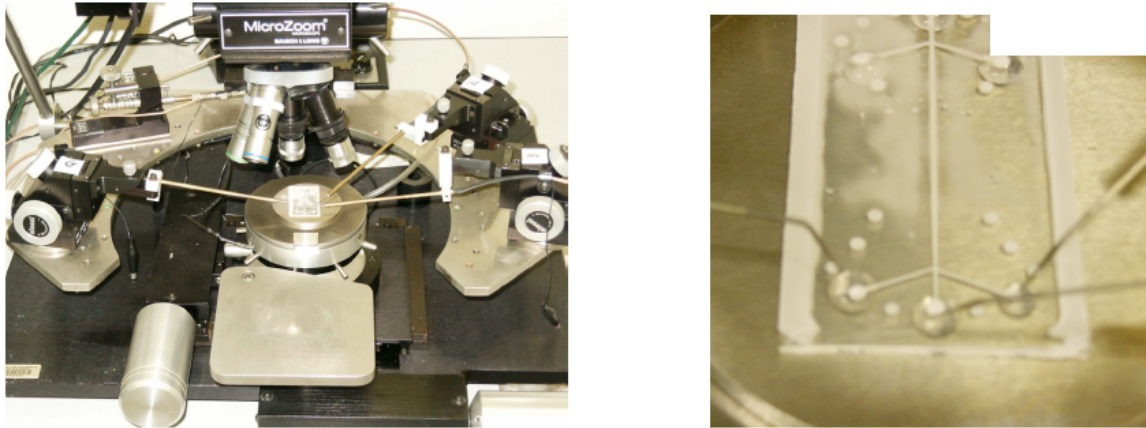


**Figure 80. Probe station.**

On the left is the latest device design undergoing electrical characterization. On the right is a close-up of this device showing probes connected to the vias reservoirs.

#### 4.27 BIP Fabrication

The multi-layer fabrication construct to form the BIP was improved in three main areas: 1) isolation and connection of the vias, 2) electrokinetic flow optimization, and 3) micro-channel fabrication, cf. Fig. 79. At this stage the strategy of bonding a thick PETG cap layer to the device was abandoned, because thermal stresses from the bonding process deformed the polymer layers beneath. A simpler approach in which a double layer of PMMA was bonded to the top of the device was used. This greatly increased the robustness of the device, but has limited the liquid capacity for each via.

As shown in Fig. 80, electrical characterization of the device took place without strict via liquid confinement. The electrokinetic flow within the PMMA channel network was also optimized. Stable and reproducible impedance measurements were achieved within the individual channels, and between the microfluidic channels through the nanofluidic gates. However, impedance measurements changed conductance regimes at higher voltages. Single channel devices, as shown in Figure 81, were made. Straight microfluidic channels were fabricated to more clearly ascertain the effects of adhesive properties, cure schedules, and PMMA formulation on the electrical characterization and performance of the device. The reactive ion etching (RIE) patterning of the channels was optimized.

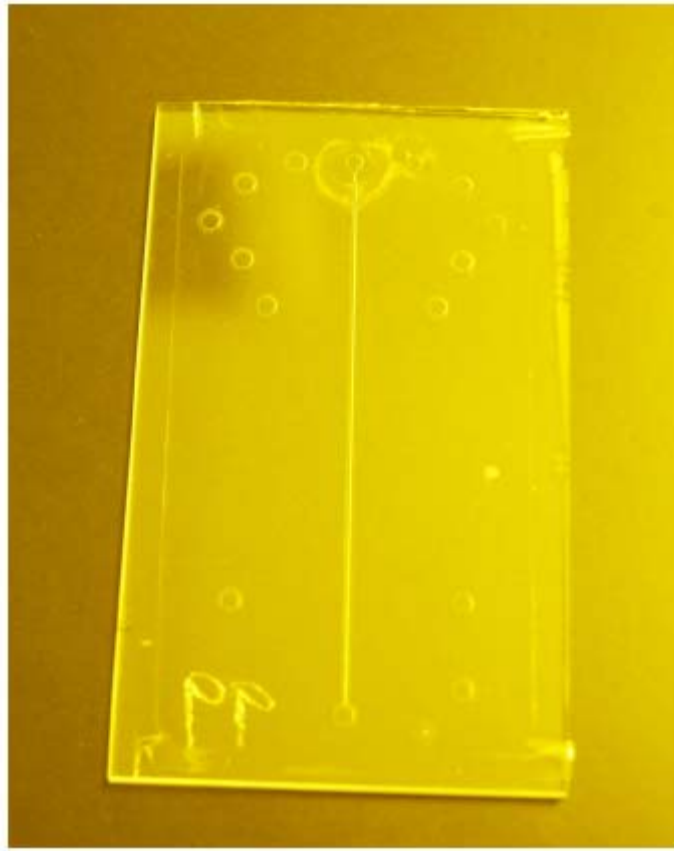


**Figure 81. Straight-channel device.**

Sharp corners and vertical sidewalls were desired. Shown in Table I are some of the optimization parameters of the RIE process. Generally speaking, as more argon was added, the sidewalls become more optimization parameters of the RIE process.

Table I. Reactive Ion Etching Parameter Optimization to Minimize Corner Rolloff and Slope.

<u>Process</u>	<u>Oxygen</u>	<u>Argon</u>	<u>Pressure</u>	<u>Duration</u>	<u>“Corner Rolloff”</u>	<u>Slope</u>
L	1.0	1.0	0.5 Torr	2 hours	0.5 micron	0.20
M	3.0	1.0	0.8 Torr	1 hour	0.7 micron	0.10
N	3.0	-	0.7 Torr	1 hour	1.9 micron	0.17
O	2.5	2.5	1.0 Torr	1 hour	2.8 micron	0.08
P	4.0	0.5	1.0 Torr	1 hour	2.1 micron	0.13
Q	3.5	1.0	1.0 Torr	1 hour	1.0 micron	0.04

Generally speaking, as more argon was added, the sidewalls become more vertical (slope decreases), but the “sharpness” of the corners became worse. An increase in pressure as well as balancing the argon amount led to an improved fabrication process. Additionally the bonding process improved as the microfluidic channels were more geometrically precise.

## 5.0 INTERFACING AND OPERATION

The Biological Intelligent Processor (BIP) diagnostic test station, a laser-induced fluorescence detection system, was constructed and optimized. This was an independent fluorescence microscope test station, which was also designed to be interfaced with a fluorescence microscope. After the BIP diagnostic test station was assembled, prototype devices were tested.

### 5.1 Prototype Testing

A three layer device consisting of two electrophoretic channels with a “molecular valve” molecular gate between the two channels was the first device tested. Testing the device required the appropriate fabrication protocols to be followed, and so a prototype was first tested. The prototype was fabricated by the polydimethylsiloxane (PDMS) rapid prototyping scheme developed by Whitesides [1]. The advantage of utilizing a prototype was that the control systems (computer code and high voltage switches) could be determined for the operating parameters of the molecular gates. Particularly important was that most prior preliminary studies of molecular gates were in the “macro-scale” with milliliter to microliter volumes, which corresponded to slow operational speeds. While simple scaling laws predicted a large increase in the operation speed of a molecular gate when the “reservoirs” were reduced in volume to the picoliter volume regime, this had never been experimentally verified.

Preliminary experiments using a three-layer PDMS device demonstrated a large increase in molecular gate speed and efficiency in stacked three-layer devices. The molecular gate itself was first characterized. The prototype devices used to accomplish this consisted of two PDMS layers with channel patterns (100 to 500- $\mu$ m wide, 30- $\mu$ m deep). A polycarbonate track-etched membrane (PCTE) was inserted between the PDMS layers as the gate before sealing. The membrane and layers were sealed together, and then a PDMS reservoir layer was sealed to the top patterned layer. The typical structure of these devices is shown in Figure 82.

Reservoirs 3 and 4 were connected through the channel in the top layer, while the channel in the bottom layer reservoirs 1 and 2 were connected (Figure 82(b)). The only intersection between the top and the bottom channels was through the PCTE membrane, which had a cross section of 100  $\mu\text{m}$  by 100  $\mu\text{m}$  (up to 500  $\mu\text{m}$  by 500  $\mu\text{m}$  in some of the prototypes), which defined the active gate area. The top channel and reservoirs were filled with the fluorescein containing source solution and the bottom ones with buffer, and then electrical contact was achieved by inserting platinum electrodes into the reservoirs. All molecular gate controls and detection were computerized through the data acquisition interfaces and the multiple-relay system that was constructed in-house specifically for this project.

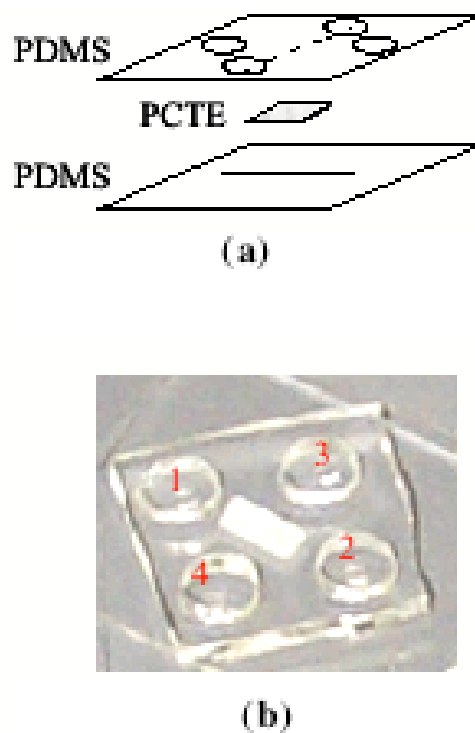


**Figure 82. Illustration of the first prototype crossed channel device.**

(a) Schematic diagram showing the placement and orientation of components. (b) Photograph of one particular device structure. The molecular gate was evident as the white rectangular element in the center.

Figure 83 demonstrates the ability to control transport of the probe molecule (fluorescein) by the application of a voltage bias across the membrane. When a forward bias was applied (bottom reservoirs at +100 V and top at ground), a sharp rise in fluorescence signal was observed, followed by a decrease in signal intensity after the release of the bias. Thus, fluorescein ions were transported from the source side, through the PCTE membrane, and into the bottom channel under the forward bias. This completely cleared the top channel in several seconds. When the bias was removed and the channel voltages floated, diffusion along the bottom channel reduced the fluorescein concentration. Upon application of a reverse bias voltage, the fluorescein ions were depleted from the bottom side of the gate back into the source side, accompanied by the steep drop in signal intensity. When the bias was removed, it took 60 s for the system to relax to the diffusion-controlled equilibrium. The majority of the response generated upon bias application occurred in less than a second, which demonstrated the ability to control the probe transport actively on a fast time-scale.

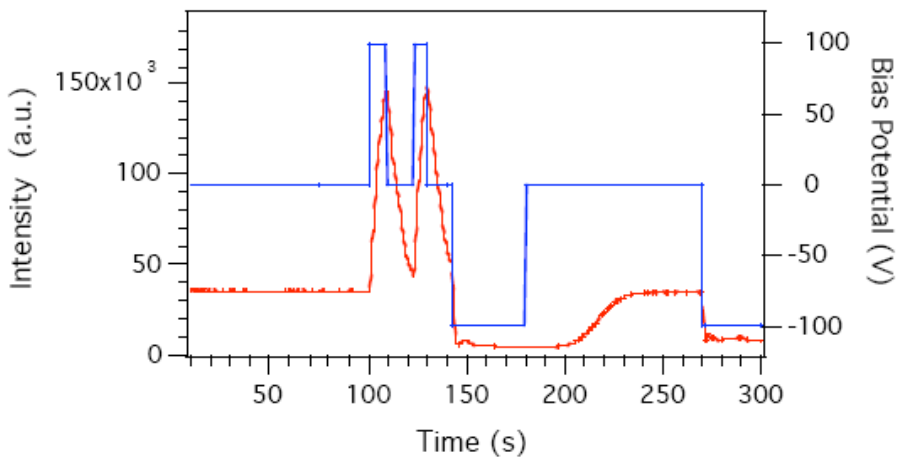


**Figure 83. Plot of the fluorescence response.**

(Red) in the receiving channel in response to the applied bias potential (blue) between source and receiving channels.

The reason that the response continued to increase after the initial step period was that the entire upper channel was filled with probe molecules, and so as more fluorescein molecules diffused and migrated into the space above the gate, those molecules were transported to the lower reservoir. Obviously in the separation experiments, the upper

channel had only a limited “zone” of material to be transported, and so the response reached a limiting value much faster. These results on testing the prototypes for the first generation BIPs were encouraging.

## 5.2 Different Gate Membranes

Next simple three-layer devices were explored with different types of gates (membranes) for elucidation and optimization of the active control of molecular transport. A range of probe molecules, including positive, neutral and other negative molecules of various molecular sizes, were more fully characterized to determine the mechanisms of transport across different molecular gate structures. With such information, device fabrication could be optimized, and guidelines were developed for faster and more efficient molecular gate operation. Using the three-layer polydimethylsiloxane (PDMS) devices, the control and detection systems were optimized, in addition to the further characterization of the molecular gates.

As demonstrated previously, the direction of transport was controlled by tailoring the macro-scale surface properties of membranes, under conditions where nanochannels in the membrane were the major source of electrical resistance in the system. Under these conditions the identity of the mobile counterion in the channels and the ionic strength determined the direction of transport. When the same membranes were incorporated in PDMS devices (Fig. 82), the resistance of the PDMS channels played an important role in determining the net flow direction, because the sign of the mobile counterion was opposite to that obtained in PCTE nanochannels. Hence, a new parameter for microfluidic control was elicited.

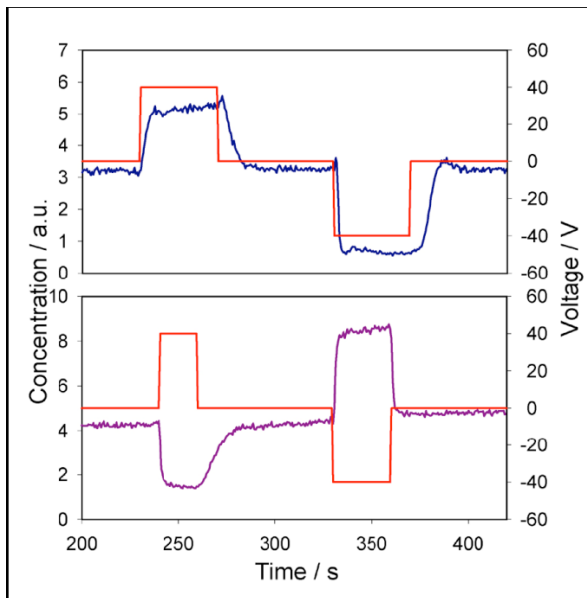


**Figure 84. Fluorescein concentration in the receiving channel.**

Responses to applied voltage (black) between source and receiving channels. (Top, 15-nm PCTE; bottom, 200-nm PCTE). Channels of the PDMS devices were 100- $\mu$ m wide and 30- $\mu$ m deep.

In Figure 84 is contrasted the behavior of 15-nm (top) and 200-nm (bottom) pore size polycarbonate membranes (PCTE) in PDMS devices. The 15-nm pore size device behaved as expected from macro-scale transport experiments, that is, applied positive bias caused electroosmotic transport of fluorescein into the receiving channel. On the other hand, positive bias caused the buffer to flow into the source side in the 200-nm pore size device. This unexpected result was caused by the difference in electric field strength that resulted from the significant variations in resistance ratio of PDMS channels to PCTE membranes. The ratio of resistances was 3:1 in the 15 nm pore size membranes, and 58:1 in the 200-nm pore size membranes.

Thus, in the case of 200-nm pore size PCTE membranes, the membrane resistance constituted of less than 2% of the total resistance, so the electroosmotic flow generated in the PDMS channels overcame the oppositely-oriented electroosmotic flow generated in that membrane. This resulted in a net flow that moved the analyte into the receiving channel under negative bias. Therefore, the direction of flow could be manipulated by varying the channel length used in combination with a single membrane, which resulted in a powerful new design tool with which to tune the nanofluidic behavior of the

structures. A positively charged probe, Rhodamine 560, was used to verify the driving force of the transport, which showed the same behavior as the negatively charged fluorescein. Electroosmosis was the dominant force under these conditions, driving all species (neutral, positive, and negative) in the same direction.

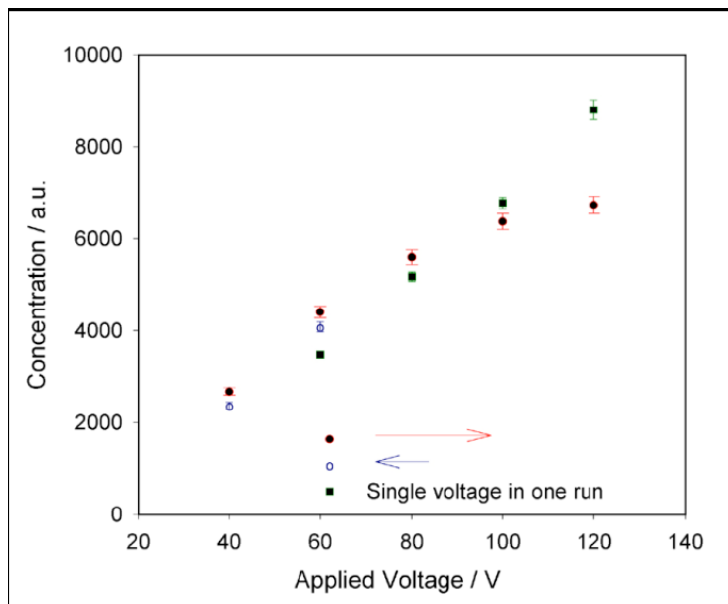


**Figure 85. Fluorescein concentration in the receiving channel in response to applied voltage.**

The data taken in the order of increasing voltage were depicted in red, and open circles were the subsequent measurements in descending voltage. The green squares represent separated runs at single voltages.

The effect of external voltage on transport rate (Figure 85) was investigated. The results from separate runs with single voltages clearly indicated a linear relationship between the transport rate and the driving voltage. Since a threshold and a breakdown voltage were expected in a molecule gate operation, this result served as a guide for operation, and effectively dictated the controllable dynamic range.

Efforts were made to optimize experimental parameters for “gating” coupled with electrophoretic separation. A system that demonstrated separation and retrieval of analyte was implemented, and construction of a dual detection system began. By combining charge-coupled device (CCD) imaging and photomultiplier tube (PMT) detection, molecular movement could be “seen” under the control of molecular gates.

### 5.3 Transport

The manipulation of electric bias control was then focused on to achieve faster and cleaner transport of analytes. Three types of bias configurations for transport were demonstrated, as shown in the insets of Fig. 86, with the three-layer PDMS devices that were developed. The principal construct was a nanofluidic membrane sandwiched between two crossed microfluidic channels. The crossed microfluidic channels spatially defined the transport region and eliminated the need for the precise alignment of the nanofluidic membrane. Transport control was monitored with fluorescence spectroscopy, and fluid streams were characterized by interrogating the fluorescence signal on either the originating or the receiving channel side of the nanofluidic membrane. Fig. 86(a) shows the transfer of an aqueous 5 mM phosphate buffer solution (PBS) at pH = 8 of the anionic fluorophore, fluorescein, across a 200 nm pore diameter polycarbonate PCTE membrane to a receiving channel held under static, *i.e.* flow-free, conditions. Successive transfers were controlled by the application of negative bias pulses. Because the potential of the

receiving channel was held constant the fluorophore concentration determined

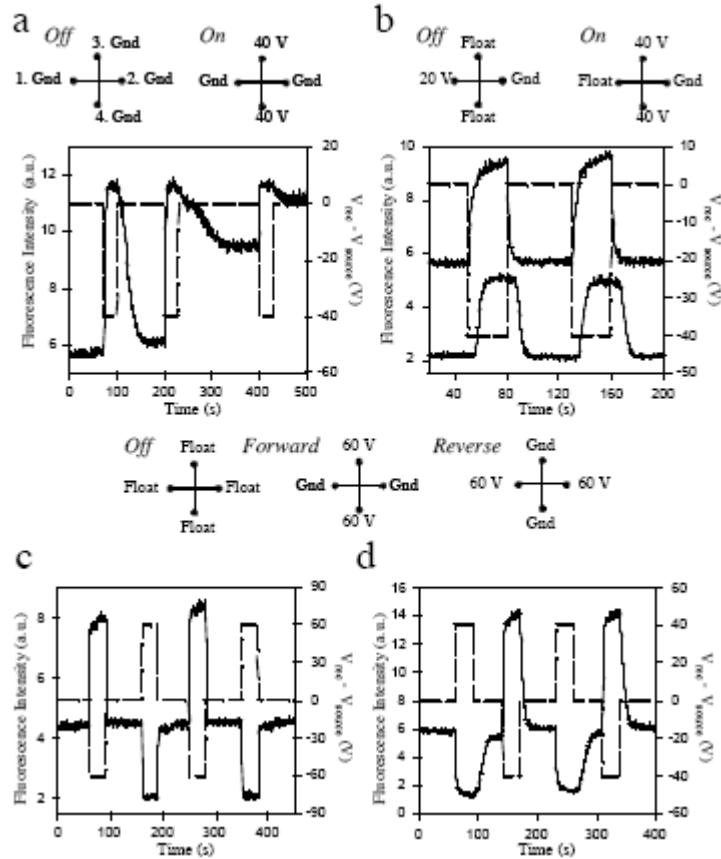


**Figure 86. Fluorescence intensity and applied bias.**

(a)Fluorescence intensity (left ordinate, solid line) and applied bias,  $V_{rec} - V_{source}$ , (right ordinate, dashed line) as a function of time showing transport of fluorescein in PBS across a 200 nm pore diameter PCTE membrane. The inset shows how the bias voltages were applied. Contacts 1 and 2 were in the receiving (horizontal) channel; contacts 3 and 4 were in the source (vertical) channel. The receiving channel was held under flow-free conditions during the off-state in this experiment. (b) Transport across 200 nm pore diameter PCTE detected at (*left*) the membrane and 100  $\mu$ m downstream (*right*) in the receiving channel. (c) Transport across 200 nm pore diameter PCTE. Off-state, reverse bias, and forward bias potentials were shown in the inset. (d) Neutral probe migration. Fluorescence intensity and applied bias as a function of time to monitor the transport of bodipy fluorophore in PBS across 200 nm pore diameter PCTE.

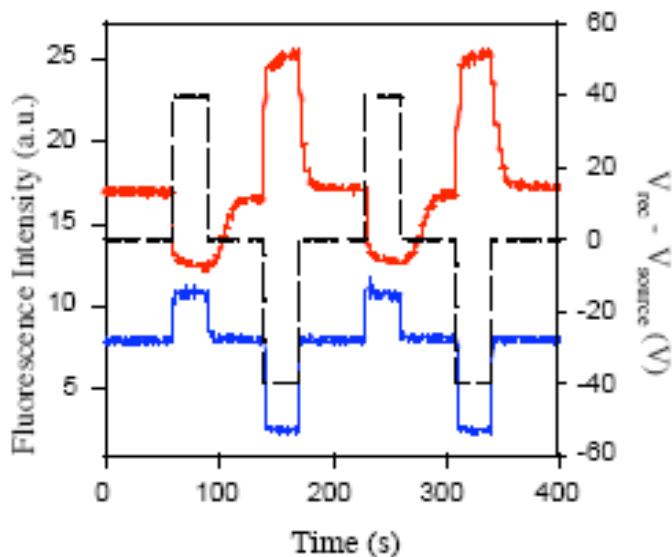
during bias application was a balance between active transport from the source channel and diffusion along the receiving channel. When the bias was removed, diffusion depleted the concentration in the region probed. With successive forward bias applications the concentration of probe in the receiving channel increased, thereby reducing the driving force for diffusion after subsequent transfers.

Fig. 86(b) shows the results of a similar experiment in which active flow was maintained in the receiving channel. The build-up to steady-state at the membrane after bias

application resulted from the balance between active transport of the analyte across the nanofluidic membrane and its removal by cross-flow in the receiving channel, which was clearly more gradual than under static conditions. A time offset was observed when the detection region was moved downstream of the interconnect.

Figure 86(c) demonstrates the level of control and speed of transfer possible with these nanofluidic interconnects. In this experiment the off-state voltages were allowed to float, producing a non-zero level of transfer at the intermediate between the forward-bias (-60 V) on-state and the reverse-bias (+ 60 V) on-state. Measurements on the changing edges of Fig. 86(c) indicated that a steady state concentration was re-established in the receiver channel within 1.2 s of the application of the switching voltage.

Figure 86(d) demonstrates the insensitivity to the charge state by comparing the transfer of the neutral fluorophore, 4,4-difluoro-5,7-dimethyl-4-bora-3a,4a-diaza-*s* indacene-3-succinimidylpropionate (bodipy). The surfaces of the PCTE membrane channels were coated with polyvinylpyrrolidone (PVP) to render the surfaces hydrophilic. The tertiary amine of the PVP was susceptible to protonation, making the surfaces net positive at pH 8, and resulted in the diffusion of the negative counterions to the interior of the nanochannels. Under these low ionic strength conditions, the ionic population in the channel was predominantly  $\text{H}_2\text{PO}_4^-/\text{HPO}_4^{2-}$ , and the forward bias obtained would be  $V_{rec} - V_{source} > 0$ , if the nanofluidic channels controlled the direction of transport. Instead, flow in the direction predicated on the (negative) charge state of the PDMS surfaces of the microfluidic channels controlled transport.



**Figure 87. Transport of BODIPY in 15 and 200-nm pore size membrane PCTE microchips.**

This control could be reversed, as shown in Fig. 87, for transport across a 200 nm pore diameter membrane compared with that across a 15 nm pore diameter membrane. Clearly the polarities of forward- and reverse biases were reversed. This behavior was based on two effects – the greatly increased resistance to pressure driven flow through the smaller pores and the greater voltage drop across the pores in the 15 nm case. Modeling the impedance network composed of the two microfluidic channels and the membrane showed that in the network containing the 200 nm pore membrane, less than 2% of the potential was dropped across the nanofluidic membrane. However, for 15 nm pores, just over 33% of the potential appeared across the membrane. The PCTE pore electroosmotic flow dominated when 15 nm pores were used, but not when larger pores were employed. Thus, by choosing the pore size, pore and channel surface chemistries, and solution composition, either direction of fluid flow can be chosen for the same externally applied voltages. Furthermore, these results with a neutral dye in both 15 (bottom) and 200-nm (top) PCTE chips supported the previous conclusion that electroosmosis was the ultimate driving force in these structures.

## 5.4 Transport Behavior by Fluorescence Imaging

The transport phenomena in 3-dimensional microfluidic/nanofluidic composite structures was investigated by fluorescence microscopy and spot-detection laser-induced fluorescence (LIF). Figure 88 shows a series of images observed under bias with time. Resistance differences between the two sides of the receiving channel in a 200-nm pore size PCTE device were caused by either slight differences in the channel lengths and/or in the electrolyte concentrations. The probes (fluorescein<sup>2-</sup>) were moved from the source channel into one side of the receiving channel when both receiving reservoirs were under the same bias (Fig. 88a, top). This preferential transport could have been overcome by increasing the magnitude of the bias, as fluorescein<sup>2-</sup> moved into both sides of the receiving channel from the source channel when the bias increased from -40 to -160 V (Fig. 88a, bottom).

In all conditions studied with the 200-nm pore size PCTE, the response of the fluorescence intensity upon the bias was always observed as soon as the bias was turned on, suggesting that it would be feasible to transport a narrow analyte band from one channel to the other with a short bias pulse. This concept was investigated further with a new multichannel design. The fluorescence image of fluorescein transport was difficult to observe with 15-nm pore size PCTE, since the overall transport efficiency was small. However, an increase of fluorescence intensity in the source channel was observed under bias (Fig. 88b), indicating sample stacking upon the application of a bias. There are numerous situations in microfluidic manipulation in which sample stacking is desirable, so this observation was significant.

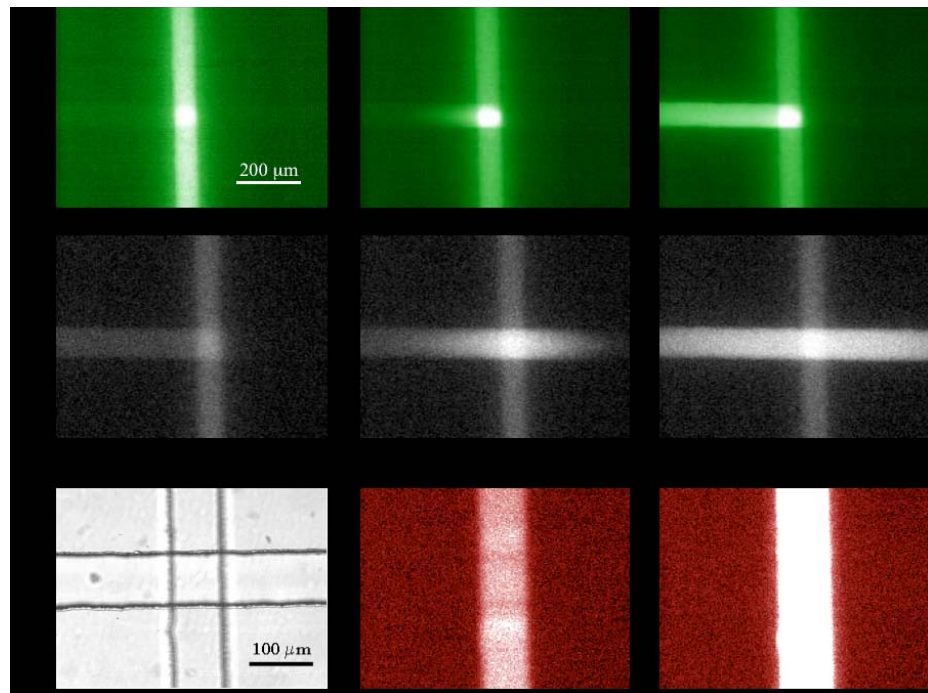


**Figure 88. Fluorescence images vs. time.**

(a) Fluorescence images vs. time with a 200-nm pore size PDMS/PCTE/PDMS device — top row:  $V_{rec} - V_{source} = -40$  V; bottom row:  $V_{rec} - V_{source} = -160$  V. (b) Left, white light image of the cross section of a PDMS device with 15-nm pore size PCTE; middle, fluorescence image of the same area under zero bias; right, fluorescence image at  $V_{rec} - V_{source} = 120$  V. In both (a) and (b) the source (vertical) channel was filled with 1  $\mu$ M  $Fl^2+$  in 5 mM PBS, and the horizontal receiving channel was filled with 5 mM PBS at pH 8.

### 5.5 Stacking Effect of the Membrane

The sample stacking phenomenon observed in Fig. 88b was studied further. With single spot LIF detection 200  $\mu$ m from the intersection in the *source* channel, a detectable change in the fluorescence intensity was not observed upon the application of bias in the 200-nm pore size PCTE device. On the other hand, the intensity (i.e. fluorescein concentration) increased 3-fold under the same conditions in a 15-nm pore PCTE device (Fig. 89). The size of fluorescein ion was 8% of the 15-nm pore size, and a similar sample stacking effect was expected when the diameter of the nanopores was within one order of the hydrodynamic radius of the analyte. Therefore, integration of small pore diameter gates into microfluidic systems will provide a means to pre-concentrate dilute analytes, which will result in either increased detection volume sensitivities and/or further reduce the dilution effects in the analysis.

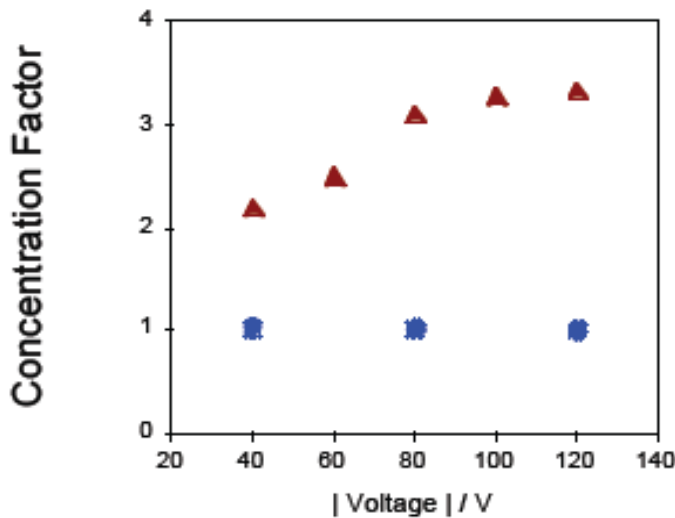


**Figure 89. Sample stacking in the source channel vs. absolute bias.**

The PDMS/PCTE/PDMS devices with 15-nm pore size (red) and 200-nm pore size (blue) PCTE membranes.

## 5.6 Interfacing and Characterization of the First Generation BIP

With the previously reported rapid prototyping method, double cross polydimethylsiloxane (PDMS) devices were fabricated, as shown in Fig. 90, to explore how nanoporous membranes could be gated to inject samples and collect analytes in chip-based separations. An additional channel was added to the original cross channel system, yielding two parallel channels,  $p_1$  and  $p_2$ , that were 425  $\mu\text{m}$  apart and intersected a cross-channel,  $c$ . Initially  $p_1$  was filled with fluorescein, and the remaining channels with buffer.

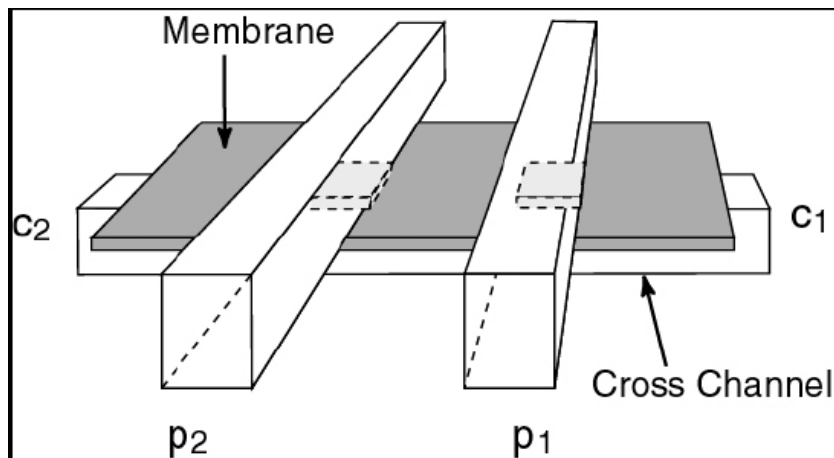


**Figure 90. Schematic diagram of an injection/collection system.**

Fig. 91 shows a sequence of fluorescence images from injection to collection of the 1<sup>st</sup> generation BIP. After injection the fluorescein solution was electrokinetically transported from p<sub>1</sub> into the cross channel, Fig. 91(a), and then the electrical configuration was switched to move the fluorescein band along the cross channel, Fig. 91(b). Knowing the velocity in the cross channel and the injection time allowed timing the forward bias of the c-p<sub>2</sub> junction, and the band moved vertically into channel p<sub>2</sub> (Fig. 91(c)). After reverting to reverse bias conditions, a slow broadening of the captured band was observed at p<sub>2</sub> due to diffusion. The entire sequence of micrographs spanned 12 sec. Selective transport of a single band out of multiple repeated injections was achieved in the same fashion, assuring that the type of preparative manipulations envisioned for the final operating device could be realized.

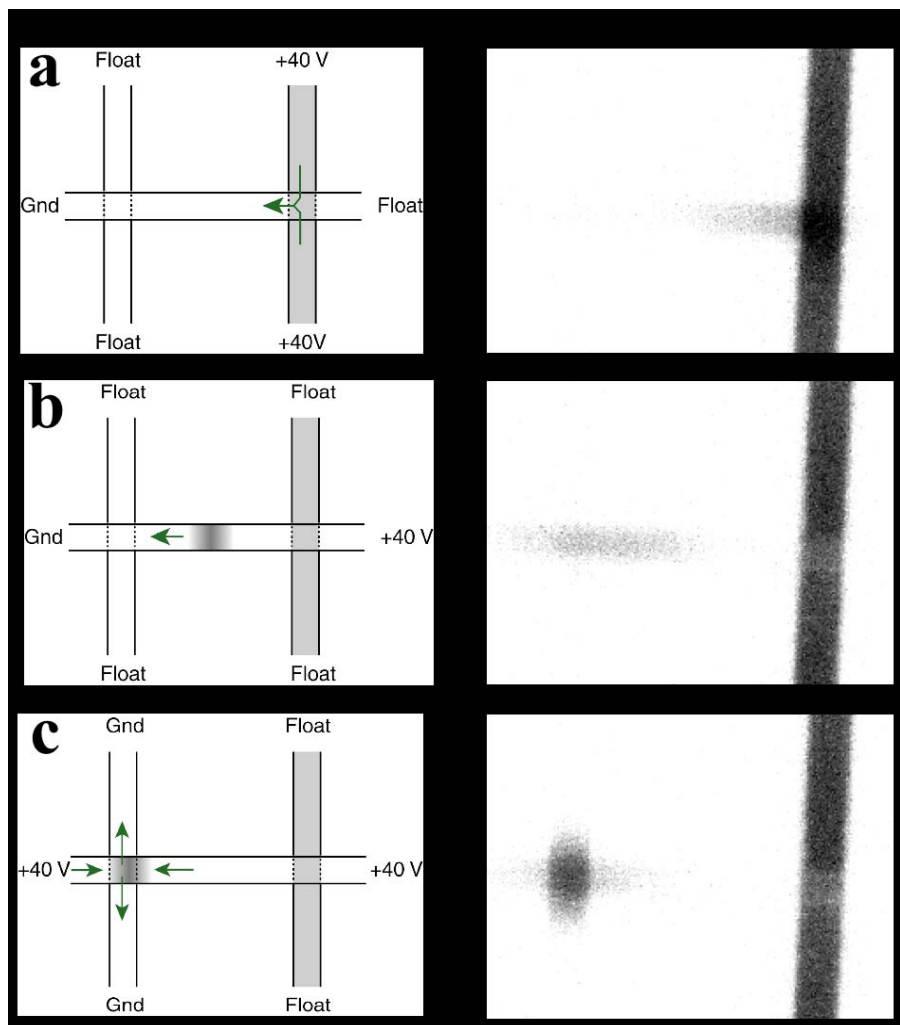


**Figure 91. Injection and collection of an analyte band.**

*Left*, the electrical configuration; *right*, fluorescence images with respect to the electrical configurations. Channel  $p_1$  was filled with  $2 \mu\text{M}$  fluorescein $^{2-}$  in 5 mM PB at pH 9, and the channels  $c$  and  $p_2$  were initially filled with 5 mM PB at pH 9. (a) Injection. (b) Movement of the injected band in the cross channel. (c) Collection of the fluorescein band.

## 5.7 Optimization of the Operation in the Second Generation Prototype BIP's

To optimize the operation of the molecular gates in a BIP, a dual-point detection system was required that allowed the source and receiving channels to be simultaneously monitored. A second generation BIP diagnostic station was constructed to monitor fluid transport and electrophoretic transfer of fluorescent probe-containing streams. The advantages over previous diagnostic stations based upon single point detection included:

- The ability to monitor source and receiving sides of molecular gates simultaneously during transport studies.
- The ability to study the capacity of molecular gates to collect individual chromatographic bands selectively among closely spaced bands.
- The ability to monitor chromatographic bands simultaneously at points proceeding and following the molecular gates to evaluate the efficiency as collection devices; a capability required to optimize gating speed and collection efficiency.
- The ability to use the signal from a detection point just prior to molecular gates as a trigger signal for collection.

Figure 92 shows a schematic representation of the dual point detection system. The important features of this system included an additional detector (vertical), with associated collection optics, mounted on a translational stage. A pinhole was placed in front of each detector to reject both stray light and some out of focus sample fluorescence. In addition, the sample could be translated in all three Cartesian directions to allow reproducible optical sampling from addressed physical locations. As a result, molecular transport and separation/collection experiments could be performed with a variety of detection schemes, as illustrated in Fig. 93. Modes 1&2 were appropriate for monitoring source (open circle) and receiving (closed circle) sides of molecular gates during transport studies, and Modes 3-5 allowed the optimization of the timing and duration of gating to efficiently collect chromatographic bands. Finally, Mode 5 was used to optimize gating procedures to collect a single band among closely spaced bands.

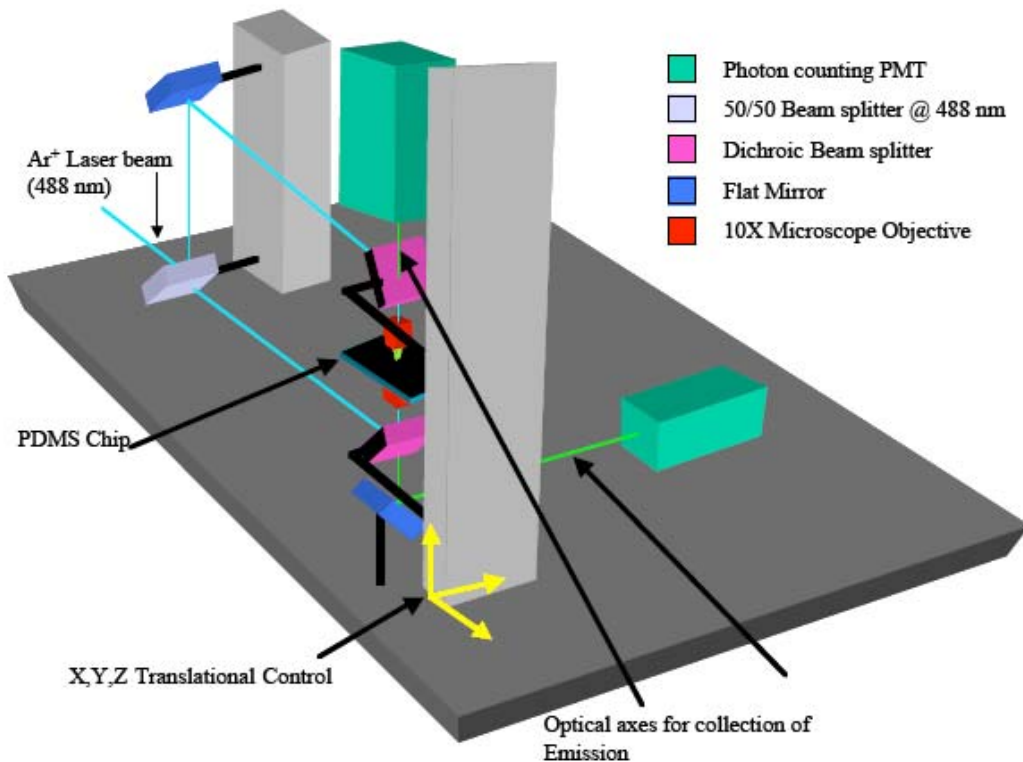


**Figure 92. Diagnostic station with dual detection capabilities.**

Both source and receiving channels are monitored.

### 5.8 Automated Sample Injections.

The dual-point BIP diagnostic station was applied to evaluate the ability to generate and to detect a series of automated injections of a solution of fluorescein. This ability was necessary to simulate closely spaced chromatographic bands to be isolated upon encountering molecular gates that serve as collection devices. The ability of molecular gates to inject (*see below*), transport, and recapture solutions of fluorescein within

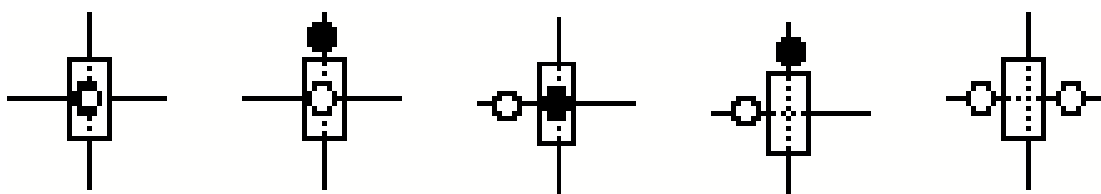


**Figure 93. Modes of operation of the dual point detection.**

microfluidic structures was evaluated. However, each of these manipulations had, up to this point, been accomplished by active user control. The final operating BIP's required the automation of sample injection, separation, and collection. Automated collection of chromatographic bands was inherently more complex, since this required the ability to control the application of a potential bias across membranes in the presence of a desired analyte.

Potentially one of two strategies, or a combination of the two strategies, could be used in timing gates for collection:

- The electrokinetic velocity of the target analyte and the distance between the collection injection gates could be used to determine the time for collection.
- A detection point placed immediately before the collection gate could be used to trigger collection.

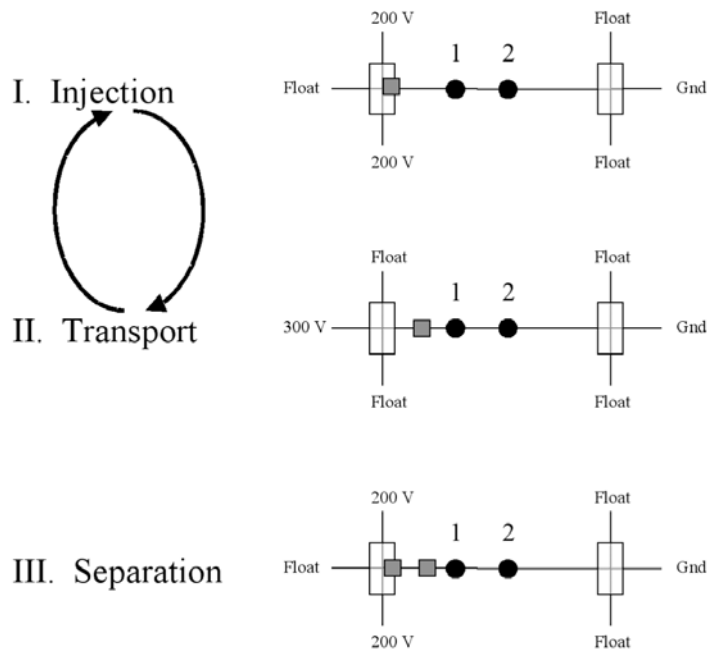
Evaluation of any automated gating strategy required a series of fluorescein “bands” of reproducible spacing to be introduced to collection gates. Table II shows preliminary data that illustrates the automation sample injections and separations.

Table II. Injection and Separation Parameters for Automated Triplicate Injections of 5 $\mu$ M Fluorescein in 5mM Phosphate Buffer (pH=7.7).

Trail	Detection Point #1			Detection Point #2		
	Transport Time ( $t_1$ ) (sec)			Transport Time ( $t_2$ ) (sec)		
	Peak 1	Peak 2	Peak 3	Peak 1	Peak 2	Peak 3
A	14.2	23.7	33.8	30.7	38.8	48.8
B	12.6	23.1	32.8	29.1	38.6	48.9
C	12.1	22.7	32.6	28.5	38.3	48.6
	Peak Period 9.9 $\pm$ 0.6 sec			Time Delay(s) 15.9 $\pm$ 0.5 sec		

Injections were 1 second in duration with a frequency of 0.1 Hz. Uncertainties were reported at the 95% confidence level. Data in Table II were acquired using Labview® software, which also was used to apply voltages to chips according to the scheme shown in Figure 94. Steps I and II were repeated to yield the desired number of injections. The duration of steps I and II controlled the injection duration and frequency, respectively,

while the duration of step III was controlled to ensure that all injections passed detection points 1 and 2 (closed circles).



**Figure 94. Schematic showing voltage sequence used for automated injections of fluorescein.**

Fluorescein “bands” were represented by grey squares while detection points were shown as black circles. Injection and Separation gates (200nm pore size PCTE membranes)are shown on the left and right, respectively.

### 5.9 Molecular Gates as Injectors

Quantitative transport studies of large molecular weight dextrans had shown excellent reproducibility, leading to the development of molecular gate sample injectors. Non-optimized initial studies had demonstrated injection reproducibilities of  $\pm 10\%$  for 2 MDa of dextran across a 200-nm pore diameter membrane. Further refinement reduced the variance to  $\pm 4\%$  for 2-sec injections, and  $\pm 5\%$  for 10-sec injections. With appropriate care, the reproducibility for fluorescein injection across a 100-nm membrane was lowered to  $\pm 2\%$  for 1-sec injections (Figure 95).

Further refinements of the inherent injection variance associated with these gates could be achieved with computerized injection timing schemes (data presented here were manually timed), faster sampling rates (just 3 Hertz (Hz) in these studies), as well as faster switching electronics (current HV-relays have response times in millisecond time

range versus achievable nanosecond and even picosecond HV switching times) were anticipated. In addition, previous studies had targeted the various (i.e. 200-nm, 100-nm, and 15-nm) pore-diameter membranes for a wide variety of injector applications.

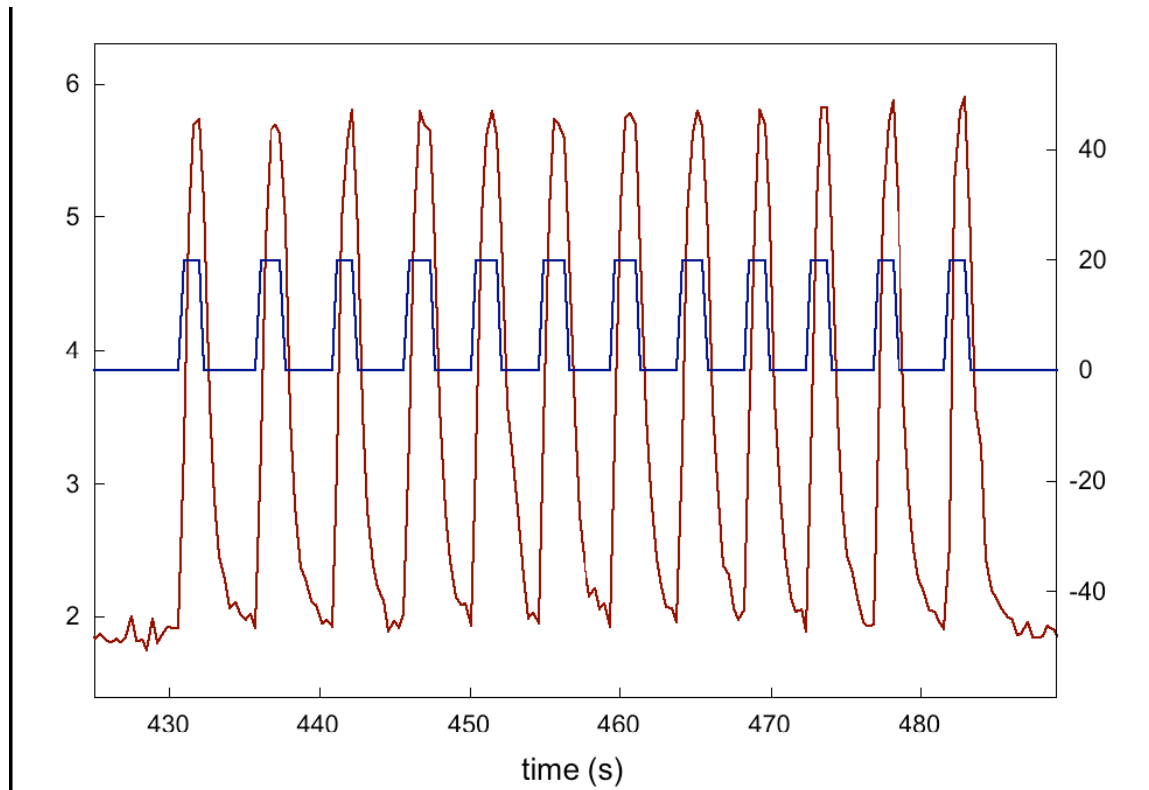


**Figure 95. Gates as Injectors.**

Fluorescence intensity and applied bias as a function of time for fluorescein transport across a 100-nm pore diameter membrane.

Analogous to the collection function, the 200-nm pore diameter gates were used for mass-independent injections. For small molecule transport, all of the pore-diameter membranes showed an excellent ability to be used as reproducible injectors. Furthermore, smaller pore diameter membranes may be used to achieve a “pre-separation” injection by being able to discriminate based on molecular size. Because of the inherent problems with standard microfluidic injection protocols, considerable interest in the injection function of these molecular gates was generated. Further developments related to the injector function were pursued, as well as evaluations of the effects on the resulting separations.

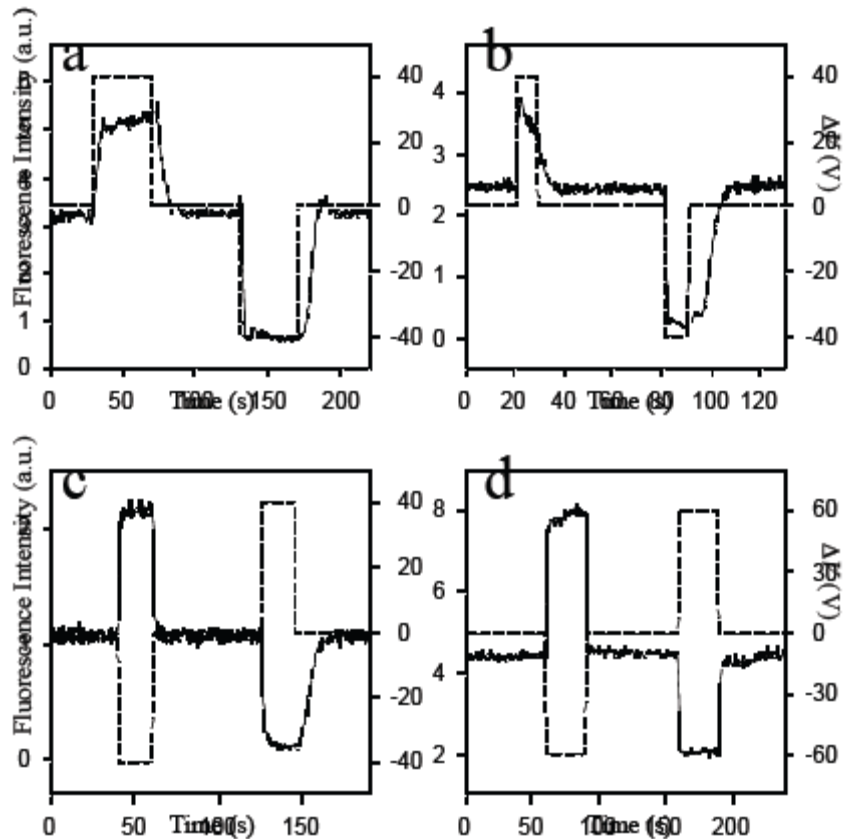


**Figure 96. Fluorescence intensity in the receiving channel.**

Fluorescence intensity (left ordinate, solid line) and applied bias  $\Delta V$ , ( $V_{rec} - V_{source}$ , right ordinate, dashed line), as a function of time in the receiving channel, which showed transport of  $0.17 \mu\text{M}$  fluorescein in  $5 \text{ mM}$  pH 8 PB across the PCTE membranes with various pore diameters: (a)  $15 \text{ nm}$ , (b)  $30 \text{ nm}$ , (c)  $100 \text{ nm}$ , (d)  $200 \text{ nm}$ .

### 5.10 Composite Device Structures

When membranes with different pore sizes were integrated with the PDMS transport devices and forward biased, the  $\text{Fl}^{2-}$  containing solutions were transferred from the source channels to the receiving channels. The potential was positive for the  $15 \text{ nm}$  and  $30 \text{ nm}$  pore diameter PCTE membranes (Figs. 96(a) and (b)), and negative for the  $100$  and  $200 \text{ nm}$  membranes (Figs. 96(c) and (d)). The PDMS microchannels determined the net

device direction of electroosmotic flow in the larger pore diameter structures, while the PCTE nanochannels were controlling for the smaller pore diameters. Table III summarizes the electrical properties of these devices. For those situations in which  $E_m/E_{PDMS}$  was large, either direction of flow could be selected for a particular bias condition by changing the polarity of the nanochannel surface charge (by changing membrane surface chemical functionalities), the pH, or the ionic strength of the buffer solution.

Table III. Impedances and Electric Field Strengths in 3-D Microfluidic Systems

Pore size	Measured resistance ratio <sup>a</sup> $R_m/R_{total}$ (%)	Electric field strength ratio <sup>b</sup> $E_m/E_{PDMS}$	Forward bias <sup>c</sup>	Expected resistance ratio <sup>d</sup> $R_m/R_{total}$ (%)
15	25	670	Positive	36
30	23	600	Positive	12
50 <sup>e</sup>	12	160	Positive	7
100	3	37	Negative	3
200	1.7	20	Negative	1

a.  $R_m/R_{total}$  was the resistance of the PCTE membrane ( $R_m$ ) over the total resistance of the network ( $R_{total}$ ). In these measurements, the buffer was 5 mM PB.

b.  $E_m/E_{PDMS}$  was the ratio of the electric field strength in the PCTE membrane ( $E_m$ ) to that in the PDMS microchannels ( $E_{PDMS}$ ). The pore lengths were from manufacturer's data.

c. The bias, which causes an increase of fluorescent intensity in the receiving channel, was defined as forward bias, and the opposite situation was defined as reverse bias.

d. Calculations were based on lengths and pore densities provided by the manufacturer.

e. For 50-nm pore diameter PCTE membranes, complicated changes in fluorescent intensity were observed. Nevertheless, the polarity of forward bias was clearly positive.

### 5.11 Molecular Gates as Injectors

Analogous to the collection function, 200-nm pore diameter gates were used to achieve mass-independent injections. These gates had extremely good reproducibility for general

transport. For small molecule transport, all of the pore-diameter membranes showed an excellent ability to be used as reproducible injectors. The smaller pore diameter membranes were also used for a mass-biased injection, since these pores preferentially transported smaller molecules, and thus discriminated based on molecular size. Each of the different pore-diameter molecular gates had shown the ability for long repeated use at the appropriate bias potentials.

To accomplish gated injection, the gate region was placed at the front end of the separation channel (Figure 97). In this configuration, the injection gate was placed in the

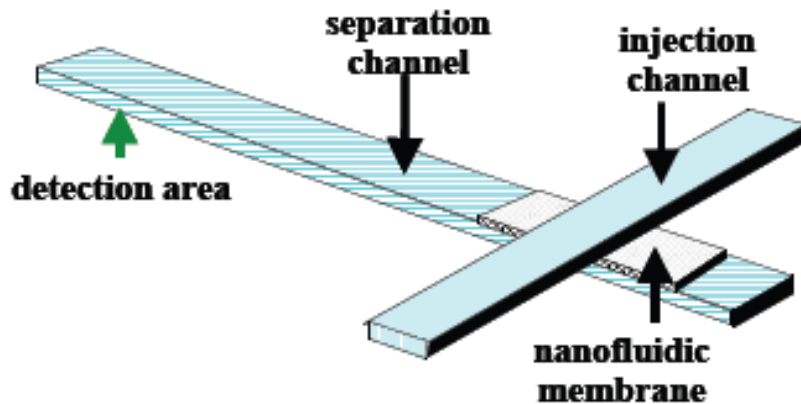


**Figure 97. Schematic of molecular gate injection device.**

position of the cross-T in the more traditional two-dimensional injection scheme. The sample was discretely introduced from the injection channel, crossed the nanoporous gate membrane, and flowed into the separation channel. The injection step was then rapidly followed by flow induction in the separation channel to carry out the separation.

The bias scheme of the system for both injection and collection are shown in Figure 98. For normal fluid flow in the separation channel, a high voltage was applied between the

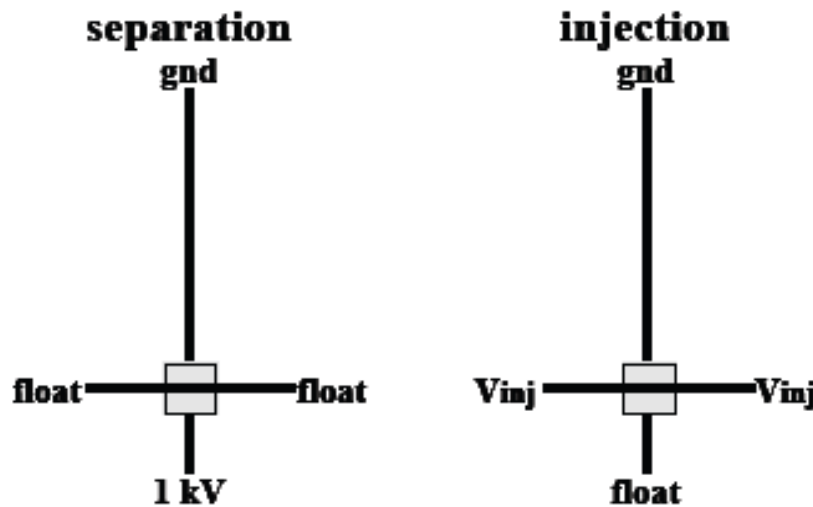


**Figure 98. Potential bias application for both injection and separation schemes.**

two ends of the separation channel, with the voltages for the injection channel being allowed to float. This scheme achieved electroosmotic flow in the separation channel, while not allowing leakage of the analyte across the nanoporous gate membrane from the injection channel. To invoke an injection, the voltage scheme was switched such that the arms of the injection channels were equally biased with respect to the end of the separation channel. For these initial experiments, the injection and separation voltages were the same, which was simply as a matter of convenience.

To demonstrate the utility that these molecular gates have as injectors for microchip-based separations, various gate parameters were varied while monitoring the resulting separation of two FITC-labeled amino acids. Initial experiments were conducted on a fluorescence microscope to evaluate the gating region. The photograph in Figure 99 captured an injection band as it was introduced into the injection channel. Video capturing (data not shown) showed this process to be very reproducible, very robust

(devices allowed to inject continuously over 100 times), and a function of gating time and potential.

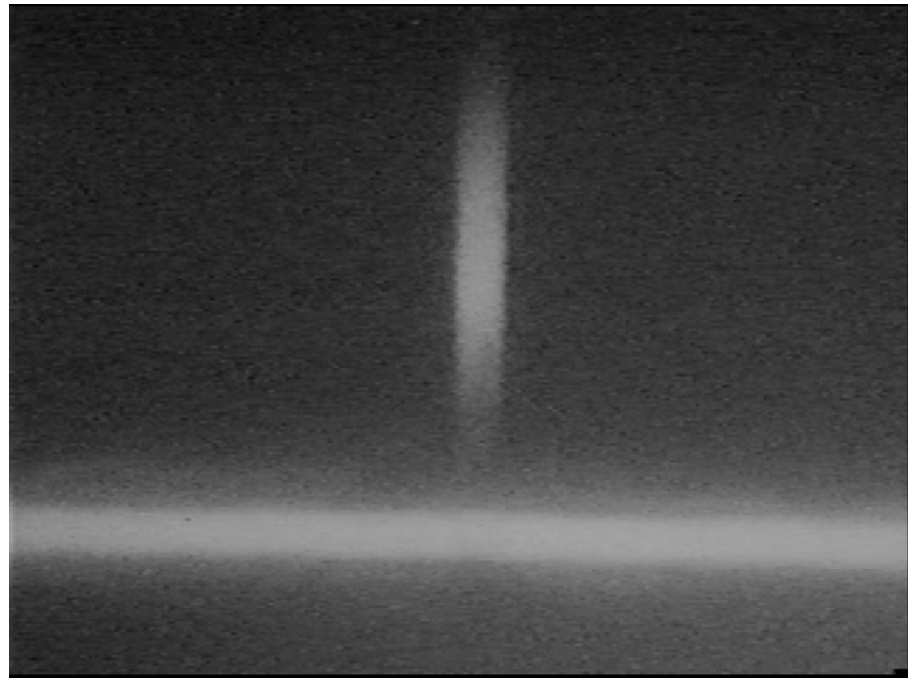


**Figure 99. Fluorescence image of gated injected analyte (FITC-labeled arginine) band across 200-nm PCTE membrane.**

The square plug profile was characteristic of band transport caused by electroosmotic flow (vs. pressure-induced flow). The success of this injection configuration with respect to separations can be seen in the reproducible electropherograms obtained (Figure 100) for the separation of labeled arginine and tryptophan. Furthermore, the efficiency of the system was noteworthy in that a nominal 3 kV separation potential resulted in these two species being separated in less than 1 minute. Also of note were the successive injections that can be accomplished on a rapid time scale. In cross-T injection schemes, a back flow into the injection channel was typically necessary to prevent leakage into the separation channel. The need to “pinch” back the injection meant that successive injections must be performed after the complete separation and detection of the previous run. However, for

the gated injections studied here the time between injections had to be only as large as the time between eluted peaks.

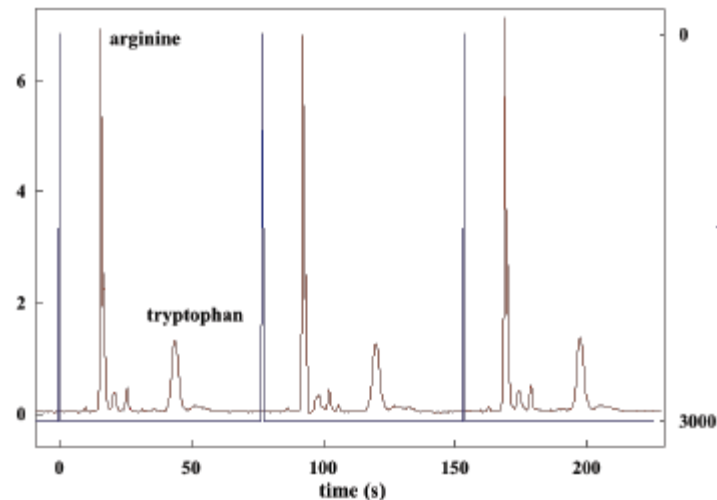


**Figure 100. Reproducibility of the separation of  $\mu\text{M}$  FITC-labeled arginine and tryptophan in phosphate buffer.**

$V_{\text{inj}}$  and  $V_{\text{sep}} = 3 \text{ kV}$ . Detection 20 nm from injection area.

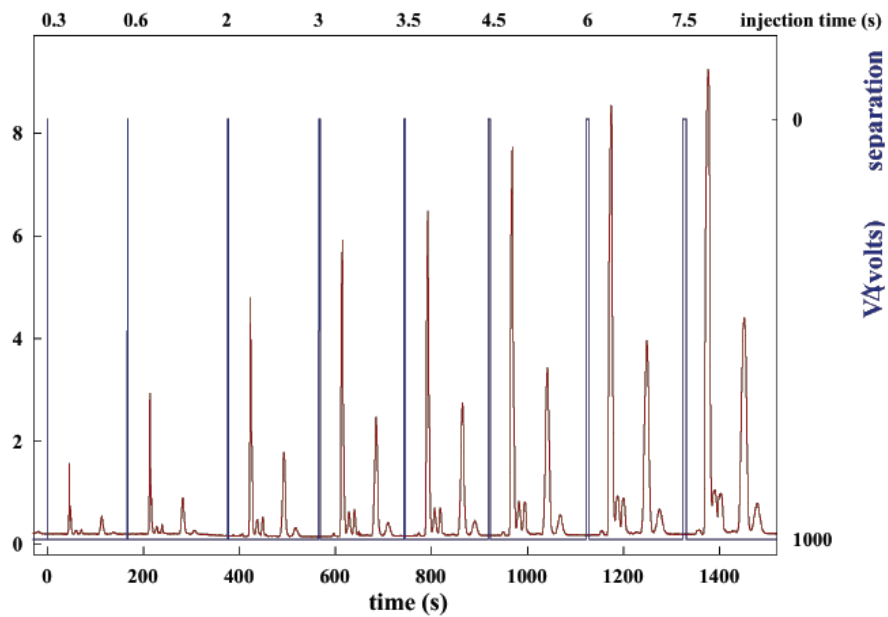


**Figure 101. Separation of  $\mu\text{M}$  FITC-labeled arginine and tryptophan in phosphate buffer as a function of the gate injection time.**

Further experiments focused on investigating how the separations vary as a function of time and injection bias. As expected for gated injections, not only did potential (data not shown) have an effect on the amount injected, but time was also a determining factor. Figure 101 shows a series of separations as a function of gated injection time. This was a unique aspect of gated injections in that the amount injected had a direct result on the separation outcome in the form of detection limits as well as resolution. The linear correspondence between injection time and peak heights showed the versatility of this system to tailor the injection parameters to best optimize the separation. For example, if resolution were of prime importance, a minimized injection time could be used so as not to overload the separation channel, thereby allowing the resolution of two closely eluting peaks. On the other hand, if sensitivity were of importance, injection times would be lengthened to introduce more analyte into the channel increasing the chance of distinguishing above the baseline. This interplay of parameters must be understood for the effective exploitation of this versatile attribute of membrane gated injection.

Because of the inherent problems with standard microfluidic injection protocols, considerable interest in the injection function of these molecular gates was generated, and further developments related to the injector function were pursued. It has not escaped notice that the reproducible injection function demonstrated here could have applications to quite different types of militarily-relevant biomedical problems, such as the controlled delivery of therapeutic agents without need for intervention by medical personnel.

## 5.12 Band Collection

Band collection, *i.e.* the upstream detection and subsequent collection of individual separated bands from a separation, would represent a major milestone for the operation of the integrated BIP concept. In the target device an externally controlled interconnect, or molecular gate, achieved selective removal of specific bands after electrophoretic separation. During operation, an analyte first undergoes electrophoresis in the separation channel, and then either flows past, or flows through, the nanopore membrane into the collection channel. The presence of fluorescently-labeled bands was monitored at two positions (Figure 102). An upstream LIF experiment detected the presence of an analyte

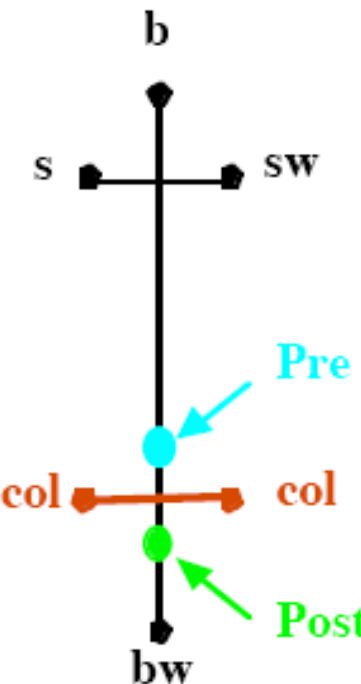


**Figure 102. Schematic of the separation channel and the two LIF detection regions.**

band. The electrophoretic velocity was calculated for each band, and if the velocity matched the velocity of the desired component, then a predicted arrival time at the collection gate was calculated. At the appropriate time the collection gate was forward biased so as to direct the target molecules to migrate through the gate membrane, and into the collection channel. Further manipulation of the isolated molecules in the collection channel then becomes feasible. During an analytical separation, individual component peaks would be observed in both detection windows. However, in the preparative mode, when the collection was turned on, the desired peak was detected in the pre-gate region, but then was transported through the gate and was not detected in the post-gate detection region. To demonstrate the approach, a complex mixture consisting of four amino acids and a degradation product was separated, and each individual band was collected in consecutive runs (Figure 103). 10  $\mu$ M each of FITC-labeled Glu, Gln, Gly and Arg in 10

mM borate buffer eluted with the order of Glu, Gln, Gly, Arg, and Arg-deg. The collection of all five individual peaks was realized from this mixture.

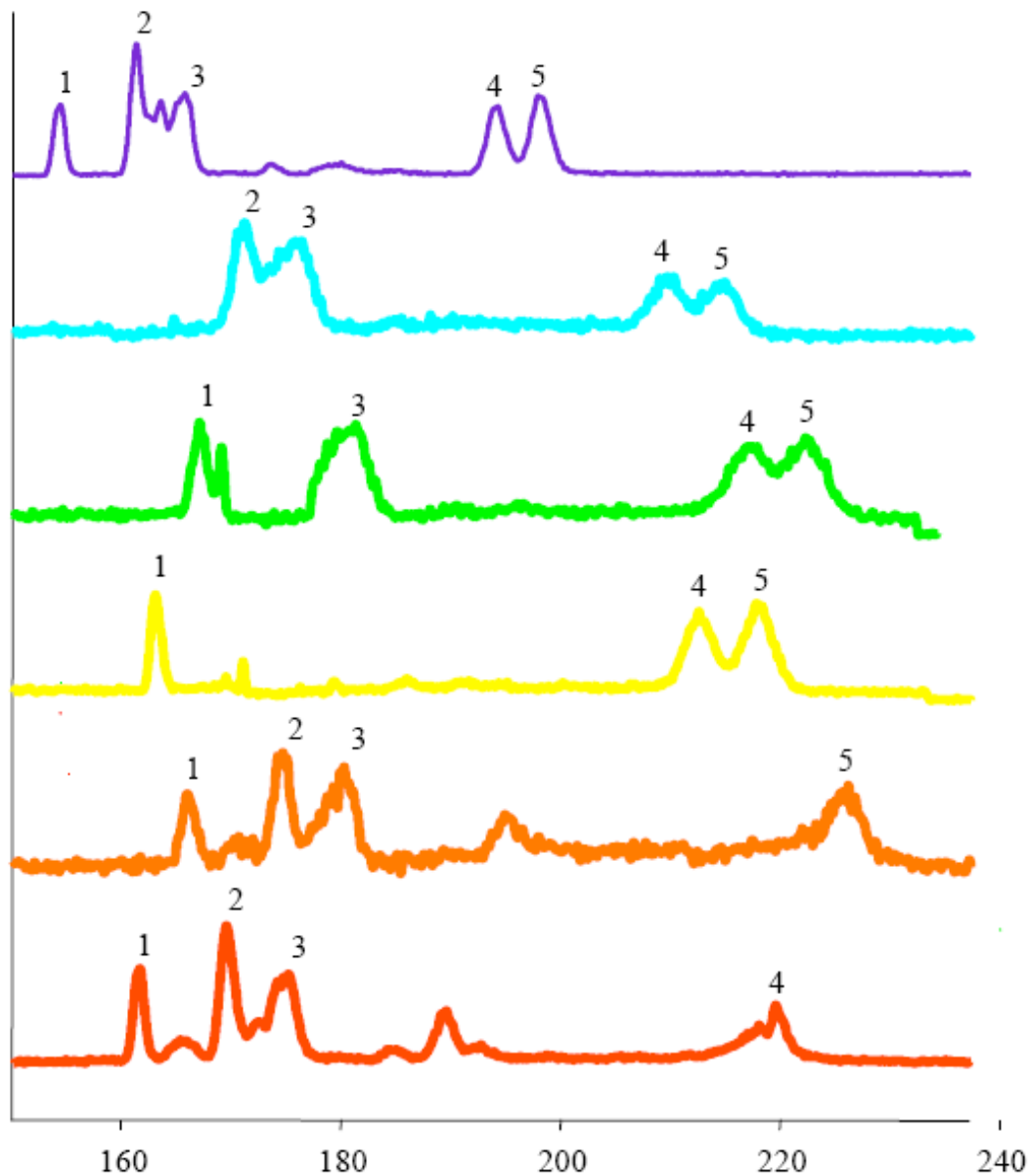


**Figure 103. All five bands of the post-collection volume.**

Below were consecutive separations in which each band was collected, and therefore notched out of the post-collection detection.

### 5.13 Automated Collection of Chromatographic Bands

A computer controlled detection method was developed that, following an electrophoretic separation, recognized the presence of analytes as each passed a specified detection point upstream of the collection gate. When a chromatographic band of interest was detected, this signal was used to trigger the operation of a molecular gate to capture the analyte band. The detection point was placed at a controlled distance preceding the molecular gate and, given the chip dimensions and migration time of a particular band, the electrophoretic velocity of the analyte was calculated and used to switch on the molecular gate at the appropriate time. A standard mixture of FITC labeled amino acids was separated followed by the computer-automated collection of individual components that explored the autonomous operation of microfluidic devices.

The method for distinguishing chromatographic peaks from baseline drift and noise was based upon the differentiation of the detector signal to produce a waveform that exhibited a zero crossing with the occurrence of a chromatographic peak. This was accomplished by subtracting from the real time signal the value of the signal preceding it in time by a constant offset ( $\Delta X$ ). The shapes of chromatographic peaks were well approximated as Gaussians, and it could be shown that for peaks of approximately the same width, the waveform generated by this differentiation exhibited a zero crossing at the same fraction of the total peak height. The zero crossing exhibited by the differentiation function was defined as the arrival of a chromatographic peak. This differentiation function had the advantage of providing consistent timing for peaks of varying amplitudes. Figure 104 depicts the relationship between an idealized signal (A), its offset, and the inverted counterpart (B) along with the sum (A+B). The dashed line represents the arrival time of the peak.

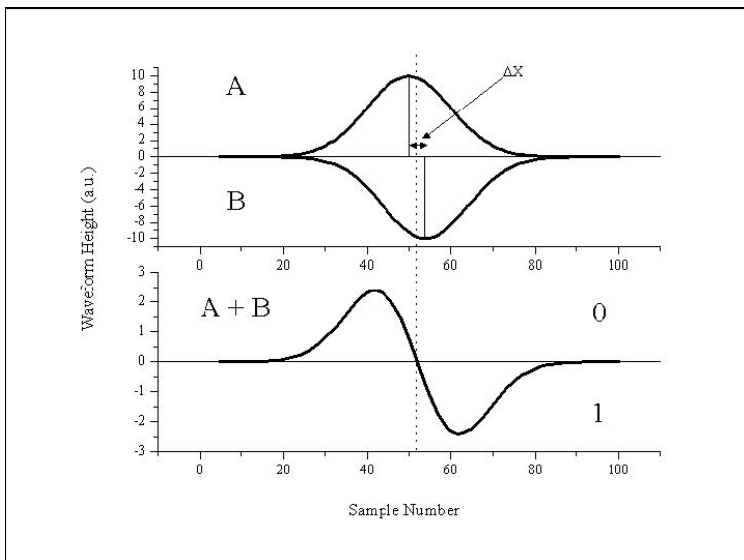
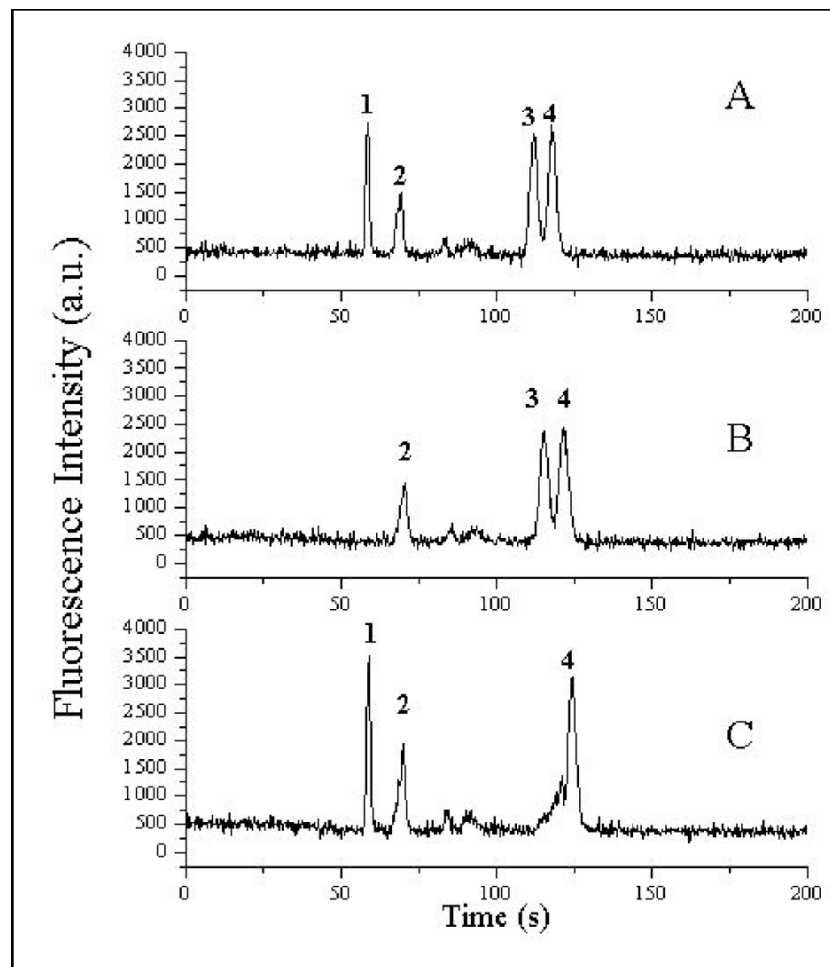


**Figure 104. Scheme for differential detection of chromatographic peaks.**

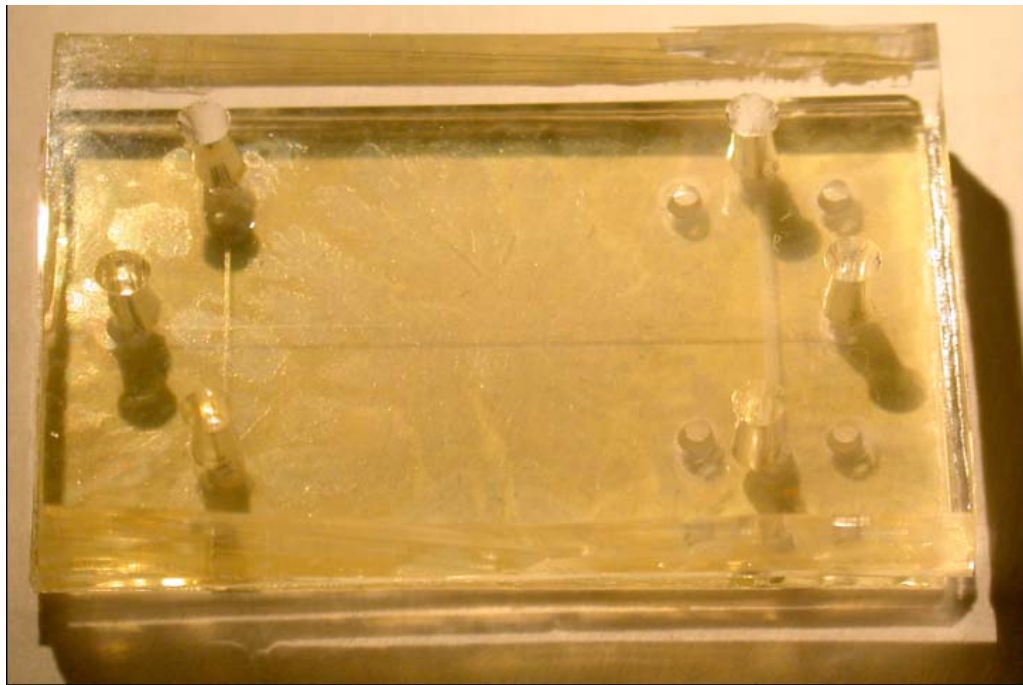
For the regions where the autocorrelation function had a value of zero, the possibility of false positives arising from noise existed. However, since zero crossings produced from chromatographic peaks occurred far less often than those arising from noise, the rate at which zero crossings of the autocorrelation function occurred can be used to reject false positives. This was done by assigning values of zero and one to positive and negative points on the autocorrelation function, respectively. A running sum of these values was kept, and only changes in the sum occurring below an established frequency were accepted as true zero crossings. This method also ensures that only one zero crossing was associated with the arrival of each chromatographic peak (i.e. each peak was counted once). In addition, another criterion was added to reject zero crossings that occurred for signal values that fell below the detection limit.

Figure 105 shows a computer-controlled collection of FITC labeled amino acids that followed the acids separation by electrophoresis. A mixture of labeled glutamate (1) and arginine (3&4) was separated in borate buffer of pH = 8. The peaks were labeled according to the order recognized (pre-gate detection) using the method described above, and was consistent from run to run. Peak number two was an unidentified impurity. Arginine, with two reactive labeling sites, exhibited two peaks corresponding to different

states of labeling. The important feature of these data was that peaks 1 and 3 had very different migration times, and were successfully captured based on the pre-gate triggering signal. The only user input required to perform the collections shown was to enter the peak number to be collected. It was also notable that the smaller peaks between (2) and (3), having signal heights below the established detection limit, were consistently rejected.



**Figure 105. Electropherograms showing the automated collection of labeled glutamate, arginine and degradation products.**



**Figure 106. Optical photograph of the new design for the five-layered second generation BIP.**

#### 5.14 Fluorescence Characterization of Second Generation BIP

The design of the five-layer second generation BIP was altered for several reasons. An image of this new construct (Figure 106) shows the device. In these experiments, only one upper layer channel (right vertical channel) was included at this point in the fabrication. This defined a starting point for the sequential assessment of the separation and gated transport performance within the BIP devices as the number of gated layers was increased. New instrument mounting holders and electrode placement holders were fabricated to include flexibility for the scale up to multiple layers and cross channels during the scale-up to the final BIP construct. Efforts were made to minimize background fluorescence from the glue.

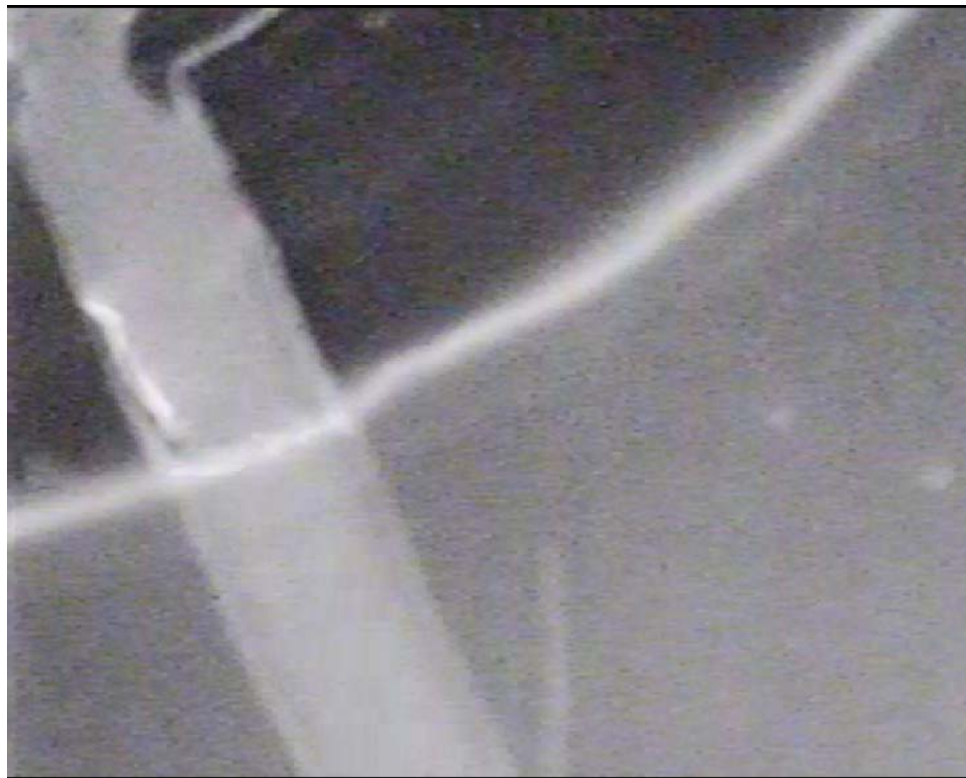


**Figure 107. Fluorescence image at the border of a connection via.**

The channel was filled with 5 mM fluorescein in 5 mM phosphate buffer (pH 7.8).

The fluorescence image in Figure 107, taken at the outer border of a connection via, illustrates the concern. The upper left of this image shows the fluorescence contrast when no glue was present within the via. The bottom right of the image shows the decreased contrast between analyte fluorescence from the channel and the surrounding area (through multiple glue layers). Although the analyte fluorescence could still be distinguished within the channel, there was some concern, because the concentration of analyte used for these investigations was relatively high.

To evaluate the background interference fluorescence spatial profiles were taken across the channel with the single-spot LIF instrument. A 10x objective and a small (100  $\mu\text{m}$ ) moveable pinhole allowed confocal spatial profiling of the background. Starting from the channel wall and moving toward the center of the channel, minimum background fluorescence was observed after three spatial steps. The second minimum in Figure 108 was the perpendicular movement away from the channel center in the opposite direction

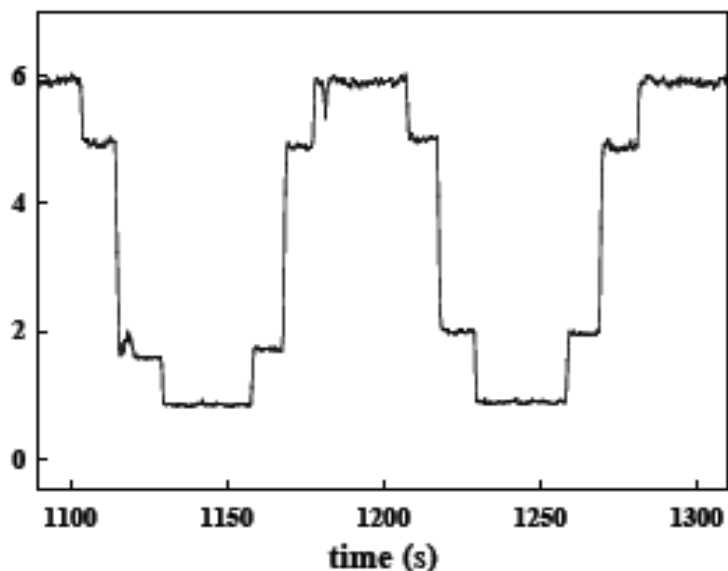


**Figure 108. Laser-induced fluorescence intensity profiles.**

Taken at various positions relative to the channel center. The channel was filled with 5 mM fluorescein in 5 nM phosphate buffer (pH 7.8).

and then back to the channel center. Large differences in signal intensity were observed for the optimized analyte fluorescence from the channel compared to the background fluorescence from the glue-only regions. The large signal-to-background ratio measured here diminished concerns about interference and sensitivity limitations that would be imposed by the glue fluorescence. On-going experiments continued to evaluate the LIF detection of analytes within these second-generation BIP devices.

### 5.15 Membrane Gated Injections for Chip-based Separations

When used as an injector, the molecular gate served as the active transport element between spatially and fluidically distinct injection and separation channels. The crossed intersection of the channels separated by the nanoporous interconnect was spatially located at a traditional injector location (Fig. 109). Interestingly, the increased sophistication achieved in a multilayer design was easily implemented to achieve injections for microfluidic separations. Laser induced fluorescence and fluorescence microscopy were used to interrogate the performance of the molecular gate injection

scheme, and its success with respect to electrokinetic separations was demonstrated in the acquisition of reproducible electropherograms for the separation of FITC-labeled arginine

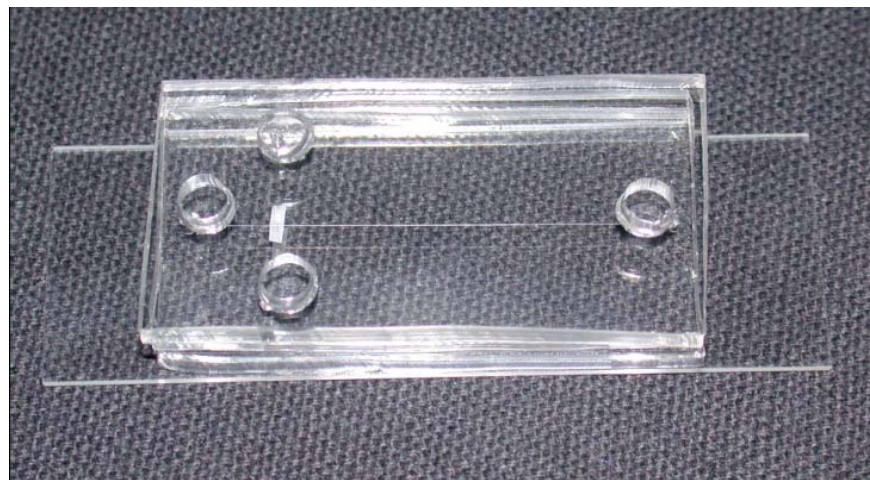


**Figure 109. Optical photograph of PDMS devised used to demonstrate gated-injections for microfluidic chip-based separations.**

and tryptophan. Arginine related peaks (elution time – 15.6 sec  $\pm$  0.6%) were detected with standard deviations of 1% for area and 3% for height. The later eluting (43.7 sec  $\pm$  1.6%) tryptophan peaks had standard deviations of 5% for area and 3% for height. The increased variance associated with the tryptophan peaks were an indication of a relatively small electrophoretic bias, as seen with other electrokinetic injection schemes. Nonetheless, injection times down to 0.3 sec along with separation reproducibilities as small as 1% illustrate the potential for gated injection to accomplish fast, serial analyses.

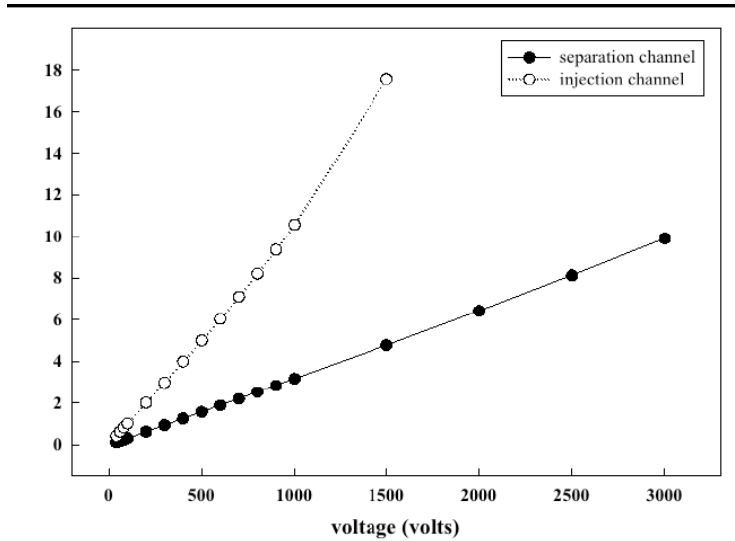


**Figure 110. Current versus applied bias for single layer channels.**

Separation channel was 44-mm in length. Injection channel was 14-mm in length. Both channels were 50  $\mu\text{m}$  wide and 30  $\mu\text{m}$  in height.  $N = 3$ .

### 5.16 Impedance Analysis of the Membrane Gated Injections

Impedance analysis further substantiated the use of these nanofluidic interconnects for high voltage electrokinetic transport schemes, and have proven valuable for microchip separations. Current versus voltage curves for single layer channels (Figure 110) displayed the high-voltage limitations for two specific PDMS channels (50  $\mu\text{m}$  wide) of different lengths. The injection channel (14-mm in length) departed from linearity at 1500 V (1041  $\text{V cm}^{-1}$ ), presumably due to Joule heating effects, while the longer separation channel (44-mm in length) showed linearity out to 3000 V (682  $\text{V cm}^{-1}$ ). It was readily apparent that the separation channel had higher impedance than the injection channel, as expected. These initial characterizations of single-layer impedances established a benchmark with which to compare the incorporation of the nanofluidic molecular gate within the bias applications.

Current versus voltage curves are presented for separation and injection bias schemes in Fig. 111. The separation bias scheme had a simple equivalent circuit that involved only a single element and yielding a channel resistance  $7.45 \text{ M}\Omega\text{cm}^{-1}$ . Impedance analysis for

the injection scheme was not as straightforward, but the i-V linearity indicated the

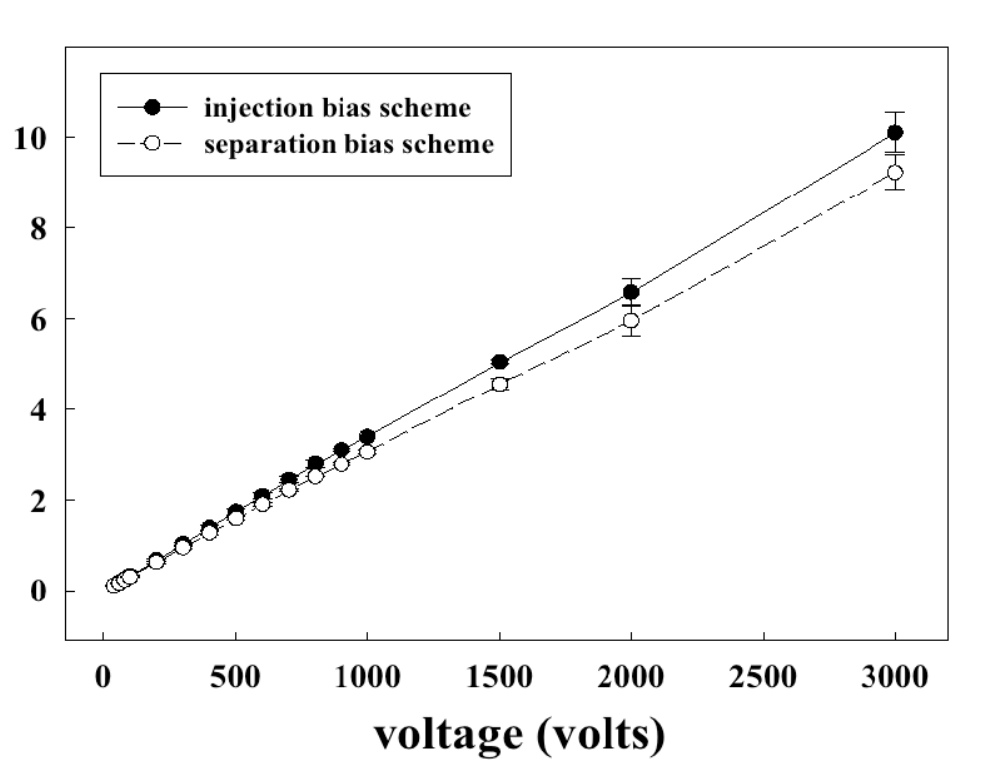


**Figure 111. Current versus applied bias for an injection bias scheme compared to a simpler separation bias scheme.**

$$n = 3.$$

absence of Joule heating. The overall resistance contribution was decreased by the symmetrical application of voltage across the two 7-mm microfluidic injection arms. Factoring in the length differences, the separation channel resistance was calculated from the first analysis as  $258 \text{ M}\Omega$ . Therefore, the effective membrane resistance was determined to be approximately  $17.5 \text{ M}\Omega$ .

One perspective gained from this impedance analysis (Figure 112) was knowledge of the voltages dropped across these arrays of nanofluidic pores within the gate region. In the case where 1 kV was applied to each injection arm, 60 V was dropped across the membrane. The membrane voltage linearly increased to 180 V across membrane, when 3 kV was applied. This produced a field strength of  $300,000 \text{ V cm}^{-1}$  for the 3000 V injection bias application. However, the increased surface area to volume ratio gained by an array of nanofluidic pores must also be taken into account. Assuming 7500 pores in

the gate region, along with linear channels perfectly perpendicular to the surface (surface area of  $7.5 \times 10^{-8} \text{ cm}^2$  per pore), would produce a set of parallel paths for current conduction. The large surface-to-volume ratio means that the membrane material (polycarbonate) itself did not have to support such a large field.

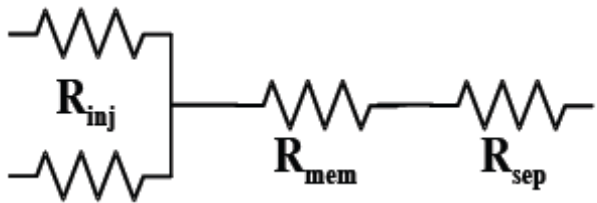


**Figure 112. Simplified representation of the equivalent electrical circuit for the injection bias scheme.**

### 5.17 Fluorescence Characterization of Second Generation BIP's

The efforts to minimize background fluorescence generated by polyphenol glue layers were previously described. Laser-induced fluorescence profiling has shown the relative differences between the background and a channel filled with  $5 \mu\text{M}$  fluorescein in  $5 \text{ mM}$  phosphate buffer (pH 7.8). A series of fluorescein concentrations were used to quantify a lower limit of detection in these second generation BIPs constructed with polyphenol glue layers. A calibration curve (not shown) produced a low nanomolar detection limit. While this lower limit of detection was not optimal for fluorescence detection, this value was sufficient for a number of analyses and helped in comparing the various steps taken to minimize this background contribution.

### 5.18 Membrane Gated Injections for Microfluidic Chip-based Separations

To further characterize the injection utility, various gate parameters were varied while monitoring the separation of two FITC-labeled amino acids. Fluorescence microscopy experiments previously reported showed that when the injection potential was changed, there was a corresponding change in the observed size of the injected analyte band. Because equal voltages were applied for injection and separation when a single power supply was used, the two parameters were linked. Different power supplies could be

used for injection and separation, if desired. With a single power supply, higher voltages increased both the sample amount and the separation speed.

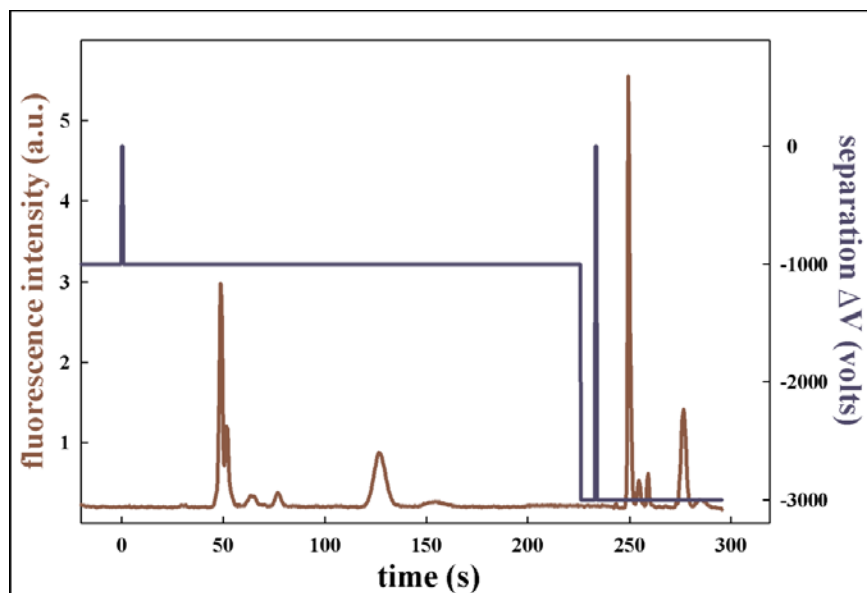


**Figure 113. Separation of FITC-labeled arginine and typtophan.**

FITC-labeled arginine (2.5  $\mu$ M, 1<sup>st</sup> major peak) and tryptophan (7.5  $\mu$ M, 2<sup>nd</sup> major peak) in 5 mM phosphate buffer (pH 7.8) as a function of gate injection and separation voltage. Fluorescence intensity (solid line – left axis) in the detection region and applied separation bias (dashed line – right axis) as a function of time.

The electropherogram in Fig. 113 demonstrates the overall effect of changing potentials for serial injections of the same duration. The first injection and separation were conducted at 1 kV, while the second experiment used a 3-kV bias. The baseline stability at the higher electrokinetic field strength was consistent with the high degree of fluidic isolation between the injection and separation channels. Experiments were run quickly and repetitively with this microchip electrophoresis design. Injection and separation protocols for a specific analysis were evaluated, and the ensuing set of serial separations was rapidly investigated. The lack of electrokinetic sample transport in the injection channel during the separation also allowed the sample in the injection channel to be changed during a separation. Sample replacement was especially facilitated using the pressure loading of the injection channel, thereby enabling flow injection analyses.

### 5.19 Impedance Analysis of the Membrane Gated Injections

Impedance analysis of the injection scheme was previously described. The following discussion was an expansion of the impedance analysis that probed the array of nanofluidic pores within the gate region, as well as individual nanopores. For membrane-gated injections where 3 kV was applied, approximately 180 V was dropped across the membrane. Given the 10- $\mu\text{m}$  thickness of the membrane, the effective field strength was 180,000 V cm<sup>-1</sup> for the 3 kV injection bias. Assuming these membranes had properties typical of other polycarbonate films, the 180 V was approximately 7% of the expected breakdown voltage (6300 V/mil) of the film itself. The overall membrane was modeled as a parallel array of impedances. Assuming average pore densities (7500 pores in gate region) along with linear channels that are perfectly perpendicular to the surface, the measured membrane impedance yields an impedance for each pore of  $R_{\text{pore}} = 7500 R_{\text{memb}} = 1.3 \times 10^{11} \Omega$ . For 200-nm diameter pores this yielded an individual pore impedance of 41 k $\Omega$  cm, a reasonable value for the electrolyte solution used. Furthermore, the pore network was in parallel with the effectively infinite impedance of the membrane, so the relevant parameter to consider for device failure was the current that could be supported before Joule heating in the pores becomes problematic. Under the conditions used here a current of 10  $\mu\text{A}$ , or 1.3 nA per pore, which was easily within the linear (ohmic) regime, was supported by the array of nanopores. Each nanopore was thus expected to dissipate *ca.* 230 nW during the voltage pulse, again an amount which could be easily dissipated.

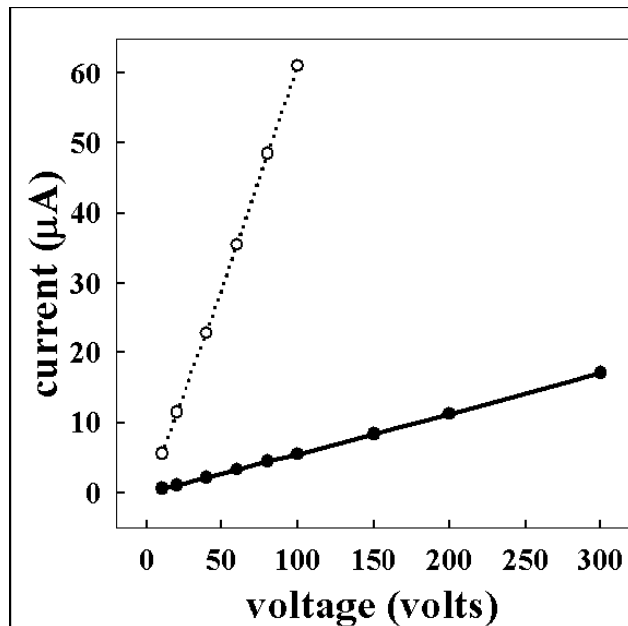


**Figure 114. Current vs. applied voltage in individual channels of a single device.**

There was a concentration gradient of salt across a 15-nm pore diameter membrane gate. Solid trace was for the channel filled with 10 mM phosphate buffer (pH 7.4). Dashed trace was for the channel filled with 10 mM phosphate buffered saline (pH 7.4).

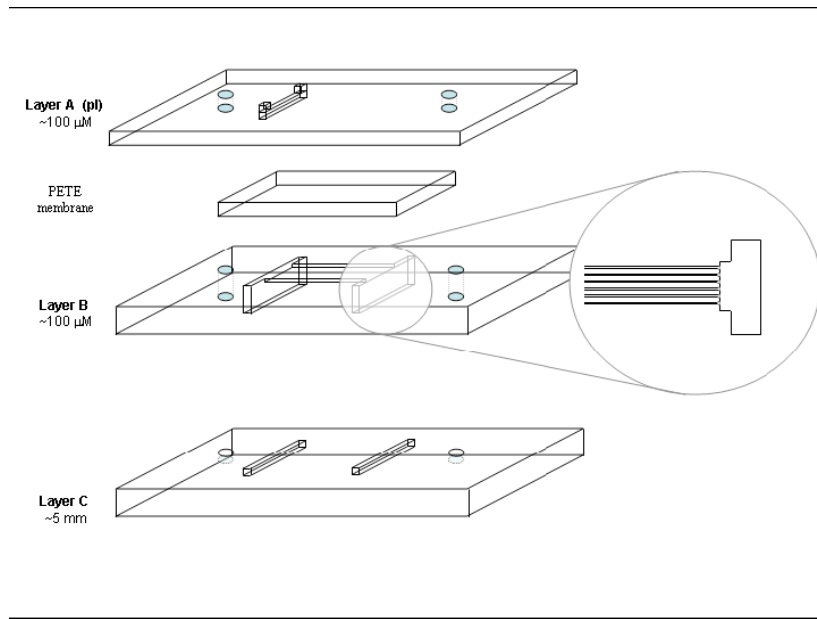
## 5.20 Microfluidic Salt Gradients Across Nanofluidic Membrane Gates

The utility of membranes gates as microfluidic chip injectors was extended by exploiting the benefits of the nanofluidic interconnection, specifically the high degree of isolation, as demonstrated in Figure 113. By using a 15-nm pore diameter membrane gate, initial experiments showed the establishment of a long-term stable salt gradient across the membrane gate. Resistivity measurements (current vs. voltage plots) between the two reservoirs of a single channel were used to probe the relative salt content as a function of time. Figure 114 displays the impedance analysis of individual channels within a single device. The bottom channel contained 10 mM phosphate buffer, while the top channel simultaneously contained 10 mM phosphate buffer saline (w/ 138 mM NaCl and 2.7 mM KCl), a physiologically relevant buffer. Both buffer systems were prepared at pH 7.4 to eliminate any pH gradient effects.

The resistances obtained from this plot were equivalent to the resistances obtained when both channels were filled with a single buffer system. Furthermore, these resistivity values held constant for up to 2.5 hours. The duration limitation was not dependent on

leakage (diffusion) across the gate, but rather reservoir evaporation effects, which caused a resistivity increase in both channels. Initial transport experiments of either the low salt or high salt buffer solutions showed that the resistivity of either channel was altered. Furthermore, electroosmotic flows from the large reservoirs were easily used to “clean” out either channel, thus restoring the initial resistivity differences associated with this salt gradient. With this technology, the high salt concentration analytes in most biological systems could be pre-cleaned to reduce the salt contained, thereby greatly improving the following electrophoretic separation and/or mass spectrometric analysis.

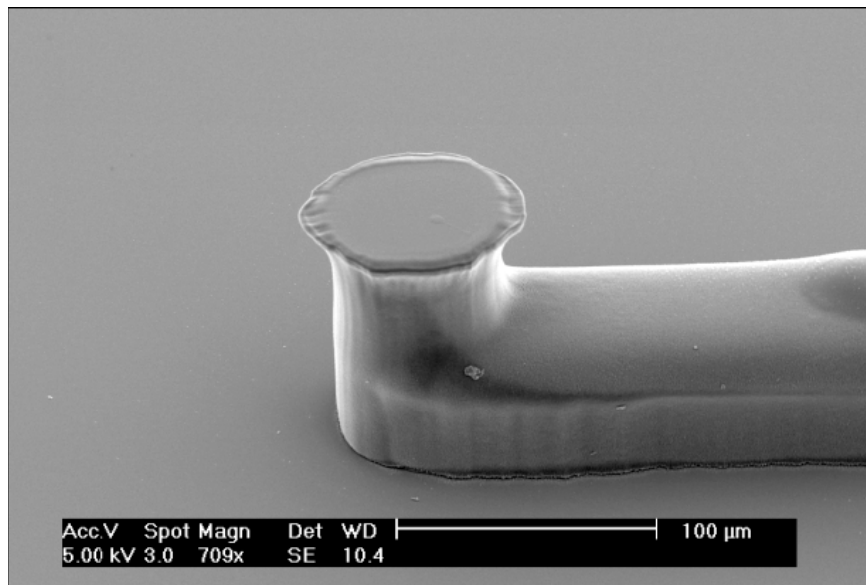
Three dimensional microfluidic constructs offer the advantage, over their two dimensional counterparts, of being highly adaptable to performing complex chemical separations. Sequential separations were performed, which were based on completely different physiochemical principles, and efficiently separated all components within a sample. One of the most successful methods for separating proteins was isoelectric focusing/sodium dodecyl sulfate (IEF/SDS) gel electrophoresis where proteins were separated independently based upon the charge states and molecular weights, respectively. Typically separations of this type can take up to two hours or more. The time to complete this analysis depended on the highest electric field magnitude that could be sustained across gels such that joule heating did not prevent efficient separations. It would be advantageous to adapt the techniques of gel electrophoresis to microfluidic formats, since gels with a much higher surface to volume ratio could sustain substantially higher electric fields, and thus reduce analysis times. Microfluidic architectures which possess the ability to separate complex biological samples would be of great importance for simultaneously identifying multiple biochemical warfare agents. A multilayered microfluidic device to perform 2D gel electrophoresis of proteins was worked on.



**Figure 115. Schematic representation of a microfluidic chip designed for 2-D separation of proteins.**

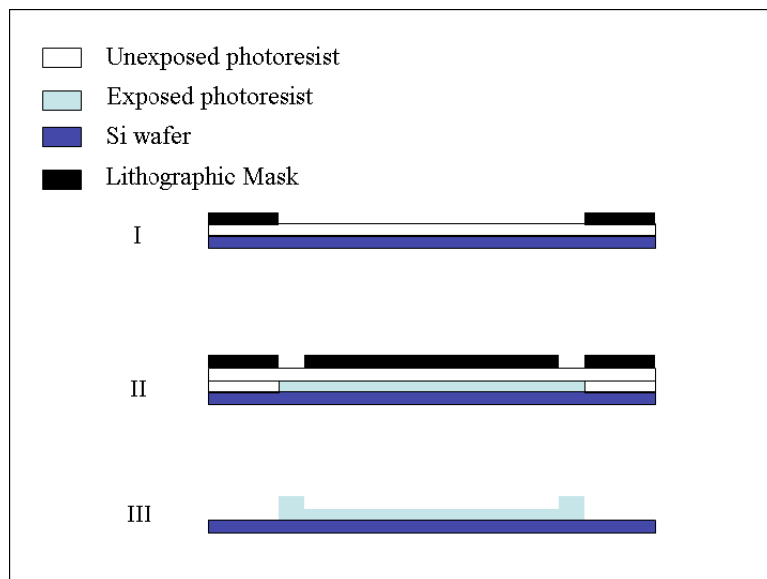
Proteins were isolated by their isoelectric points and molecular weights in layers A and B, respectively.

Figure 115 shows a schematic of a four layer device that was developed. Layers A and B were designed to perform IEF and SDS gel electrophoresis, respectively. These layers were separated by a *polyester* nuclear track-etched membrane similar to the polycarbonate membranes used in previous electrophoresis chips. It was previously established that these membranes could transport molecules with molecular masses up at least 2 MDa. Thus, there was confident that these membranes could serve to transfer proteins to the second layer (separations by mass) after the initial separation (based on charge state) in the first layer.



**Figure 116.** SEM micrograph of a 3-D micro-fluidic channel.

The first technical challenge to overcome in developing the device depicted in Fig. 115 was to fabricate the IEF capillary of the first layer. The simplest method of sample introduction was to inject the IEF capillary with a gel/sample mixture. However, the inlets to the capillary must be small compared to the dimensions of the capillary. Otherwise the time required to separate the sample contained within the inlet reservoirs and capillary would be immense. The inlet reservoirs, approximately  $50 \mu\text{m}^3$  in volume, were constructed via optical lithography and not by the simple mechanical punches that are popular in rapid prototyping. This was accomplished by creating masters (Figure 116) for standard soft lithography by alternately spin coating and exposing two layers of photoresist, as shown in Figure 117. Devices were cast by pouring a PDMS pre-polymer mixture over the masters, and then the mixture was allowed to cure.



**Figure 117. Schematic depicting method for patterning in 3-D masters to create PDMS microfluidic devices via soft lithography.**

UV exposure/baking occurred at steps I and II, and the final development occurred at step III. The thickness of each layer of photoresist was controlled through pre-determined spin coat parameters. PDMS poured over this master created a three-dimensional microfluidic channel suitable for gel isoelectric focusing (IEF) of proteins.

### 5.21 Automated Manipulation of Attomole Samples

Previously it was reported the ability to perform on-chip manipulations of FITC-labeled amino acids subsequent to separation by electrophoresis. The method described earlier relied on real time application of a signal differentiation function to electropherograms, so that the analyte peaks were identified, and the migration times were measured. Initially, separations were monitored by recording signals at a position upstream of the molecular gate, which avoided contributions to the signal due to scatter from the membrane.

Migration times were used to calculate electrophoretic velocities, and when the peaks arrived at a molecular gate, the gate was activated to collect peaks of interest. A limitation of this method was that it assumed the migration times of analytes to be constant during the collection and separation states of devices. This assumption may fail for analyte peaks which arrive at the molecular gate after a previous peak collection was performed, and would prevent the collection of multiple peaks to be performed during a

single separation. In addition, the duration needed to perform a collection had previously been judged from an understanding the dependence of peak width upon the migration time. While the contributions to peak broadening were well understood, significant variations in peak broadening were observed between experiments due to a superposition of laminar flow upon the flat flow profile normally characteristic of electroosmotic flow. The magnitude of this contribution depended on the extent to which the level of fluid in each reservoir was controlled.

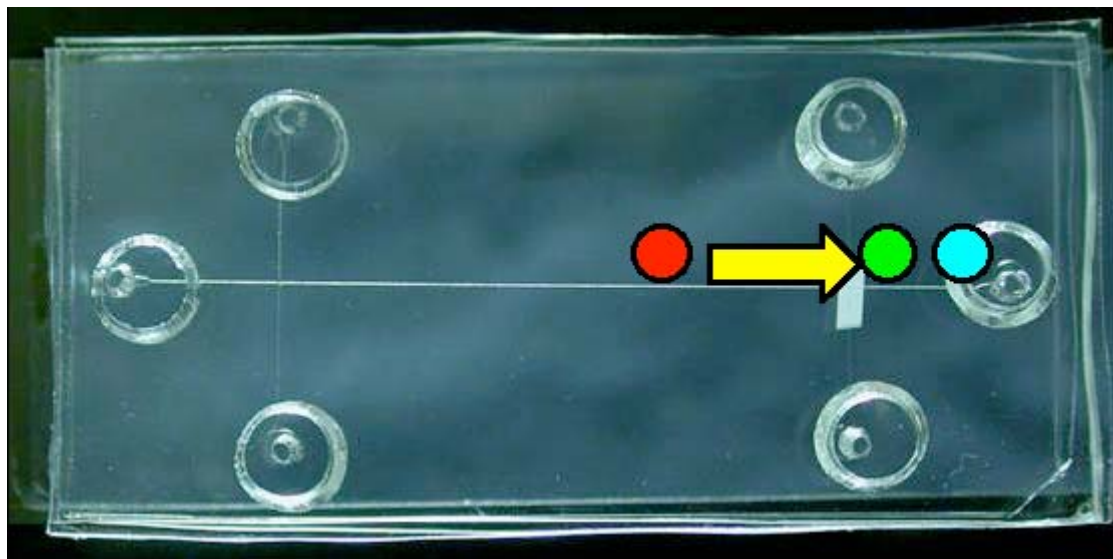


**Figure 118. Schematic showing the relationship of detection strategies and device layout.**

Pre-gate, at gate, and post gate detection spots are shown in red, green and blue, respectively. The gate triggering signal was moved from a position prior to the gate to the being at the gate, as shown by the yellow arrow. All detection points were within the electrophoresis (horizontal) channel, and are not shown to scale.

The peak collection was improved to eliminate those problems by placing the gate-triggering signal at the molecular gate (Fig. 118). Increases in the background signal due to scattering of the source beam was found to not limit the ability to detect analyte peaks. Placement of the triggering signal obviated the need to precisely measure peak migration times and widths. Peaks could be collected simply by turning on the gate when a peak

was detected, and then turning off the gate when the signal fell below the detection limit established by the peak detection algorithm.

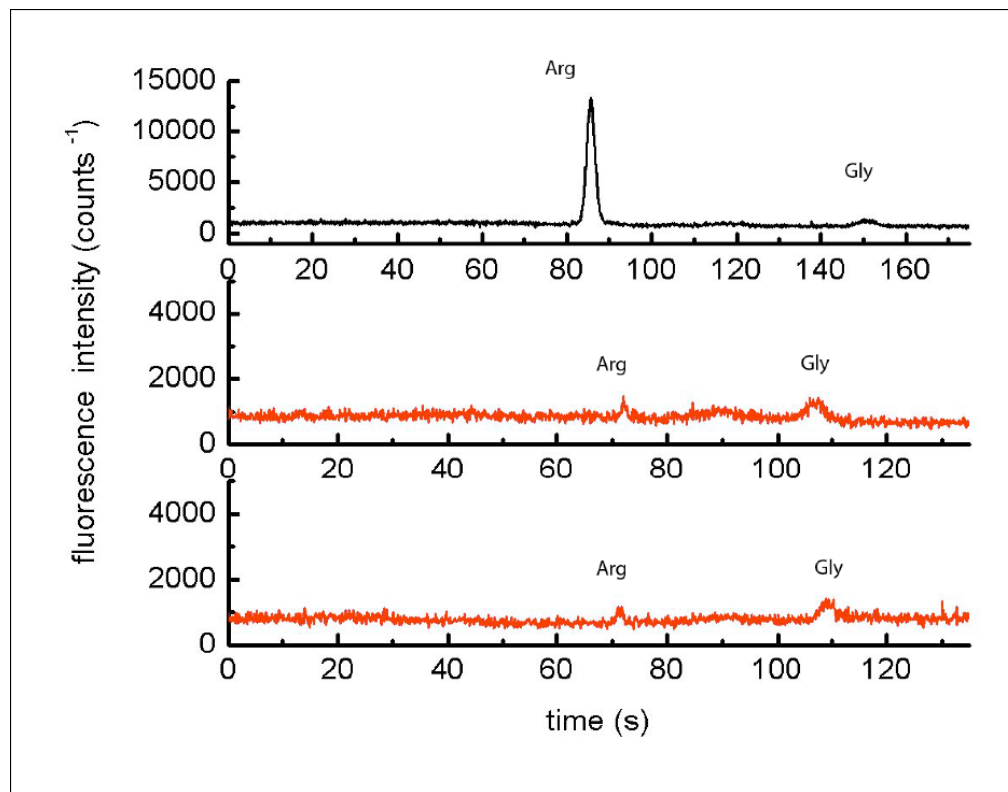


**Figure 119. Separation and collection of FITC-labeled amino acids arginine and glycine.**

All electropherograms shown were monitored with a post gate detector. The top graph was recorded without the collection of arginine, while the lower graphs were recorded when the collection of arginine was performed.

Figure 119 shows the separation of the FITC-labeled amino acids arginine and glycine. The topmost plot was an electropherogram, which was recorded without collection, while the lower two plots were recorded for collection of FITC-Arginine. Comparison of the integrated peak areas with and without collection revealed that collection was accomplished with an efficiency of greater than 98%.

Further work on interfacing and operating the BIP continued on automatically separating out attomole samples using the molecular gates for collecting specific bands from the electrophoresis channel, and injecting those bands into collection channels for further

processing. In addition, a storage method was developed for the separated bands to conduct post-processing analysis for the exact identification of the band.

## 5.22 Post-Processing of Collected Samples

As an additional identification tool, a new tool was developed that enabled the post-processing of separated species using nanometer gold colloids. The goal was to collect bands via the molecular gate, attach the species to the colloids, and then introduce the colloid complex to other analytical identification methods, such as Matrix Assisted Laser

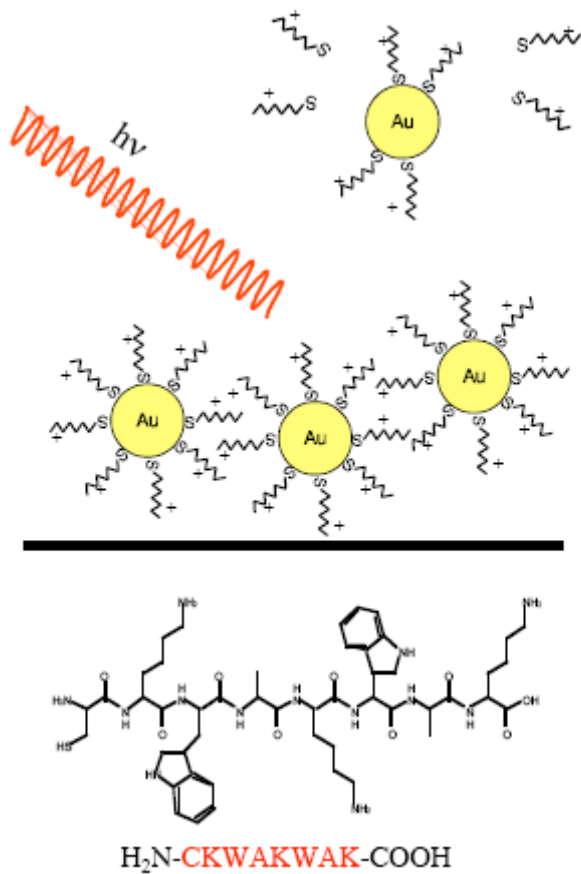


**Figure 120. Representation of attaching target specie on nanometer gold colloids for identification by MALDI.**

Desorption Ionization (MALDI) mass spectroscopy. In this manner, the same sample that gave a positive fluorescent response could be collected, stored, and released for mass spectrometry identification of the species.

To demonstrate the concept, Figure 120 shows a target analog molecule, H<sub>2</sub>N-CKWAKWAK-COOH, that was absorbed onto nanometer sized gold colloids for storage of the analog species. Subsequently, the species was desorbed as ions from the colloid matrix using infrared (IR) laser irradiation for introduction into a mass spectrometer. Both the absorption and desorption of the target species were determined to be sufficiently high for the technique to be viable.

### 5.23 Dynamic Mixing Studies with Ultrafast Confocal Microscopy

Previously the ability of nanocapillary transport to effect rapid mixing between two microfluidic channels was established. Confocal fluorescence microscopy was used to show the distribution of analyte in the gating region as a function of z-distance away from the gate. In this previously mixing scheme, the flow was established before probing the spatial homogeneity. This efficient static mixer was extended for the development of dynamic injection. Because of the dynamic nature of establishing these rapid flow rates, ultrafast scanning was required for these confocal fluorescence studies, and z-profile scans were obtained in less than 300 ms.

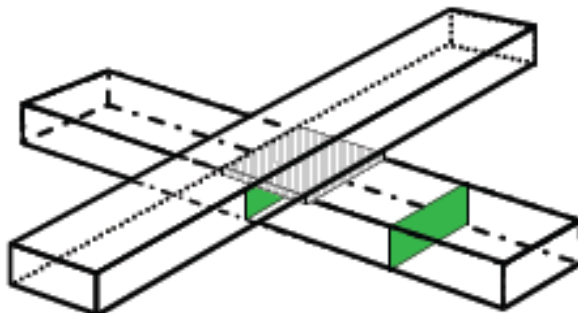


**Figure 121.** Schematic of a multilayer device showing positions for confocal XZT series used for studying dynamic mixing (i.e. gated injections).

As shown in the schematic in Figure 121, two positions relative to the gating region were probed, directly under the gating region and 350-μm downstream. The series of images in Figure 122 were for a 1-s injection (panels 1-6), followed by microfluidic flow (panels

7-12), taken directly under the gating region. The image in panel 2 shows the heterogeneity initially associated with establishing nanofluidic flow. The series of panels up to panel 6 shows a continual progression of a major fluid front. The interesting point to note was the relatively small, but discernable presence of fluorophore within the entire channel, even before the major fluidic flow filled the channel. The images in panels 7 to 12 showed the homogeneous washing away from the analyte, a further indication of the

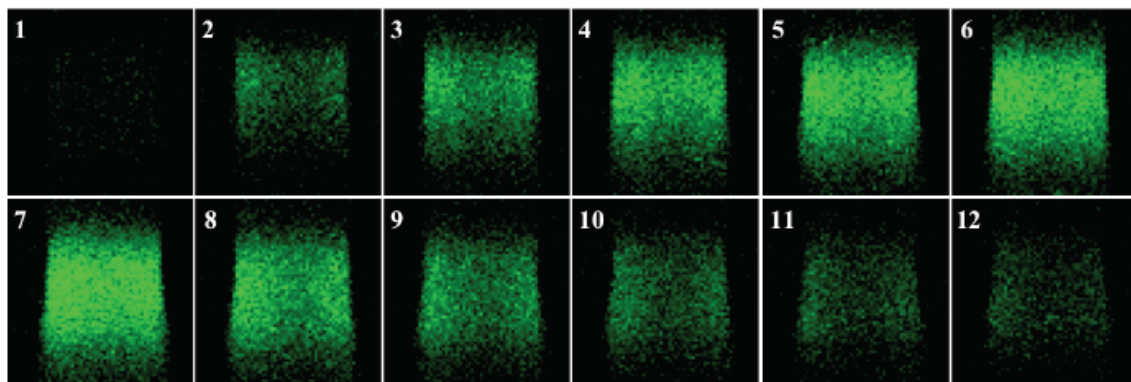


**Figure 122. Confocal XZT series (210 ms/frame) for 1-s injections across a 200-nm diameter nanocapillary array.**

The Imaging position was directly at gate region in the receiving channel. Source channel was at top of panel. Panels 1-6 were during flow across nanocapillary array. Panels 7-12 were for microfluidic flow in receiving channel sweeping injected band away from imaging area. 10- $\mu$ M fluorescein in 10 mM phosphate buffer (pH 7.4). Microfluidic receiving channel was 80-mm high and ~65mm wide.

unique nanofluidic scale transport phenomena. Additional experiments that involved the reverse configuration of injecting buffer into fluorophore were used for quantitative measure of the two distinct flow mechanisms. The major front that can be seen to progress was assigned to the microfluidic flow rate of 10  $\mu$ m/s at these small potentials. The fast component of the flow was determined by measuring the rate of the overall diminishing signal for buffer injection into fluorophore. Assuming an average potential

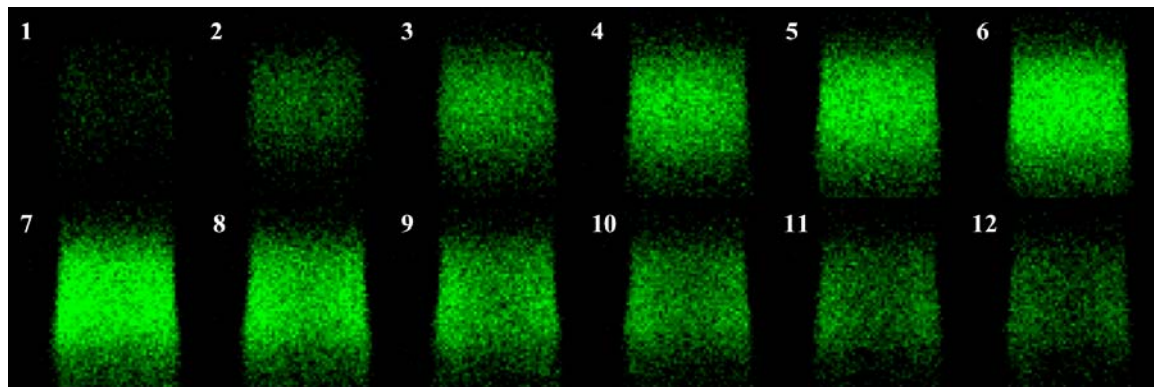


**Figure 123. Confocal XZT series (210 ms/frame) for 1-s injections across a 200-nm diameter nanocapillary array.**

The imaging position was 350-  $\mu$ m downstream from the receiving channel. The source channel was at the top of panel. Conditions were the same as in Figure 119.

field across the nanocapillary array and average electrophoretic mobilities, the rates were calculated to be from 3 to 60 mm/s, which corresponded to a rapid mixing time of 7 to 140 ms.

The images in Figure 123 were for a 1-s injection collected 350- $\mu$ m downstream from the gating region. Once again, panels 1-6 were associated with nanofluidic flow, while the 7-12 panels were for the subsequent microfluidic flow. The initial detection of fluorescence in the microfluidic flow was homogeneously distributed. This was an expected result, because at these flow rates and combined with nominal diffusion, any molecule at one side of the channel would have easily diffused to the other side. These dynamic experiments further validated the static mixing experiments, and allowed for a perspective on the evolution of potential fields.

## 6. CONCLUSIONS

The primary question that was answered by this research was how nanofluidic potential fields coupled with the microfluidic fields. Another key challenge was the development of the ability to control the volume and transport properties of nanocapillary array membranes. An approach to this problem was to form membranes with pre-designed patterned arrays of nanopores by focused-ion beam (FIB) direct writing (Figure 124). For example, single nanochannels were created via focused-ion beam milling. Thin films (8  $\mu\text{m}$ -thick) of poly(methylmethacrylate) (PMMA, 350 kDa in anisol) were spin-coated (6000 rpm) on 5 mm x 5 mm silicon wafers and cured at 195 °C for at least 1 hr. The cured PMMA films did not adhere to the silicon carrier, because the films contained a trace amount of poly(di-methylsiloxane)-poly(ethyleneoxide), added to the solution before casting. Gold (10 nm) was sputter coated on the PMMA prior to FIB processing,

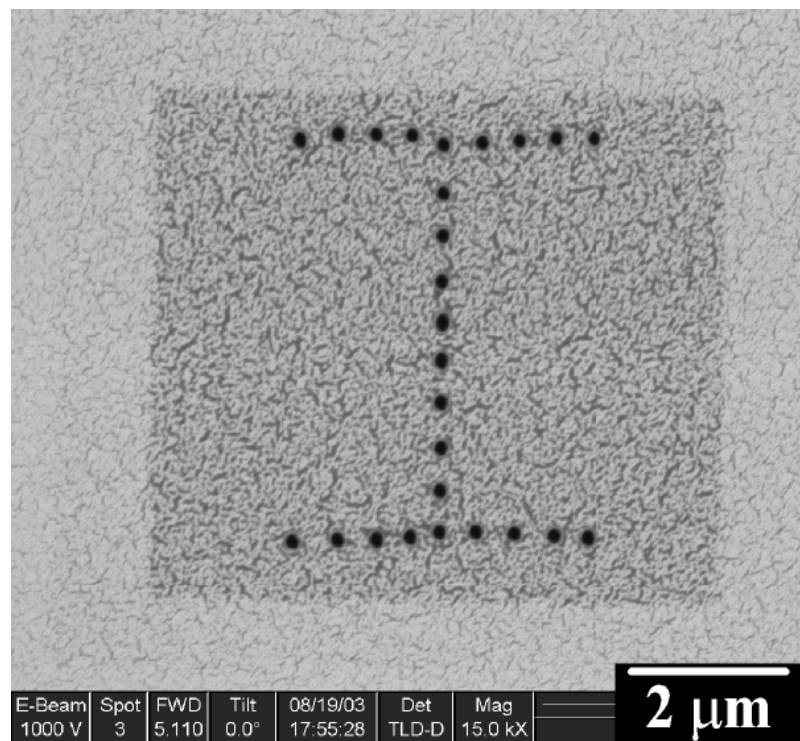


**Figure 124. SEM micrograph of patterned nanopores highlighting the excellent patterning control of the FIB spot-milling process.**

Each milling location was hand positioned via a computer generated graphical image overlay.

which reduced the charging artifacts, since PMMA was an insulator. After ion milling, the layer was removed from the silicon carrier for subsequent experiments. Ultimately a single nanochannel was placed between two crossed microfluidic channels. PMMA rigidity allowed these released thin-films to be carefully handled without major damage.

The nanochannel dimensional reproducibility combined with the specific location control of the FIB also allowed the creation of nanochannel arrays of defined numbers and densities. A demonstration of the direct-write capabilities of FIB to produce high precision arrays of nanochannels with arbitrary control over spatial alignment is shown in Fig. 125. This nanopore array was characterized by  $< 5\%$  standard deviation for the horizontal diameters,  $d = 170 \pm 10 \text{ nm}$ ;  $n = 25$ .

Controlling the number and spatial placement of multiple nanochannels was a powerful tool for investigating electrokinetic transport at the nanoscale. The utility of single nanopores and small arrays of nanopores for understanding how the transport properties can be used to yield the analytically useful reactions envisioned for this project was

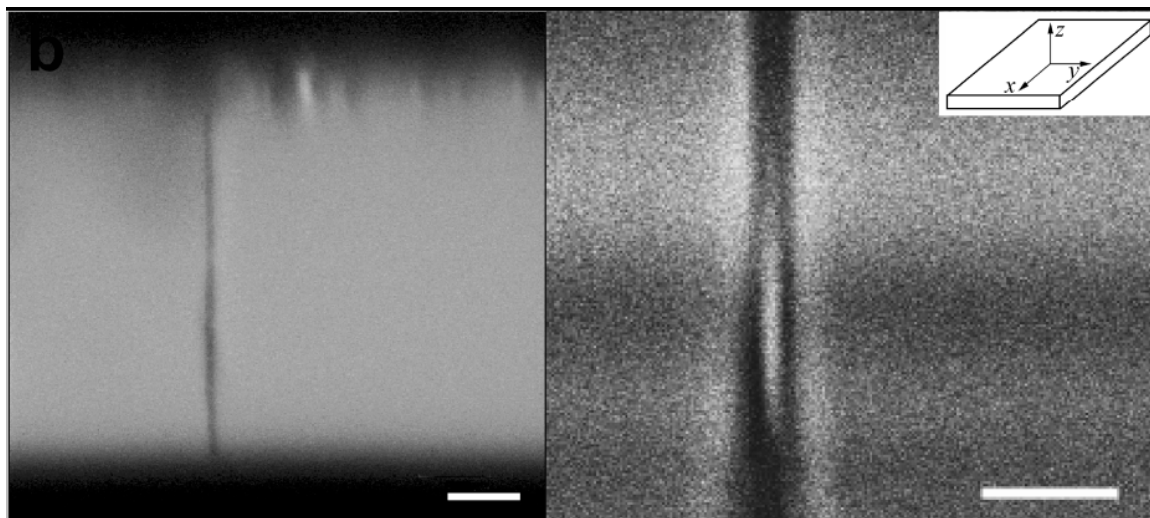


**Figure 125. Confocal fluorescence images sectioning parallel to the xz plane.**

(Left) Vertical slice through a dyed-PMMA layer with a single nanopore spanning the layer; scale bar 2  $\mu\text{m}$ . Measured diameter =  $400 \pm 35 \text{ nm}$  ( $n=10$ ) (Right) Vertical slice through a dye-filled nanopore; scale bar 8  $\mu\text{m}$ . (Inset) Coordinate system for confocal imaging.

illustrated by the confocal sectioning images shown in Fig. 125. Soaking a PMMA layer in a t-butanol solution containing rhodamine dye resulted in the rapid incorporation of dye throughout the polymer, and permitted negative tone fluorescent sectioning by confocal microscopy. The cross-section shown in Fig. 125 (left) was obtained by carefully aligning the  $xz$  plane of the confocal image with the nanopore longitudinal axis. It shows the single nanopore spanned the 8- $\mu\text{m}$  thick PMMA film, and illustrated the uniform diameter along the length of the pore, the high aspect ratio (20 for the pore shown), and confirmed that the time required to mill through 8- $\mu\text{m}$  PMMA layers was less than 3 s. In contrast, Fig. 125 (right) showing an  $xz$  section through a pore loaded with an aqueous fluorescein solution, illustrates the high sensitivity of confocal fluorescence imaging, and raises the possibility of monitoring transport in the interior of these single nanochannels by confocal sectioning.

## 7. SUMMARY AND FUTURE PROSPECTS

The concept of establishing three-dimensional integrated fluidic circuits, which was a dream at the beginning of this project, is now firmly established as experimental fact, and has been confirmed with numerous demonstration vehicles. The Defense Advanced Research Projects Agency (DARPA) and Air Force Research Laboratory support have allowed the establishment of important principles governing fluidic communication in nanocapillary array membranes and, by extension, digital fluidic switches that controlled the interlayer transfer of analyte-containing fluids between vertically separated microchannels. Knowing how to move precisely defined fluid voxels is the enabling capability which will permit the sophisticated multidimensional chemical analysis needed to detect the presence of mass-limited analytes. With these principles now firmly established, it will be possible to push forward the technology towards militarily relevant problems of exposure to biological threat agents, rapid diagnosis of such exposures, and to other problems of acute exposure likely to be encountered on the battlefield of the future.

## 8. REFERENCES

[1] Duffy, D.C., McDonald J.C., Schueller, O.J.A., Whitesides, G.M. *Anal. Chem.* **1998**, 70, 4974).

## APPENDIX I. LIST OF JOURNAL PUBLICATIONS

1. A.N. Chatterjee, D.M. Cannon, Jr., E.N. Gatimu, J.V. Sweedler, N.R. Aluru and P.W. Bohn, "Modeling and Simulation of Ionic Currents in Three-Dimensional Microfluidic Devices with Nanofluidic Interconnects," *J. Nanopart. Res.* **2005**, 7, 507-516.
2. I.-H. Chang, J.J. Tulock, J. Liu, W.-S. Kim, D.M. Cannon, Jr., Y. Lu, P.W. Bohn, J.V. Sweedler, and D.M. Cropek, "Miniaturized Lead Sensor Based on a Lead Specific Catalytic DNAzyme in a Nanocapillary Interconnected Microfluidic Device," *Environm. Sci. Technol.*, **2005**, 39, 3756-3761.
3. C.B. Swearingen, D.P. Wernette, D.M. Cropek, Y. Lu, J.V. Sweedler and P.W. Bohn, "Immobilization of a Catalytic DNA Molecular Beacon on Au for Pb(II) Detection," *Analyt. Chem.* **2005**, 77, 442-448.
4. D.M. Cannon, Jr., B.R. Flachsbart, M.A. Shannon, J.V. Sweedler and P.W. Bohn, "Fabrication of single nanofluidic channels in poly(methylmethacrylate) films via focused-ion beam milling for use as molecular gates," *Appl. Phys. Lett.*, **2004**, 85, 1241-1243.
5. J.J. Tulock, M.A. Shannon, P.W. Bohn, and J.V. Sweedler, "Microfluidic Separation and Gateable Fraction Collection for Mass-Limited Samples," *Analyt. Chem.* **2004**, 76, 6419-6425.
6. T.-C. Kuo, H.-K. Kim, D.M. Cannon, Jr., M.A. Shannon, J.V. Sweedler, and P.W. Bohn, "Nanocapillary Array Membranes Effect Rapid Mixing and Reaction," *Angew. Chem. Intl. Ed. Engl.* **2004**, 43, 1862-1865.
7. D.M. Cannon, Jr., T.-C. Kuo, J.V. Sweedler, M.A. Shannon, and P.W. Bohn, "Nanocapillary Arrays Produce Gated Analyte Injection for Separations and Analysis in Three-dimensional Microfluidic Architectures," *Analyt. Chem.* **2003**, 75, 2224-2230.
8. T.-C. Kuo, D.M. Cannon, Jr., M.A. Shannon, J.V. Sweedler, and P.W. Bohn, "Hybrid Three-Dimensional Nanofluidic/Microfluidic Devices Using Molecular Gates," *Sens. Actuat. A* **2003**, 102/3, 223-233.
9. T.-C. Kuo, D.M. Cannon, Jr., W. Feng, M.A. Shannon, J.V. Sweedler, and P.W. Bohn, "Gateable Nanofluidic Interconnects in Multilevel Microanalytical Systems," *Analyt. Chem.* **2003**, 75, 1861-1867.
10. D.M. Cannon, Jr., T.-C. Kuo, W. Feng, M.A. Shannon, J.V. Sweedler, and P.W. Bohn, "Characterization of Molecular Transport Within Gateable Nanofluidic Interconnects for Three-Dimensional Microfluidic Systems," in *Micro Total Analysis Systems 2001*, J.M. Ramsey and A. van den Berg, Eds., Kluwer Academic Publishers, Dordrecht, **2001**, pp. 199-200.

11. M.G. Spencer, B.R. Flachsbart, T. Yasunaga, T.-C. Kuo, J.V. Sweedler, P.W. Bohn, and M.A. Shannon, "Design and Fabrication of Multiple Nanofluidic Interconnects for Three-Dimensional Microanalytical Systems," in *Micro Total Analysis Systems 2001*, J.M. Ramsey and A. van den Berg, Eds., Kluwer Academic Publishers, Dordrecht, **2001**, pp. 195-196.
12. T.-C. Kuo, D.M. Cannon, Jr., W. Feng, M.A. Shannon, J.V. Sweedler, and P.W. Bohn, "Three-Dimensional Fluidic Architectures Using Nanofluidic Diodes to Control Transport between Microfluidic Channels in Microelectromechanical Devices," in *Micro Total Analysis Systems 2001*, J.M. Ramsey and A. van den Berg, Eds., Kluwer Academic Publishers, Dordrecht, **2001**, pp. 60-62.
13. T.-C. Kuo, L.A. Sloan, J.V. Sweedler, and P.W. Bohn, "Manipulating Molecular Transport Through Nanoporous Membranes by Control of Electrokinetic Flow: Effect of Surface Charge Density and Debye Length," *Langmuir*, **2001**, 17, 6298-6303.